공학박사학위논문

Study on noise and sensitivity improvement of solid-state nanopores for DNA sensing applications

2017년 8월

서울대학교 대학원

재료공학부

박 경 범

STUDY ON NOISE AND SENSITIVITY IMPROVEMENT OF SOLID-STATE NANOPORES FOR DNA SENSING APPLICATIONS

지도 교수: 김 기 범

이 논문을 공학박사 학위논문으로 제출함

2017 년 8 월

서울대학교 대학원

재료공학부

박 경 범

박경범의 공학박사 학위논문을 인준함

2017년 8월

위 원 장	남 기 태	(인)
부 위 원 장	김 기 범	(인)
위 원	김 성 재	(인)
위 원	김 영 록	(인)
위 원	이 민 현	(인)

Study on noise and sensitivity improvement of solid-state nanopores for DNA sensing applications

A DISSETATION SUBMITTED TO

DEPARTMENT OF MATERIALS SCIENCE AND ENGINEERING

SEOUL NATIONAL UNIVERSITY

FOR THE DEGREE OF

DORTOR OF PHILOSOPHY

KYEONG-BEOM PARK

August 2017

ABSTRACT

STUDY ON NOISE AND SENSITIVITY IMPROVEMENT OF SOLID-STATE NANOPORES FOR DNA SENSING APPLICATIONS

Kyeong-Beom Park
Department of Materials Science and Engineering
The Graduate School
Seoul National University

DNA sequencing technology has attracted more attention for applications to personal diseases or personalized medicine. Nanopore based system is attractive for 3rd generation DNA sequencing technology due to its label-free, amplification-free, real-time single molecule sensing, long read-length (> 1kbp) and possibility to portable system. While biological nanopores demonstrate the visible performance of DNA sequencing, solid-state nanopores still have limitations to overcome.

In introductory part (chapter 1 and chapter 2), general overview of nanopore system for DNA sequencing application is described. First, the history and basic principle of nanopore sensing are presented in chapter 1. Also, the technologies for next generation DNA sequencing is introduced briefly and the current situation of nanopore-based sequencer in the DNA sequencing market is described. In chapter 2, the current limitations of solid-state nanopores are reviewed in terms of DNA

sequencing applications. Also, literature survey on previous research to improve the sensing properties of solid-state nanopore are described.

In chapter 3, highly sensitive and low noise nanopore platform in boron nitride membrane on a pyrex substrate is demonstrated. This work is performed in two approaches to reduce both the dielectric noise and flicker noise of device, which is one of the bottlenecks to making highly sensitive 2-D membrane nanopore devices. Flicker noise is minimized by employing multiple layers of BN with sub 100 nm opening size to enhance the mechanical stability of membrane. From our results, we proposed that the flicker noise has a correlation with the stiffness of membrane material, which is one property of mechanical stability.

In chapter 4, a fabrication scheme of a solid state nanopore with ZnO membrane directly deposited on top of quartz substrate by atomic layer deposition (ALD) and the characteristics of DNA translocation through this membrane are presented. Prior to that, transfer-free fabrication process of solid-state nanopore platform based on quartz substrate with the membrane of 2 μm opening aperture by using a polycrystalline Si (poly-Si) as a protection layer is introduced for reliable and reproducible process. ZnO membrane is chosen due to its high isoelectric point (~9.5) as well as its chemical and mechanical stability. Not only this device shows an extremely low noise level as it is fabricated on highly insulating and low dielectric quartz substrate but also it shows that the translocation speed of DNA through ZnO nanopore is more than one order of magnitude slower as compared to

that of SiN_x nanopore device. We propose that the electrostatic interaction between positively charged ZnO pore wall, resulted from high isoelectric point of ZnO, and negatively charged phosphate backbone provides additional frictional force to slow down the DNA translocation.

In this dissertation, three major issues of solid-state nanopores for DNA sequencing application are discussed. These issues include (i) enhancing signal to noise ratio (SNR) (ii) improving spatial resolution (iii) retarding DNA translocation velocity. From the work of chapter 3, the sensitive platform and the understanding of 1/f noise in 2-D nanopores were suggested. From the work of chapter 4, we proposed a ZnO nanopore platform that can slow down the DNA rate efficiently with low noise. Further work will explore the interaction of ZnO pore wall with specific nucleotides for DNA-based applications such as ideal DNA sequencing or single nucleotide polymorphism (SNP) detection.

Keywords: nanopore technology, solid-state nanopore, DNA sequencing, electrical noise, boron nitride, zinc oxide, temporal resolution

***Student Number*:** 2011-20639

Table of Contents

LIST OF TABLES

LIST OF FIGURES

Chapter 1

Illustration of forward and reverse ratcheting of DNA through α-hemolysin. (b) Ionic current trace of single DNA molecule during forward and reverse ratcheting process through α-hemolysin. (c) Schematic diagram of phi 29 polymerase combined with single stranded DNA through MspA. (d) Ionic current traces of the sequence of ssDNA molecules during synthesis process through MspA. Adoped from ref. 21 and ref. 22

Figure 1-6. Nanopore sequencer and its application (a) Minion nanopore sequencer device and its flow cell from Oxford nanopore (b) First sequencing using Minion under microgravity in international space station. Adopted from Ref. 25 and © nanoporetech.com

Figure 1-7. Fabrication method of solid-state nanopores (a) Focused ion beam sculpting method by custom-designed feedback system to control the pore size (b) TEM images of nanopore by ion-beam sculpting method (c) Schematic view of solid-state nanopore device based on Si substrate. (d) Pore diameter control in SiO2 membrane by electron beam radiation. Adopted from ref. 30 and ref. 31

Figure 1-8. Nanopore perforation method by dielectric breakdown (a) Mechanism of nanopore formation by controlled dielectric breakdown (b) Setup for multilevel pulse-voltage injection via dielectric breakdown and TEM images of sub 1 to 2 nm nanopores using this method. Adopted from ref. 34 and ref. 35

Figure 1-9. Hybrid nanopores (a) Hybrid nanopore formation sequence integrated with α-hemolysin protein and corresponding ionic current traces (b) Integration of

Chapter 2

image is cross-sectional STEM image for sub 3 nm-thick SiNx layer. (c) Membrane thinning process based on electron-irradiation and TEM micrograph of an a-Si thinned area with nanopore. The bottom image is the ionic current trace of dsDNA translocation through Φ 4.6 nm nanopore in thinned a-Si membrane. (d) Fabrication of 3 -8 nm thick ALD HfO_2 nanopore. AFM topography shows a freestanding HfO_2 region and TEM image shows Φ 3 nm HfO_2. nanopore. Adopted from ref. 48 , ref. 50, ref. 51 and ref. 37

Figure 2-11. Two dimensional membrane nanopores using graphene and boron nitride (a) Schematic diagram of nanopore device using a suspended graphene material. (b) Representative event traces of dsDNA through graphene nanopores with different diameters, compared to SiN_x device. (c) Measurement scheme of nanopore device using a suspend BN membrane. (d) Raw current traces of 1 kbp dsDNA transport, filtered at 100 kHz, through multilayered BN nanopore with low noise substrate. Adopted from ref. 24, ref. 57, ref. 61 and ref. 28

Figure 2-12. Two dimensional membrane nanopores using moly disulfide (MoS_2) materials (a) Nanopore device of a MoS_2 membrane and TEM image of a nanopore in MoS_2 membrane. (b) Ionic current and voltage trace for nanopore creation in MoS_2 membrane by electrochemical reaction. (c) Scatter plots of single nucleotide translocation events through single layered MoS2 pore using RTILs/KCl viscosity gradient system for retarding translocation speed. (d) Direct growth method for MoS_2 membrane on SiN_x window. Optical and TEM images show MoS_2 membrane on a ~ 1 μm circular window of a SiNx film. Adopted from ref. 62, ref. 63, ref. 64 and ref. 66

Chapter 3

Ionic current traces of single-layered BN pore on Si (s-BN, Φ 5 nm, G = 68 nS) and s-BN (Φ 4 nm, G = 43 nS) and multi-layered BN pore (m-BN, Φ 8 nm, G = 43 nS) under 0 mV and 100 mV. (b)(c) Power spectral density plots of the corresponding devices to panel a under 0 mV and 100 mV.

Figure 3-6. Noise characteristics of BN nanopore devices with different structures. (a) I_{RMS} versus frequency curves of s-BN device on Si, s-BN and m-BN device on pyrex. (b) Normalized power spectral density plots at various voltages for s-BN and m-BN device on pyrex. Each linear line results from the fitting of the data into the equation, $SI/I2 = AN/f$. (c) Power spectral densities of Φ 4 nm (25 nS), 8 nm (78 nS), 12 nm (113 nS) *m*-BN devices at 100 mV. (d) I_{RMS} of the corresponding pores against the applied voltages up to 200 mV.

Figure 3-7. Noise characteristics of low-pass filter effect with 10 kHz and 100 kHz. (a) Power spectral densities of *m*-BN pore on pyrex under 0 mV and 100 mV, filtered at 10 kHz and 100 kHz. (b) RMS noise versus frequency curves of the same pore for 10 kHz and 100 kHz filter under 100 mV, as described in panel a. The black dotted line results from the theoretical fits and it can be split into flicker and other noise part. (c) RMS noise of the corresponding *m*-BN pore with 10 kHz and 100 kHz against the applied voltages up to 200 mV.

Figure 3-8. dsDNA translocation through m-BN nanopore. (a) Ionic current traces for 1kbp dsDNA translocation at 150 mV (black), 200 mV (red) and 250 mV (blue) through Φ 4 nm m-BN nanopore in 1M KCl with TE buffer (pH 8.0), filtered at 100 kHz. Each trace is measured during 10 sec. (b) The scatter plots of blockade current

(ΔI) and dwell time for 150 mV, 200 mV and 250 mV. (c) Normalized histogram of ΔI corresponding to b with different voltages. The inset is blockade current level as a function of voltage, showing linear dependency of ΔI on the applied voltage. (d-e) Similar data set to panel a-c, filtered at 10 kHz.

Figure 3-9. An example of criteria to discriminate real translocation events from bouncing or collisions. (a) Histogram of current drops, which magnitude is larger than $10\times I\_RMS$, at 200mV and 100 kHz. Inset shows a magnified view of representative bouncing and translocation events. (b) Mean blockade currents and dwell time values of translocations and bouncing as a function of voltage.

Figure 3-10. Low-pass filter effect on blockade signals. (a) Ionic current traces for 1 kbp dsDNA translocation through Φ 4 nm *m*-BN pore at 150 mV applied voltage, filtered at 100 kHz (blue) and 10kHz (red) in 1M KCl with TE buffer (pH 8.0). (b) A magnified view of 7 DNA translocation events with different duration, ranged from 20 μs and 200 μs.

Figure 3-11. Signal to noise ratio as a function of voltage at 10 kHz and 100 kHz; SNR = ΔI/IRMS.

Figure 3-12. Relationship of spring constant and normalized flicker noise level at 100 mV in 2-D membrane nanopores. All data are presented in table 3-2.

Chapter 4

Figure 4-1. Fabrication of transfer-free device on quartz substrate. (a) Overall fabrication process of the transfer-free nanopore platform based on quartz substrate. (b)(c) Optical microscope image of top and bottom side of nanopore device with micrometer sized window. (scale bar: 10 μm) (d) Transmission electron microscopy (TEM) images of a free-standing SiN_x membrane with poly-Si supporting layer. An aperture size of poly-Si is 2~3 μm. (scale bar: 1 μm) (e) TEM image of 4 nm diameter nanopore perforated in SiN_x membrane. (scale bar: 10 nm)

Figure 4-2. Chip capacitance calculation considering chip structure. (a) Schematic image of quartz-based chip structure with poly-Si supporting layer. The labeled vertical region is the series connection of the capacitance, and the total capacitance is calculated by the parallel connection of the capacitance of each region. (b) The calculated chip capacitance as a function of opening diameter with the device corresponding to panel a. (c) Schematic image of quartz-based chip structure without poly-Si supporting layer. The calculation procedure is same to panel a. (d) The calculated chip capacitance as a function of opening diameter with the device corresponding to panel c.

Figure 4-3. ZnO device on transfer-free platform. (a) Fabrication process of ZnO nanopore on transfer-free platform. A 7-nm thick ZnO is deposited by atomic layer deposition on suspended SiN_x window. The free-standing ZnO membrane is formed by selective removing of SiN_x using reactive ion etching, (b) SEM image of an area of ZnO membrane and EDS elemental mapping of Si, Zn and O in this region. (scale

bar: 1 μm) (c) EDS spectra of micro-hole region in ZnO nanopore devices before and after SiN_x layer etching. (d) EDS line scan of Si, Zn and O elements across ZnO membrane.

Figure 4-4. Characteristics of ZnO nanopores. (a) TEM image of a free-standing ZnO membrane and the corresponding selective area electron diffraction (SAED) pattern. (b) High-resolution TEM images of representative ZnO nanopores with estimated 1.3, nm (scale bar: 5 nm) (c) Ionic current vs. voltage characteristics for three ZnO nanopores of 1.3, 4 and 6 nm diameters. (d) Power spectral densities (PSD) of 1.3 nm pores (2 nS) under 0, 100 and 200 mV voltages in 1 M KCl electrolyte solution with TE buffer (pH 8.0), filtered at 100 kHz.

Figure 4-5. Noise characteristics of ZnO and SiNx devices. (a) Power spectral densities of ZnO and SiN_x nanopore devices with similar conductance (G ~ 7 nS) at 0 mV. The dotted lines are the fitting lines of thermal noise and dielectric noise. (b) RMS noise versus frequency plots corresponding to panel a. RMS noise is calculated by the integration of PSD (S_I) over frequency as following relation : $IRMS = SIdf$.

Figure 4-6. Continuous 10-sec ionic current trances for 1 kbp dsDNA translocation through Φ 4 nm ZnO nanopore in 1 M KCl with TE buffer (pH 8.0) at the voltages of 200 – 350 mV, filtered at 100 kHz.

Figure 4-7. A study of dsDNA translocation through ZnO nanopore. (a) Representative translocation events of 1 kbp double-stranded DNA though ZnO

pore with 4 nm diameter at various voltages in the range 200 mV to 350 mV. (b) Scatter plots of blockade current (ΔI) vs. dwell time (t_D) for 1 kbp dsDNA translocation events through 4 nm ZnO pore at the applied voltages with 200 mV to 350 mV. (c) Histograms of ΔI corresponding to panel b, in the 200 – 350 mV voltage range. Inset is the mean values of ΔI as voltages increases. (d) Histograms of logarithm of t_D in the 200 – 350 mV voltage range. Inset is the mean values of t_D as corresponding voltages. The data is fitted into exponential decay function in the dashed line.

Figure 4-8. Further investigation of slowing effect of ZnO pore. (a) ΔI versus t_D scatter plots of 1 kbp dsDNA in Φ 4nm ZnO (red) and Φ 8 nm SiN_x (black) nanopores at 250 mV in 1M KCl with TE buffer (pH 8.0), low-pass filtered at 100 kHz. (b) Extracted values for drift velocity *v* and diffusion coefficient *D* of ZnO and SiNx devices as a function of the applied voltage from 1D Fokker-Planck equation. (c) Friction coefficients of hydrodynamic drag (f_{Drag}) and electrostatic interaction ($f_{interaction}$) in the range of the applied voltage.

Figure 4-9. Friction force model in ZnO pore. (a) Scheme of a typical dsDNA translocation through a positively charged ZnO pore along with electrophoretic driving force (F_{el}), hydrodynamic drag force (F_{drag}) and surface frictional force (F_{in}) of electrostatic interaction. (b) Histograms of dwell time for 1kbp dsDNA translocation through 4 nm ZnO pore at 200 – 400 mV. The solid-lines are the fitting lines to 1D Fokker-Planck model for obtaining the drift velocity and diffusion coefficient.

Figure 4-10. Reproducibility check of slow translocation in ZnO pores. (a) Scatter plots of ΔI and t_D through different ZnO pores at 400 mV. (b) The Histograms of logarithm of t_D corresponding to panel a.

Figure 4-11. Poly A_{60} ssDNA translocation through ZnO nanopore. (a) Continuous current trace through ZnO pore with Φ 1.2 nm diameter in 3 M KCl concentration at 300 mV, filtered at 100 kHz. (b) Scatter plots of ΔI and t_D for poly A60 ssDNA at 250 mV and 300 mV. (c) Corresponding histograms of logarithm of t_D to panel b.

Figure 4-12. Transport behaviors of Poly A_{60} and Poly C_{60} ssDNA through ZnO nanopore. (a) 10-second continuous raw current traces for poly A_{60} and poly C_{60} ssDNA through Φ 1.8 nm in 3M KCl electrolyte solution with TE buffer (pH 8.0), filtered at 100 kHz. (b) Scatter plots of ΔI and t_D corresponding to panel a. (c) Histograms of ΔI for poly A_{60} and poly C_{60} translocations. (d) Histograms of logarithm of t_D for poly A_{60} and poly C_{60} translocations.

Chapter 1.

Introduction

1.1. General concept of nanopore technology

As biological systems have been studied at single molecule level due to technology advancse in optics and miniaturation of mechanical systems, various enigmatic subjects such as replication of deoxyribonucleic acid (DNA), transfer of ribonucleic acid (RNA) and transports of macromolecules across the cell have attracted lots of attentions and have been unraveled in details. In particular, transports of various cargo molecules through narrow channels are important phenomena in biological system such as ejection of bacteriophage DNA from a virus head into a host cell and transport of RNA from nucleus to cytoplasm.[1] Based on these phenomena, David Deamer in the University of California proposed the first idea of nanopore sensing method in his notebook at 1989 (figure 1-1).[2] In particular, this idea aimed to DNA sequencing and it suggested that it might be possible to decipher the sequence of single-stranded DNA (ssDNA) through a nanometer-scaled pore, typically called "nanopore", in lipid membrane. As a method for measuring it, Coulter counter method was proposed, which measures ionic currents across the membrane. Coulter counter method is based on reading ion currents in both chambers, which are connected by the orifice in membrane and are filled with electrolyte solution.[3] Originally, the microparticles or the blood cells are main target of this method and pushing these into the orifice causes the resistive spikes or pulses due to the change of electrolyte flows. As the smaller sized holes can be made from micrometer to

nanometer dimensions, Coulter technique can have help to detect the smaller sized target analytes such as nano-sized molecules, individual biomolecules and ions.[3] The specific basic of nanopore measurement is explained later.

This idea was firstly demonstrated in experimental paper at 1996 by D. Deamer (UC Santa Cruz), D. Branton (Harvard University) and J. Kasianowicz (NIST).[4] This first paper demonstrated that polynucleotides, RNA or DNA molecules, were successfully detected using α-hemolysin protein nanopore (33 kD) in lipid bilayer (figure 1-2). The pore size of α-hemolysin pore is 1.4 nm, which is very close to the diameter of ssDNA. As shown in figure 1-2, poly U_{120} RNA,which is composed of continuative arranged 120 uraciles, was detected by the current drops. As seen it, the main merit of nanopore sensing is that it is possible to detect the native state of DNA molecules without any treatments such as fluorescent labeling. Also, it needs the small amounts (< 100 nM) of the target analyte since single molecule can be measured one by one. Since the initial experimental results were reported, nanopore technology has been studied in a variety of ways including various target molecules such as DNA, RNA and protein molecules, various types of nanopores, and other sensing techniques.[5]

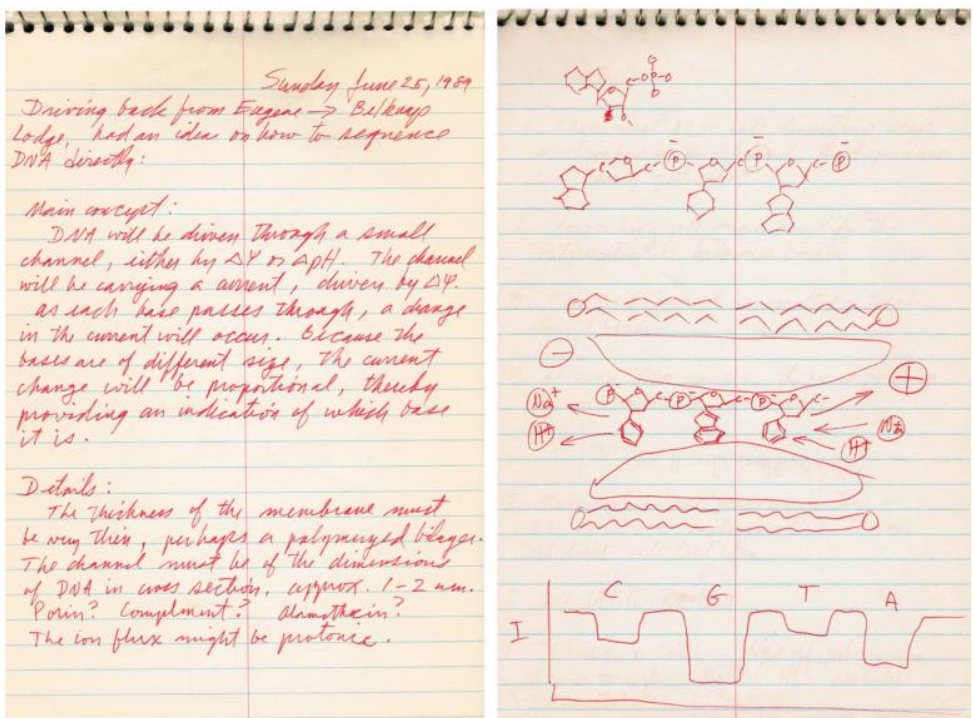

Figure 1-1. Two pages of a notebook. David Deamer illustrated the first scheme of nanopore sequencing concept are shown. Adoped from ref. 2

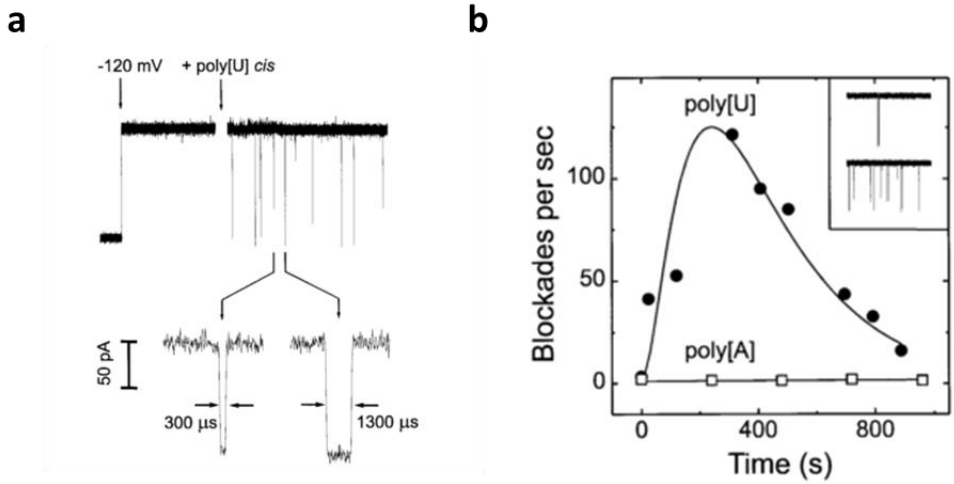

Figure 1-2. The first experimental results of nanopore sensing (a) Ionic current trace of poly U_{120} translocation through α-hemolysin pore at 120 mV. (b) The capture rates of poly A and poly U molecules as a function of experimental times. Adopted from ref. 4

The basic concept of nanopore sensing is illustrated in figure 1-3. First of all, *cis* and *trans* chambers are divided by the formation of thin membrane. Then, the nanometer-sized hole is formed in the insulating membrane and the only channel connecting the two chambers is the nanopore. Both chambers are filled with electrolyte solutions, commonly 1M KCl, and two Ag/AgCl electrodes are inserted into *cis/trans* solutions. When the voltage is applied into two electrodes, the cation (K^+) and anion (Cl^-) pass through the nanopore in opposite directions by the electric field. This ion flow generates "open pore current" as shown figure 1-3a. Because the determinant step of the ionic current is the flow of ions through a nanopore, not the electrochemical reaction of electrode, the open pore current have an Ohmic and linear behavior as a response of the applied voltage below typically 1V. The magnitude of ionic current is dependent on the pore geometry and the electrolyte conductivity, which is discussed later in detail.

For sensing biomolecules, the analyte polymers are inserted in one chamber (figure 1-3b). When the voltage is applied opposite to the charge of the analyte (typically, negative charge of DNA) in the other chamber, the target molecule passes through the nanopore by an electrophoretic force. As the DNA passes through the nanopore, the DNA interferes with the flow of ions, so that a resistive pulse is generated as much as the volume of DNA inside the pore. As shown in figure 1-3b, a large set of resistive pulses is analyzed by at least three important parameters of interest: the mean amplitude of the blockade current (ΔI), the total

duration time of the molecule in the pore (t_D) and the event interval time between two successive events (δt). These parameters are reported to be dependent on the used pore`s dimension and surface charge, biomolecule's diameter and length, solution`s concentration and viscosity.[5]

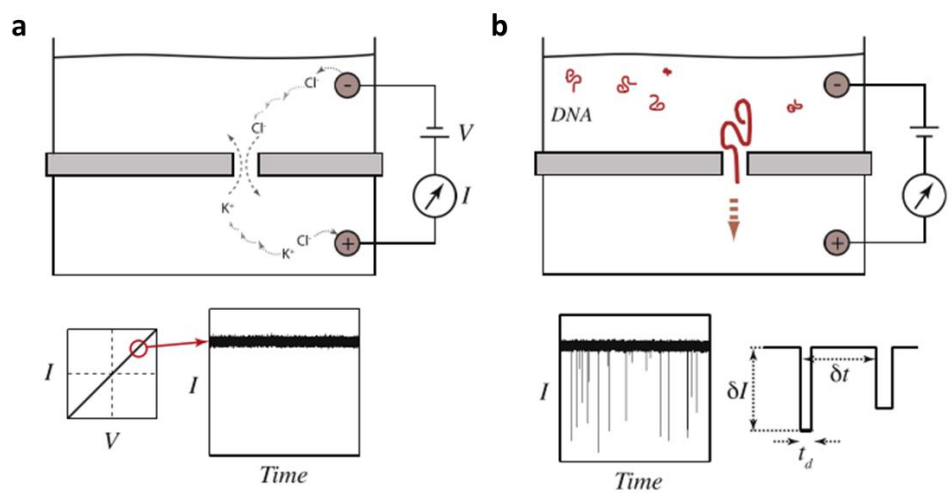

Figure 1-3. The basic concept of nanopore sensing (a) Schematic image of ion channel in electrolyte chamber separated by thin membrane. Both chambers are connected by only the nano-sized hole. After application of voltage across a nanopore, the open pore current is generated by the flows of cation and anion through a pore. (b) Schematic image of ion channel within biomolecules such as DNA. Adopted form ref. 5

1.2. Type of nanopores and brief review

As mentioned earlier, the basis of nanopore sensing technology is how to form the membrane separating two electrolyte reservoirs and the nanopore in it. As a methods for producing such a nanopore device, there are three types of nanopore devices : (i) biological nanopore, which have been studied in the beginning and have used the protein pore with nanometer-scaled hole inside (ii) solid-state nanopore, which have been fabricated by semiconductor technology (iii) hybrid nanopore combining the two nanopore methods, mentioned above.[6] As each nanopore device has different strengths and weaknesses, they have been studied in different directions. In this section, we will describe the advantages and disadvantages of each method and a brief research progress.

1.2.1. Biological nanopore

The biological nanopore is the nanopore device that was used when nanopore technology was first demonstrated in 1996[4], and the technology has been actively studied to date.[2, 5, 7, 8] Basically, a biological nanopore device is composed of a lipid bilayer as the membrane and a protein pore with nanometer-sized channel (figure 1-4). Lipid bilayer membrane is typically located in hundreds micrometer-sized hole in insulating substrates such as Teflon or glass (figure 1-4c and 1-4d).[9] Once the lipid membrane is fabricated in orifice, the protein pore is formed into the

nanopore by implanting the protein pore into the lipid layer. Once only one protein is implanted in lipid membrane, the electrolyte solution including another protein pores is flushed for preventing the formation of further channel in membrane. As seen in figure 1-4a and 1-4b, two kinds of proteins as nanopores commonly used include α-hemolysin and MspA. They have small diameters of less than 2 nm at 1.4 nm and 1.2 nm, respectively. As such, biological nanopores have the advantage of making reproducible nanopores smaller than 2 nm, which cannot yet be replicated in the semiconductor industry. This size is close to the diameter (1.1 nm) of the single-stranded DNA. Thus, while there has been much progress in the analysis of ssDNA in protein nanopore, that is why the analyte of biological nanopore are generally limited to single-stranded DNA and RNA.

The α-hemolysin protein is extracted from Bacteria *Staphylococcus aurus*.[10] The channel in α-hemolysin has the smallest orifice of 1.4 nm and ~ 5 nm long β-barrel, which accommodates up to more than 10 nucleotides at a time (figure 1-4a). Since J. Kasianowicz et al. first demonstrated the translocation of poly A and poly U molecules, most results have focused in characterization of ssRNA and ssDNA homopolymers.[11-13] However, since the channel length of β-barrel is too long to detect specific sequence of DNA, many researchers have tried to form the narrow sensing zone by mutation of amino acid[14] and insertion of another polymer[15]. With the help of this development, a-hemolysin have succeeded in distinguishing each single nucleotide including deoxyadenosine monophosphate (dAMP),

deoxycytidine monophosphate (dCMP), deoxythymidine monophosphate (dTMP) and deoxyguanosine monophosphate (dGMP).[15]

To overcome the limitation of long beta barrel in α-hemolysin, MspA from *Mycobacterium semgnmatis* have been introduced as a candidate nanopore for nucleic acid analysis.[16] Unlike barrel-type α-hemolysin, MspA protein have a conical structure with a confinement of Φ 1.2 diameter and extremely thin sensing zone below 1 nm. For improving the capture rate of ssDNA events, which were interfered by the negative charge of inner constriction in wild-type MspA, three aspartic acids with the negative charge in inner pore were replaced with neutral asparagines using the site-directed mutagenesis method.[16] The resulting engineered MspA, named as M1-NNN-MspA, was able to distinguish the sets of single nucleotides and successive tri-nucleotides.[17]

As such, protein nanopores have been structurally proven to be able to discriminate four nucleotides of DNA, but the biggest obstacle to DNA sequencing application was the rapid transport speed of DNA passage. In order to solve this problem, various methods have been attempted such as immobilization of biotin and streptavidin[18, 19], mutation of amino acid in constriction[20] and hairpin DNA[17] and polymerase enzyme[21-23]. Especially, the introduction of phi 29 polymerase, which regulate the motion of single-strand DNA to one base pair at a time, on biological nanopore platform led the next step closer to DNA sequencing to offer the detecting of current levels related to single-nucleotide movement of the strand.

As seen in figure 1-5, the control of DNA velocity using polymersze enzyme was demonstrated in both biological nanopores including a-hemolysin and MspA. This controlling process involves two dominant steps (figure 1-5b). One is the mechanical unzipping of single DNA molecules by the applied voltage (ii – iii), and the other is the DNA replication process by polymerization of phi 29 enzyme (iv - v). This technique achieved a visible result for DNA seqeuncing in that it could retard the transit time of one nucleotide to more than 1 ms. However, there has been a problem that the signal of four nucleotides can be obtained at any given time due to the limitation of the sensing zone. So, the technique to decode possible combination of each four-nucleotide, 256 quadromer, becomes necessary.[23]

Recently, with the help of these techniques including polymerase and decoding of quadromer signals, the proto-type of nanopore-based sequencer have been developed, which is named as 'Minion'.[24] Although there are many things to be improved in terms of error rate and cost, it is attracting attention as the 3rd generation sequencing technology because it is mobile equipment for the advantages of existing nanopore technology. As shown in figure 1-6a, the minion seqeuncer is small equipment and has the merit of being able to use it only by connecting to usb. Thanks to these mobile properties, results for seqeuncing are reported at various extreme environments such as antarctica and international space station in independent genomics laboratories.[25, 26]

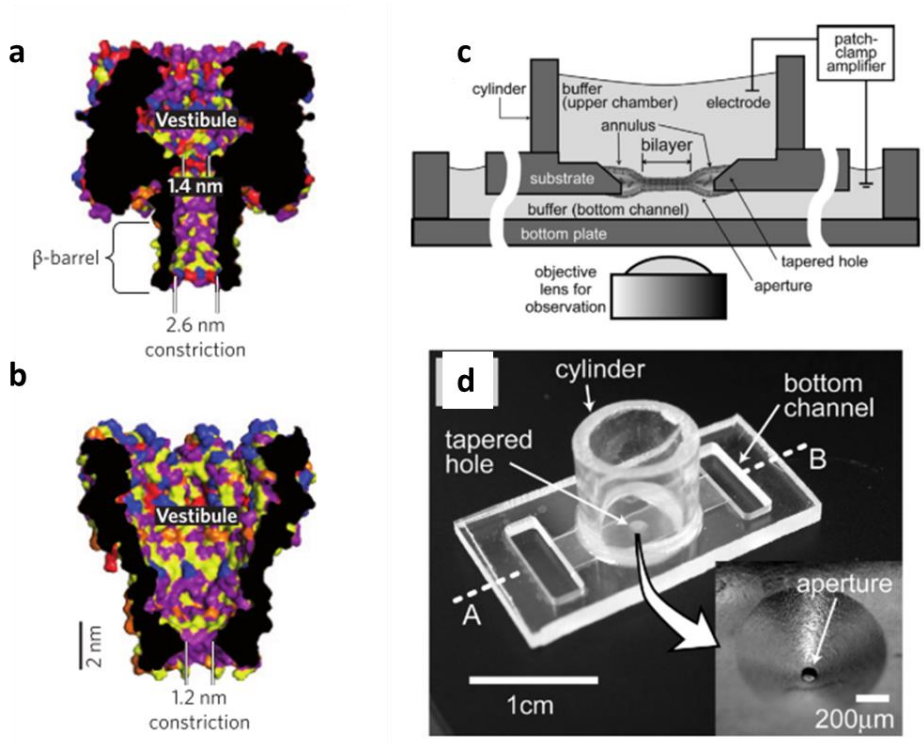

Figure 1-4. Biological nanopores and its measurement setup (a) Cross-sectional structure of α-hemolysin (b) Cross-sectional structure of MspA (c) Schematic diagram of measurement setup in biological nanopore (d) Example of lipid bilayer chip in PMMA supporting. Adopted from ref. 6 and ref. 9

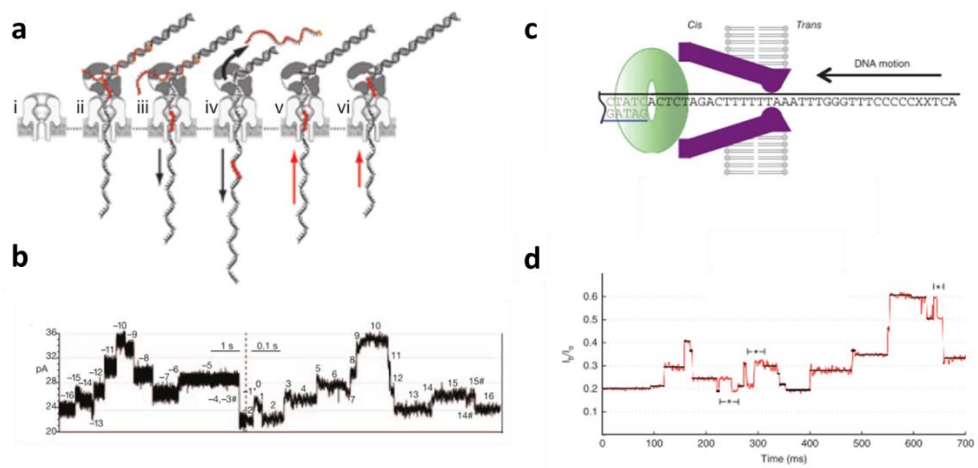

Figure 1-5. Phi 29 Polymerase enzyme-DNA complex in biological nanopores (a) Illustration of forward and reverse ratcheting of DNA through α-hemolysin. (b) Ionic current trace of single DNA molecule during forward and reverse ratcheting process through α-hemolysin. (c) Schematic diagram of phi 29 polymerase combined with single stranded DNA through MspA. (d) Ionic current traces of the sequence of ssDNA molecules during synthesis process through MspA. Adoped from ref. 21 and ref. 22

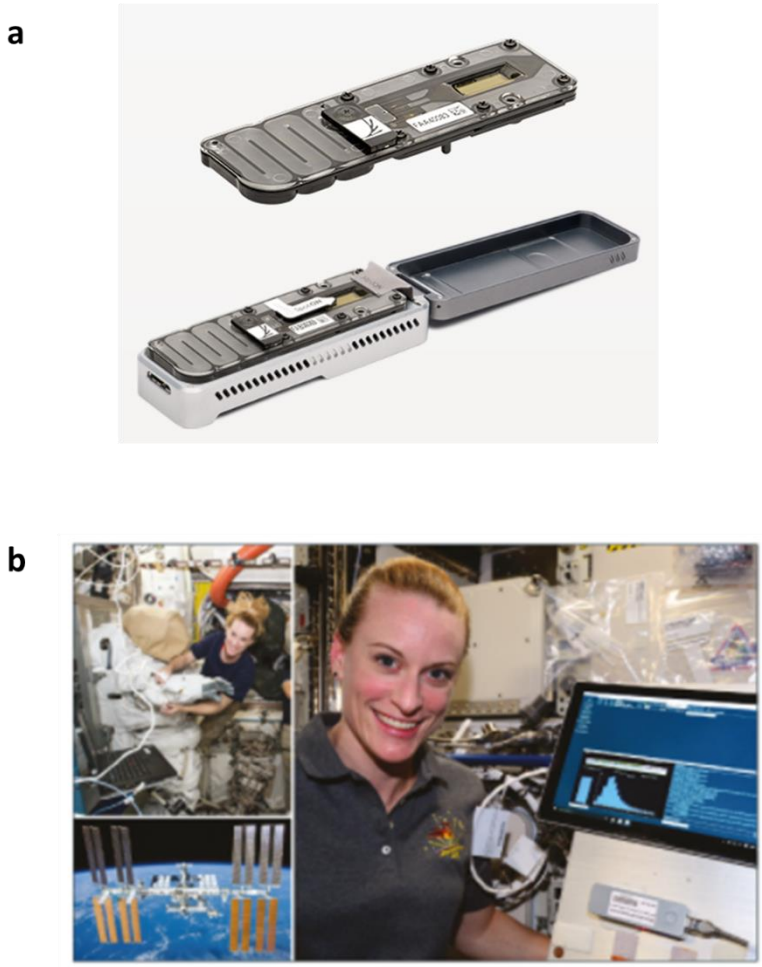

Figure 1-6. Nanopore sequencer and its application (a) Minion nanopore sequencer device and its flow cell from Oxford nanopore (b) First sequencing using Minion under microgravity in international space station. Adopted from Ref. 25 and © nanoporetech.com

1.2.2. Solid-state nanopore

Biological nanopores have the disadvantage of being unable to analyze molecules other than ssDNA, while the fixed size has advantages for ssDNA applications. Furthermore, the lipid bilayer as membrane material to support nanopore protein have poor mechanical and chemical stability, or long time stability. As nano-structures can be built below 10 nm due to the advance of nanotechnology, solid-state nanopore has emerged to obtain the mechanical and chemical robustness with controllability of pore-dimension.[7, 27-29] Basically, the development of a solid-state nanopore is aided by the fabrication of forming a free-standing SiN_x or SiO_2 membrane of a few tens of nm scale on a Si substrate using anisotropic KOH etching. In the first solid-state nanopore, focused ion beam (FIB) sculpting method was performed on the freestanding membrane on Si substrate (figure 1-7a and 1-7b).[30] This system included the ion beam generator and the single ion detector to turn off ion beam when single ion was detected. Such a device demonstrated the first double stranded DNA of 500 bp translocation through 5 nm SiN pore in 1 M KCl.[30]

In 2003, new technique to make the nanometer-sized pore in free-standing membrane was developed using transmission electron beam microscope (TEM), as shown in figure 1-7c and 1-7d.[31] This technique included the pore drilling process by focused e-beam radiation with high intensity and the pore shrinkage process by

delocalized e-beam radiation with low intensity. This method is more widely used nowadays because it does not require any special manipulation of the equipment and can adjust the pore size more precisely, compared to FIB-based method.[27] Still, the mechanism of nanopore perforation in TEM is not clearly known, but it is a tentative conclusion that the electron beam with high energy induces a direct atomic displacement as sputtering mechanism.[32]

The electron beam or ion beam drilling method has the disadvantage of being able to control the size of the actual pore while it can be an adsorption site for hydrocabrons or contaminations present in the vacuum condition.[33] Recently, an alternative nanopore creation method using dielectric breakdown of dielectric membrane is proposed.[34, 35] In figure 1-8a, this method use the high electric field applied across the membrane with few-tens of nanometer to induce vacancy sites.[34] Similar to typical dielectric break down in solid-state environment, which is caused by localized leakage currents through localized structural detect or charge traps under high electric field[36], the accumulation of traps by both cations and anions in electrolyte solution induces bond breakage and finally leads to the creation of nano-sized pore. To precisely control the nanopore size sub 1 to 3 nm, Hitach Ltd. proposed and evaluated a technique named as multilevel-pulse-voltage injection (MPVI).[35, 37] In dielectric breakdown operation, the created pore size is estimated through ionic current reading. However, the estimation of precise pore size is difficult under high electric field due to additional leakage current through the

membrane. MPVI process involves the pore generation step under relatively high voltage (~7 V) and, after the pore nucleation, the pore enlargement step under relatively low voltage (~3 V), as presented in figure 1-8b.[35] This technique produces sub 1 to 2 nm SiN_x nanopores, which is suitable for detect ssDNA translocations. In sum, all nanopore fabrication technique have demonstrated creating nano-scale pore in solid-state membrane and controlling the dimension of the created nanopore to desired size in nm resolution.

In addition to the 3rd generation sequencing application, the solid-state nanopore have drawn lots of attractions due to wide applications to the biological and biomedical detections targeting other biomolecules such as single proteins, protein-protein complex and DNA-protein complex.[38-40] But, the researches in this thesis focuses on DNA sequencing applications of solid-state nanopores. As described above, solid-state nanopores still have some issues to address while biological nanopores show visible performance of DNA sequencing. A detailed explanation is given in chapter 2.

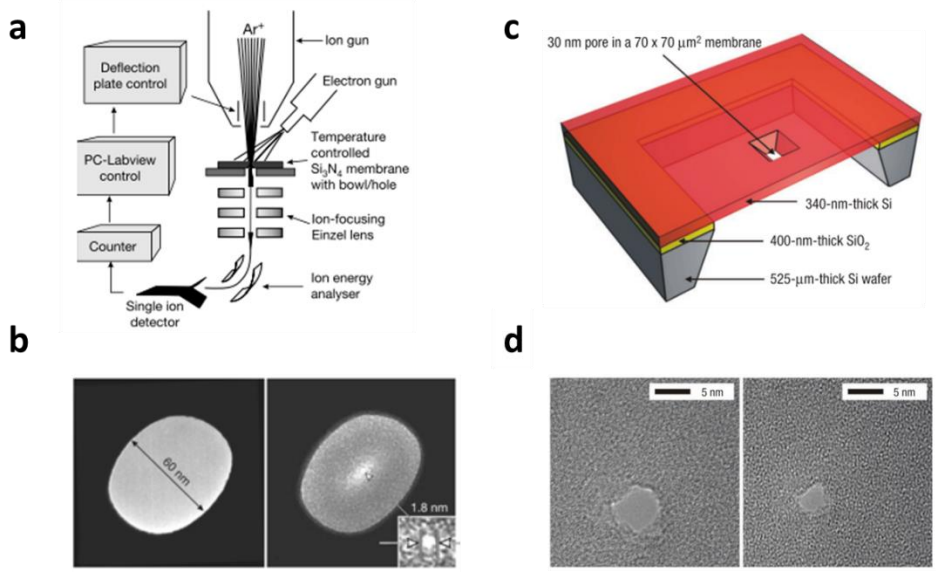

Figure 1-7. Fabrication method of solid-state nanopores (a) Focused ion beam sculpting method by custom-designed feedback system to control the pore size (b) TEM images of nanopore by ion-beam sculpting method (c) Schematic view of solid-state nanopore device based on Si substrate. (d) Pore diameter control in SiO2 membrane by electron beam radiation. Adopted from ref. 30 and ref. 31

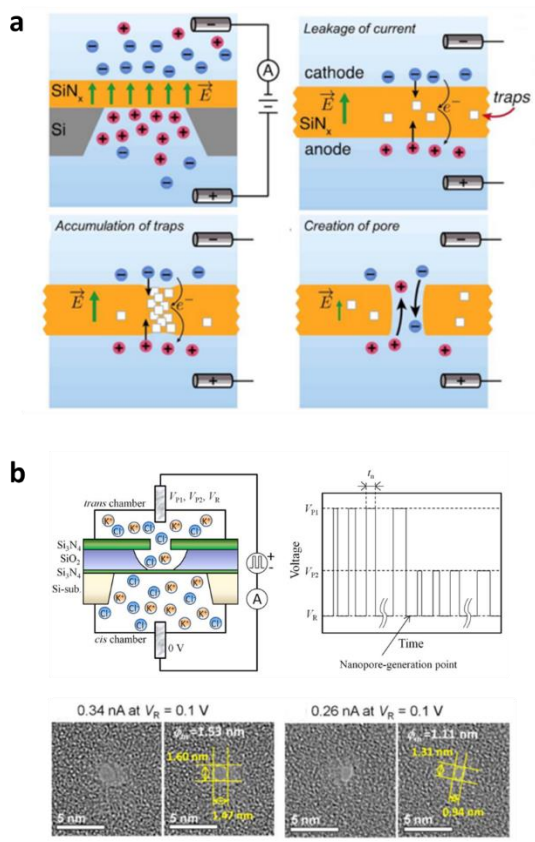

Figure 1-8. Nanopore perforation method by dielectric breakdown (a) Mechanism of nanopore formation by controlled dielectric breakdown (b) Setup for multilevel pulse-voltage injection via dielectric breakdown and TEM images of sub 1 to 2 nm nanopores using this method. Adopted from ref. 34 and ref. 35

1.2.3. Hybrid nanopore

Although solid-state nanopores ensure chemical mechanical stability due to solid-state membranes, they can not reproducibly provide the dimensions of nanopores made by the above-described methods. Hybrid nanopore pursue the combination of novel robustness from solid-state membrane and the fixed pore dimension and biological affinity from organic pore (figure 1-9).[41-44] The first hybrid nanopore was the integration of α-hemolysin protein pore on SiN_x membrane (figure 1-9a).[41] After SiN_x nanopore was fabricated with a diameter of ~3 nm, α-hemolysin protein pore was attached with dsDNA molecule for protein insertion. As presented in (iii) step of figure 1-9b, the formation of hybrid nanopore represented the stable and low ionic current level. This device demonstrate the functionality to translocate ssDNA molecules, but the hybrid nanopore have a still challenging issue of imperfect insertion of α-HL into SiN_x nanopore, which is being considered as a leakage current source related to electrical noise level.

As an alternative hybrid nanopore, DNA origami technology was introduced to provide the designed and precisely fabricated nano-sized hole with the desired structure.[43] DNA origami structure is made by the complementary interactions of DNA nucleotides, where a long ssDNA named as scaffold is used to fabricate the programmed structure by folding and binding according to the nucleotide sequence.[45] As shown in figure 1-9b, DNA origami with plate-structure was inserted on the prepared SiN_x pore by electrophoretic driven.[44] Like the hybrid nanopore, it

shows a lower level current than the original after the insertion of DNA origami. Origami nanopore has the advantage that it can pass various protein molecules such as streptavidin and immunoglobulin G as well as dsDNA because it can make pore dimension as desired.[44] But, origami-hybridized device needs further technological advances since it also represents poor signal to noise ratio of biomolecule detections owing to fluctuated current noise by ion current leakages in the interface between SiNx pore and DNA origami.

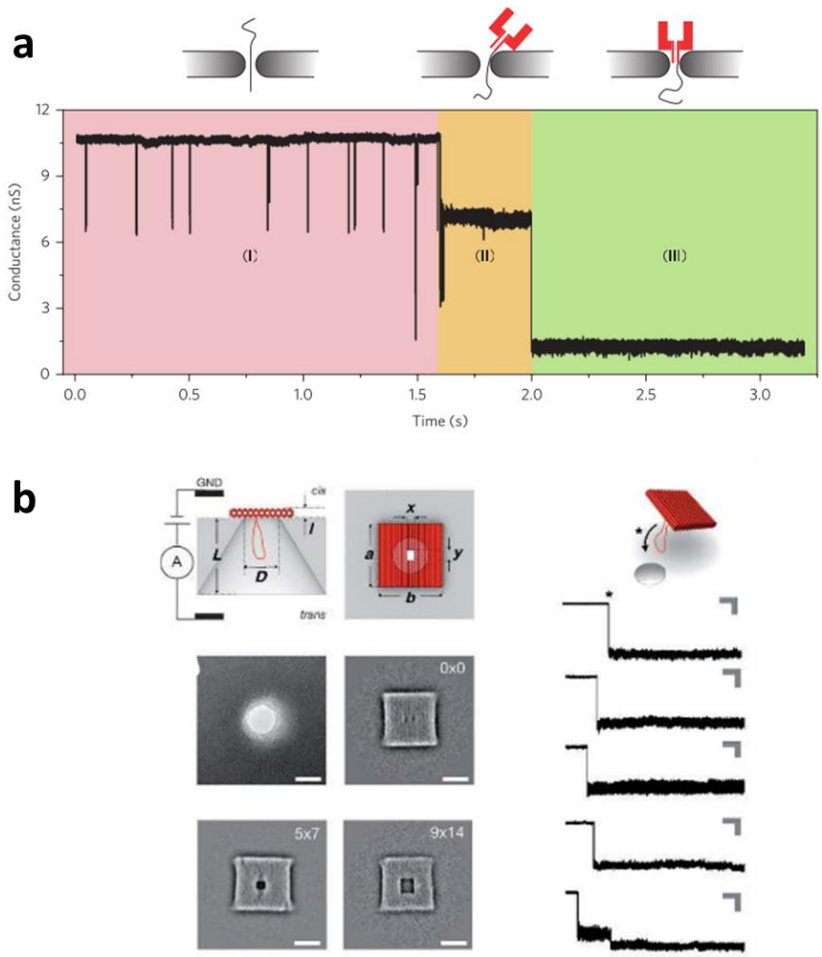

Figure 1-9. Hybrid nanopores (a) Hybrid nanopore formation sequence integrated with α-hemolysin protein and corresponding ionic current traces (b) Integration of DNA origami with nanoplate structure and raw ion current trace after DNA origami insertion .Adopted from ref. 41 and ref. 44

1.3. Nanopore technology for DNA sequencing

As the discovery of DNA structure and the understanding complexity and diversity of genomes have been studied[46, 47], DNA sequencing technology has attracted more attention for applications to personal diseases or personalized medicine. As mentioned earlier, the structure of DNA is composed of phosphate backbone with deoxyribose and four-type of nucleotides named as adenine, guanine, thymine and cytosine.[48] In natural state, DNA generally have the double helix structure by the complementary base paring between purines (A, G) and pyremideines (T, C). Due to the specific bonding sites of hydrogen bonds, the complementary base paring is limited in A-T and G-C parings. Since the sequence of the nucleotides arranged in these DNAs results in RNA transcription and protein expression, decoding the nucleotide sequence, DNA sequencing, have been important.

Since the first successful technique for DNA sequencing, named as 'Sanger method' was developed in 1970`s by Sanger[49], it has dominated the field of DNA sequencing by the early 2000`s.[50] The classical Sanger method demands a ss DNA template, a DNA primer, a DNA polymerase, deoxy-nucleosidetriphosphates (dNTPs) for polymerase chain reaction and di-deoxy-nucleotidetriphosphates (ddNTPs) for terminatation of DNA strand elongation.[49] As seen in figure 1-10, DNA strands with different length and sequence termination were producted through repeated PCR amplification and termination reactions. The sequence by the

difference of lengths was determined by gel electrophoresis or further improved capillary electrophoresis.[51] Despite 30 years of technological development, the Sanger sequencing have its fundamental limitations of the short read-length by low accuracy of termination reaction in long DNA strand (>1000 bp) and high costs by repetitive amplification reaction. So, the need of new strategies for DNA sequencing has grown in conjunction with the Human Genome Project.

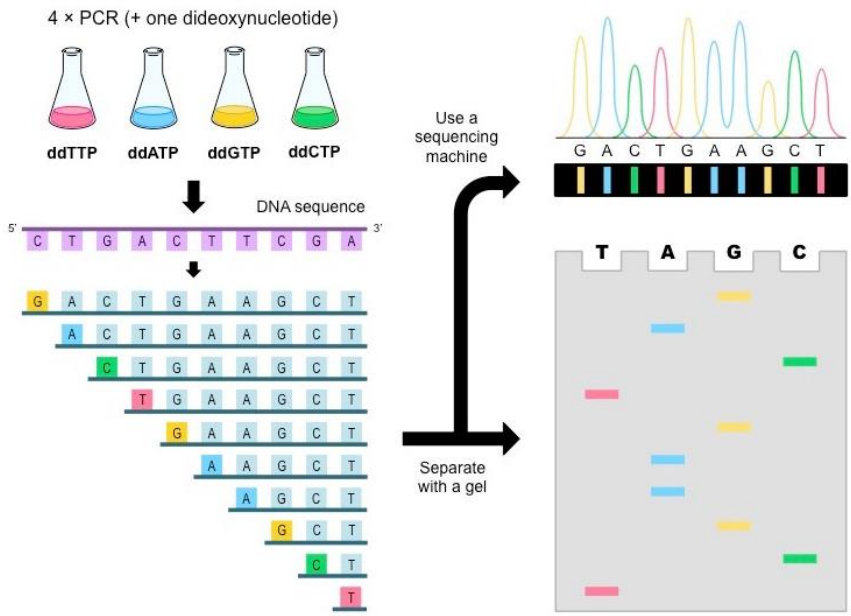

Figure 1-10. DNA sequencing procedure via the Sanger method. Adopted from © http://ib.bioninja.com.au

1.3.1. Next generation sequencing technology

In the beginning of the Human Genome Project, conventional Sanger sequencing method have a important role to identify three billion nucleotides in human genome and to investigate the genetic roots of disease. However, because of the limitation of Sanger method in a point of cost and operation time, the need of alternative DNA sequencing technique for high speed and low cost have been grown.[52, 53] These 2nd and 3rd generation sequencing technologies have been more prompted by the $ 1,000 genome challenge of the National Institutes of Health in 2004.

After Sanger termination method as 1st sequencing mehtod, 2nd sequencing methods have been developed based on two categorized technique : sequencing by synthesis (SBS) and sequencing by ligation (SBL).[51] In SBS method, the sequence of target DNA is identified by signals of fluorescence or ionic concentration change when a nucleotide is incorporated into an elongating strand by polymerase reaction. Representative instruments based SBS approach include 454 pyrosequencing (Roche), Solexa technology (Illumina) and Ion Torrent (Ion Torrent System Inc.). In SBL method, a probe sequence, which is combined with fluorescent chemical compound, hybridizes to a DNA template and is ligated to an adjacent oligonucleotide for fluorescent imaging. Representative instrument based SBL approach is SOLiD platform (Thermo Fisher Scienfic). Although a variety of sequencing technologies have been

developed, the second generation sequencing technology is now dominated by 'Solexa technology' in Illumina.

Figure 1-11 shows the principle and procedure of Illumina`s sequencing instrument. In this approach, DNA templates are immobilized on the solid substrate and the sequence of each nucleotide is identified by the four fluorescent signals, respectively. The target DNA molecules, including PCR primer fragment, are attached on solid support for 'bridge PCR amplification'. Both forward and reverse primers can interact with other nearby primers and form a bridge structure. From the immobilized primers, a second strand is replicated and unanchored DNA fragment is removed by PCR process. After several rounds of PCR amplification, 100 to 200 millions clonal cluster are grown in the separated location.[52] For identifying the sequence of nulceotides, cyclic reversible termination (CRT) method is used, which involves DNA polymerase, nucleotide incorporation, fluorescence imaging and nucleotide cleavage.[53] After the creation of DNA clusters, modified polymerase is bounded in the primer part and just one fluorescently modified nucleotide is incorporated by synthesis. Following synthesis, the remaining unbound nucleotides are removed by washing. Fluorescent imaging is then conducted to identity the incorporated nucleotide. The four colors of four A, T, G, C nucleotides are detected by total internal reflection fluorescence imaging. Then, a cleavage step is progressed to

remove the terminating/inhibiting group and the fluorescent dye. Additional washing is performed before starting the next incorporation step. As repetition of these process, the sequence of DNA is determined one by one. In this approach, the throughput of DNA sequencing is improved and the high accuracy of 99.5 % is obtained in short read-length up to 300 bp.[53]

In same SBS approaches, 454 pyrosequencing method and Ion Torrent sequencing method are also released in Roche and Ion Torrent, respectively (figure 1-12). Unlike the CRT method used for imaging in Solexa technology, these two method use single-nucleotide addition (SNA), where each of the four nucleotides is incorporated into DNA strand continuously in polymerase reaction to ensure only one dNTP is responsible for one signal. As the first 2nd instrument, 454 pyrosequencing device was developed in 2005.[54] In this approach, DNA templates are bound into beads containg an enzyme cocktail as shown in figure 1-12a. As a dNTP is incorporated into a template, an enzymatic reaction generates the release of an inorganic pyrophosphate, resulting in a bioluminescence light.[53]

While these methods described above are sequencing method by optical sensing, the Ion Torrent was the first 2nd sequencing platform based on semiconductor device with H^+ ion sensing.[55] Rather than detecting a bioluminescence signal from enzyme reaction, Ion Torrent device measured the H^+ ions that are generated by the incorporation of dNTP. The H^+ release induces

a 0.02 change in pH, which is detected by an integrated complementary metal-oxide semiconductor (CMOS) and an ion-sensitive field-effect transistor (ISFET) device.

With the advancement of these sequencing technologies, the DNA sequencing platform has achieved the desired low cost and high throughput, especially in Illumina instruments.[53] However, since these techniques utilize a reaction in a short fragment unit, there is a fundamental limitation of short read-length. This limitation is motivating for a third-generation sequencing platform that can achieve long read lengths and real-time sequencing.

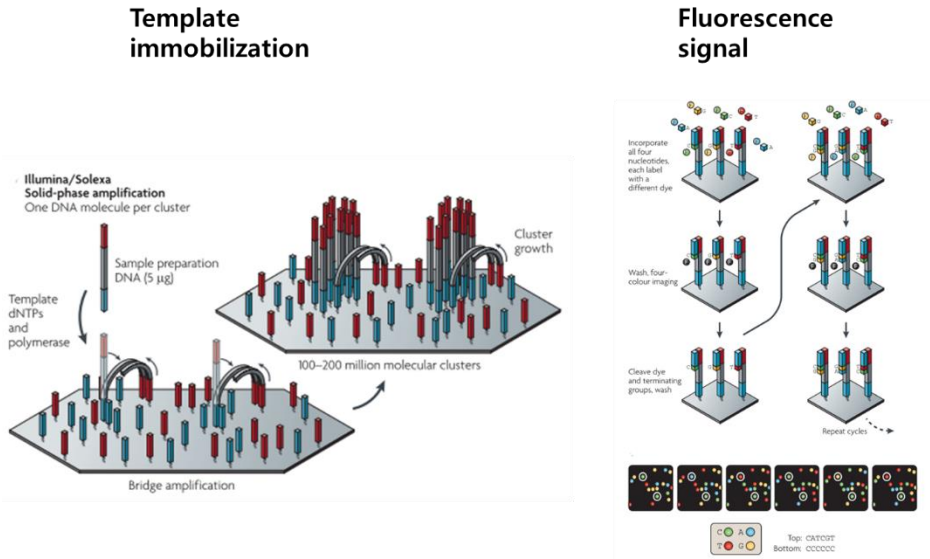

Figure 1-11. Solexa technology based on sequencing by synthesis in Illumina. It has two process; one is the immobilization of DNA template and the other is the detection of fluorescence signal. Adopted from ref. 52

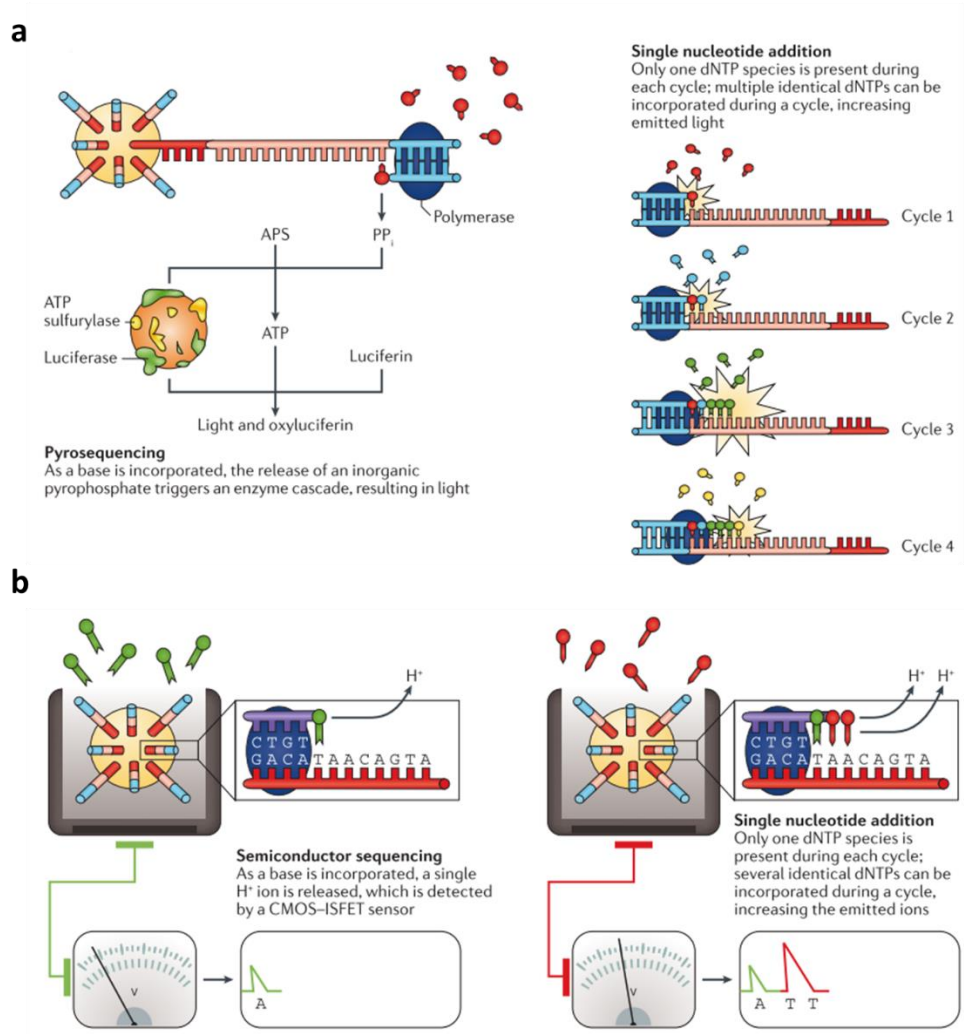

Figure 1-12. 2nd sequencing methods based on sequencing by synthesis (a) 454 pyrosequencing in Roche (b) Ion Torrent sequencing method in Ion Torrent. Adopted from ref. 53

1.3.2. Nanopore sequencing as 3rd sequencing platform

Human genomes have been understood to have many long repetitive arrangements with high complexity structural variations that are related to genomic information.[53] To decode these complex elements, long-read sequencing must be required more than several kilobases, but the developed 2nd sequencing platform can be operated up to a maximum of 1000 bp. Therefore, 3rd generation sequencing platforms have been developed for real-time sequencing of single molecules.[56] There are currently two commercial real time sequencing technologies; one is single molecule real-time sequencing (SMRT), which uses zero-mode waveguide method in Pacific Biosciences[57] and the other is nanopore sequencing technology, which is the subject of this thesis (figure 1-13). SMRT uses single fluorescence detection method during the incorporation of nucleotide in polymerase synthesis. However, a signal of single fluorescene dye cannot be detected due to background fluorescence noise. With the help of zero-mode waveguide, the signal was improved by a factor of 1000 on a 50 nm diameter metal wall (figure 1-13b). This technology allows high through put and long read length up to 10 kbp because synthesis of single nucleotide and fluorescence reading are consecutively performed on the immobilized polymerase in nanowall without additional washing or amplification process.[53]

The nanopore sequencing platform is also operated on single molecule based real time sequencing. While other techniques read indirect signals of fluorescence or H + ions that occur during the incorporation of a single nucleotide, nanopore

platform directly detect a native ssDNA molecules by ion current change of four nucleotides.[2] Although the cost of nanopore sequencing ($30k/genome) is higher than that of the second-generation sequencing technology, which is close to $ 1000 genome from Illumina`s platform, nanopore platform that does not require additional amplification or fluorescence labeling have the potential to provide lower cost. In terms of read-length, table 1-1 shows the summary of read-length in existing DNA sequencing platforms and nanopore platform reported the longest read-length, 200 kbp.[53] Such long read-length platform can be useful of identifying sequences of repetitive and complex genomes and spanning entire mRNA transcripts. In addition, since the sequence reading occurs on the nanometer scale, it has the advantage of miniaturization of the device and its portability.[58] So far, technological progress in terms of cost and error rate must be needed for commercialization as 3rd generation sequencer. But, the value of nanopore sequencing is becoming more and more important as much research is currently being carried out in the lab unit.

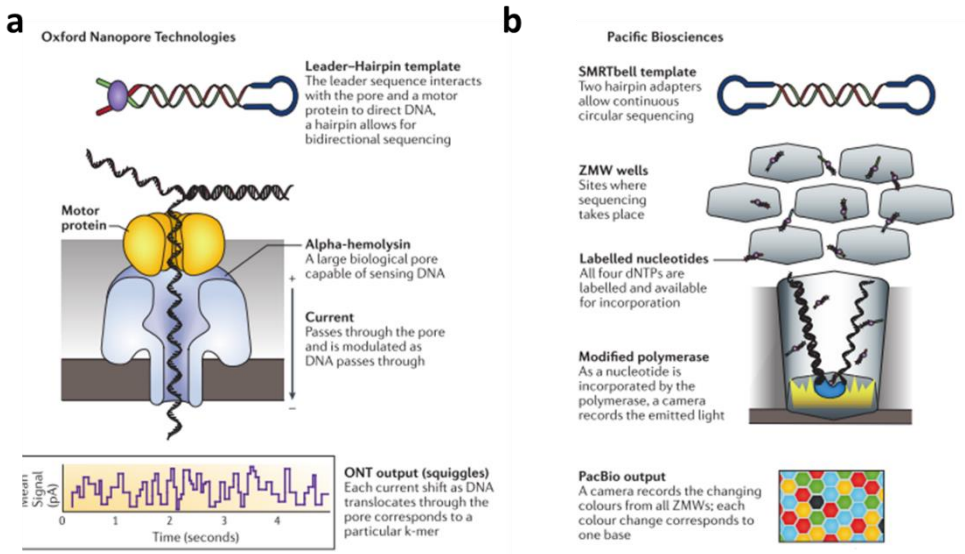

Figure 1-13. 3rd generation sequencing technology based on single molecule real time sequencing (a) Nanopore sequencing from Oxford nanopore on a-hemolysin biological pore with polymerase. (b) Single molecule real time sequencing method based on zero mode waveguide from PacBio. Adoped from ref. 53

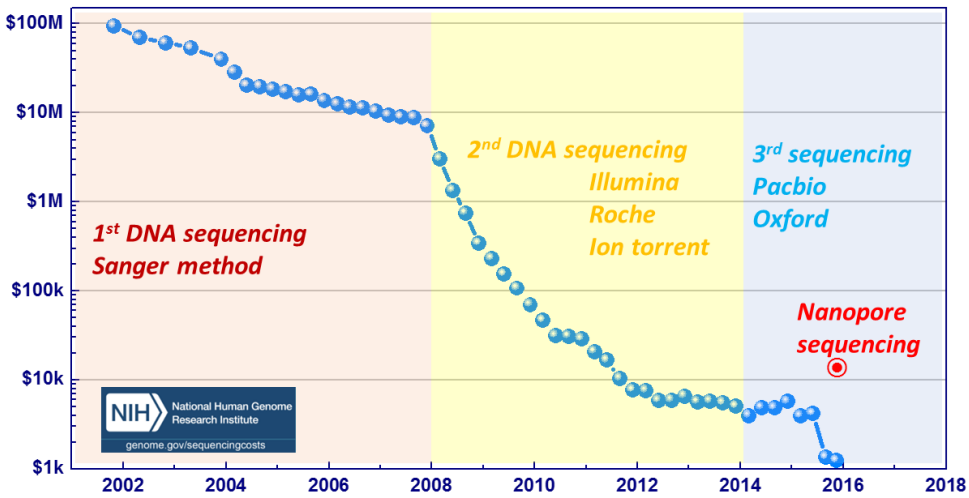

Figure 1-14. Growth trends of DNA sequencing technology in terms of cost per genome. Adopted from © gonome.gov

Table 1-1. Summary of DNA sequencing platforms as a view of read-length

1st sequencing		2nd sequencing		3rd sequencing	
Platform	**Read length**	**Platform**	**Read length**	**Platform**	**Read length**
Sanger`s method	~800 bp	Roche (Pyrosequencing)	400 bp	Oxford nanopore (MinIon)	100 bp – 200 kbp
		Illumina (Sequencing by synthesis)	150~300 bp	Pacific Bio (Zero mode guide by fluorescence)	8 - 12 kbp
		Ion Torrent (Ionic sensitive FET)	200~400 bp		

1.4. Outline of dissertation

This dissertation contains the research results to improve ionic current noise and sensitivities of solid-state nanopore through the upgradation of substrate and membrane materials for DNA sequencing applications.

Chapter 1 describes a general overview about the history and basic principle of nanopore detection. In particular, the brief fundamental of nanopore sensing method for DNA sequencing applications and the simple comparison of existing next generation DNA sequencing platforms are introduced. Chapter 2 consists of the overall review about the main issues and its solutions to utilize the DNA sequencing application in solid-state nanopore. These issues include ionic current noise, spatial and temporal resolution. Various experimental and theoretical approaches to solve each obstacles are introduced. In chapter 3, experimental results on a platform to establish low noise and high spatial resolution using two dimensional material, especially boron nitride (BN), is described. In particular, we propose a novel fabrication method to improve the flicker noise that has been a problem in 2D nanopores. Chapter 4 reports the research results of applying ZnO material as an alternative nanopore device to improve temporal resolution. Through the DNA translocation experiment, it highlights the slowing down effect of the DNA velocity. Finally, chapter 5 summarizes the results of this study and suggests the related future works in this study.

Reference

1. Berk A Lodish H, Zipursky SL, et al, Molecular Cell Biology. *New York: W. H. Freeman*, 2000. Section 11.4.
2. D. Deamer, et al., Three decades of nanopore sequencing. *Nat Biotechnol*, 2016. **34**(5): 518-24.
3. Hagan Bayley and Charles R. Martin, Resistive-Pulse SensingFrom Microbes to Molecules. *Chemical Reviews*, 2000. **100**(7): 2575-2594.
4. J. J. Kasianowicz, et al., Characterization of individual polynucleotide molecules using a membrane channel. *Proceedings of the National Academy of Sciences of the United States of America*, 1996. **93**(24): 13770-13773.
5. M. Wanunu, Nanopores: A journey towards DNA sequencing. *Phys Life Rev*, 2012. **9**(2): 125-58.
6. Bala Murali Venkatesan and Rashid Bashir, Nanopore sensors for nucleic acid analysis. *Nat Nano*, 2011. **6**(10): 615-624.
7. W. Shi, et al., Nanopore Sensing. *Anal Chem*, 2017. **89**(1): 157-188.
8. F. Haque, et al., Solid-State and Biological Nanopore for Real-Time Sensing of Single Chemical and Sequencing of DNA. *Nano Today*, 2013. **8**(1): 56-74.
9. H. Suzuki, et al., Electrophysiological recordings of single ion channels in planar lipid bilayers using a polymethyl methacrylate microfluidic chip. *Biosens Bioelectron*, 2007. **22**(6): 1111-5.
10. J E Gouaux, et al., Subunit stoichiometry of staphylococcal alpha-hemolysin in crystals and on membranes: a heptameric transmembrane

pore. *Proceedings of the National Academy of Sciences*, 1994. **91**(26): 12828-12831.

11. M. Akeson, et al., Microsecond time-scale discrimination among polycytidylic acid, polyadenylic acid, and polyuridylic acid as homopolymers or as segments within single RNA molecules. *Biophysical Journal*, 1999. **77**(6): 3227-3233.
12. D. W. Deamer and D. Branton, Characterization of nucleic acids by nanopore analysis. *Accounts of Chemical Research*, 2002. **35**(10): 817-825.
13. D. W. Deamer and M. Akeson, Nanopores and nucleic acids: prospects for ultrarapid sequencing. *Trends in Biotechnology*, 2000. **18**(4): 147-151.
14. Stefan Howorka, et al., Sequence-specific detection of individual DNA strands using engineered nanopores. *Nat Biotech*, 2001. **19**(7): 636-639.
15. J. Clarke, et al., Continuous base identification for single-molecule nanopore DNA sequencing. *Nat Nanotechnol*, 2009. **4**(4): 265-70.
16. Tom Z. Butler, et al., Single-molecule DNA detection with an engineered MspA protein nanopore. *Proceedings of the National Academy of Sciences*, 2008. **105**(52): 20647-20652.
17. I. M. Derrington, et al., Nanopore DNA sequencing with MspA. *Proceedings of the National Academy of Sciences of the United States of America*, 2010. **107**(37): 16060-16065.
18. Elizabeth A. Manrao, et al., Nucleotide Discrimination with DNA Immobilized in the MspA Nanopore. *PLOS ONE*, 2011. **6**(10): e25723.
19. R. F. Purnell and J. J. Schmidt, Discrimination of Single Base Substitutions

in a DNA Strand Immobilized in a Biological Nanopore. *Acs Nano*, 2009. **3**(9): 2533-2538.

20. M. Rincon-Restrepo, et al., Controlled translocation of individual DNA molecules through protein nanopores with engineered molecular brakes. *Nano Lett*, 2011. **11**(2): 746-50.
21. Elizabeth A. Manrao, et al., Reading DNA at single-nucleotide resolution with a mutant MspA nanopore and phi29 DNA polymerase. *Nat Biotech*, 2012. **30**(4): 349-353.
22. Gerald M. Cherf, et al., Automated forward and reverse ratcheting of DNA in a nanopore at 5-A precision. *Nat Biotech*, 2012. **30**(4): 344-348.
23. Andrew H. Laszlo, et al., Decoding long nanopore sequencing reads of natural DNA. *Nat Biotech*, 2014. **32**(8): 829-833.
24. Miten Jain, et al., Improved data analysis for the MinION nanopore sequencer. *Nature Methods*, 2015. **12**(4): 351-356.
25. Alexa B. R. McIntyre, et al., Nanopore sequencing in microgravity. *npj Microgravity*, 2016. **2**: 16035.
26. S. S. Johnson, et al., Real-Time DNA Sequencing in the Antarctic Dry Valleys Using the Oxford Nanopore Sequencer. *J Biomol Tech*, 2017. **28**(1): 2-7.
27. Cees Dekker, Solid-state nanopores. *Nat Nano*, 2007. **2**(4): 209-215.
28. Stephanie J. Heerema and Cees Dekker, Graphene nanodevices for DNA sequencing. *Nat Nano*, 2016. **11**(2): 127-136.
29. Y. Feng, et al., Nanopore-based fourth-generation DNA sequencing technology. *Genomics Proteomics Bioinformatics*, 2015. **13**(1): 4-16.
30. J. Li, et al., Ion-beam sculpting at nanometre length scales. *Nature*, 2001.

412(6843): 166-169.

31. A. J. Storm, et al., Fabrication of solid-state nanopores with single-nanometre precision. *Nature Materials*, 2003. **2**(8): 537-540.
32. Hyun-Mi Kim, et al., Theoretical and experimental study of nanopore drilling by a focused electron beam in transmission electron microscopy. *Nanotechnology*, 2011. **22**(27): 275303.
33. Aleksandra Radenovic, et al., Fabrication of 10 nm diameter hydrocarbon nanopores. *Applied Physics Letters*, 2008. **93**(18): 183101.
34. Harold Kwok, et al., Nanopore Fabrication by Controlled Dielectric Breakdown. *PLOS ONE*, 2014. **9**(3): e92880.
35. I. Yanagi, et al., Fabricating nanopores with diameters of sub-1 nm to 3 nm using multilevel pulse-voltage injection. *Sci Rep*, 2014. **4**: 5000.
36. H. Fröhlich and B. V. Paranjape, Dielectric Breakdown in Solids. *Proceedings of the Physical Society. Section B*, 1956. **69**(1): 21.
37. Y. Goto, et al., Integrated solid-state nanopore platform for nanopore fabrication via dielectric breakdown, DNA-speed deceleration and noise reduction. *Sci Rep*, 2016. **6**: 31324.
38. A. H. Squires, et al., Single-Molecule Characterization of DNA–Protein Interactions Using Nanopore Biosensors. 2016.
39. Dong-Kyu Kwak, et al., Probing the Small-Molecule Inhibition of an Anticancer Therapeutic Protein-Protein Interaction Using a Solid-State Nanopore. *Angewandte Chemie International Edition*, 2016. **55**(19): 5713-5717.
40. Benjamin N. Miles, et al., Single molecule sensing with solid-state nanopores: novel materials, methods, and applications. *Chemical Society*

Reviews, 2013. **42**(1): 15-28.

41. A. R. Hall, et al., Hybrid pore formation by directed insertion of alpha-haemolysin into solid-state nanopores. *Nature Nanotechnology*, 2010. **5**(12): 874-877.
42. N. A. Bell, et al., DNA origami nanopores. *Nano Lett*, 2012. **12**(1): 512-7.
43. Nicholas A. W. Bell and Ulrich F. Keyser, Nanopores formed by DNA origami: A review. *FEBS Letters*, 2014. **588**(19): 3564-3570.
44. R. Wei, et al., DNA origami gatekeepers for solid-state nanopores. *Angew Chem Int Ed Engl*, 2012. **51**(20): 4864-7.
45. Carlos Ernesto Castro, et al., A primer to scaffolded DNA origami. *Nat Meth*, 2011. **8**(3): 221-229.
46. J. D. Watson and F. H. C. Crick, Molecular Structure of Nucleic Acids: A Structure for Deoxyribose Nucleic Acid. *Nature*, 1953. **171**(4356): 737-738.
47. R. Dahm, Discovering DNA: Friedrich Miescher and the early years of nucleic acid research. *Hum Genet*, 2008. **122**(6): 565-81.
48. Berk A Lodish H, Zipursky SL, et al., Molecular Cell Biology. *New York: W. H. Freeman*, 2000. **4th edition**(Section 4.1 Structure of Nucleic Acids).
49. F. Sanger, et al., Nucleotide sequence of bacteriophage [phi]X174 DNA. *Nature*, 1977. **265**(5596): 687-695.
50. I. I. I. Clyde A. Hutchison, DNA sequencing: bench to bedside and beyond †. *Nucleic Acids Research*, 2007. **35**(18): 6227-6237.
51. Jay Shendure and Hanlee Ji, Next-generation DNA sequencing. *Nature Biotechnology*, 2008. **26**(10): 1135-1145.

52. M. L. Metzker, Sequencing technologies - the next generation. *Nat Rev Genet*, 2010. **11**(1): 31-46.

53. S. Goodwin, et al., Coming of age: ten years of next-generation sequencing technologies. *Nat Rev Genet*, 2016. **17**(6): 333-51.

54. Marcel Margulies, et al., Genome sequencing in microfabricated high-density picolitre reactors. *Nature*, 2005. **437**(7057): 376-380.

55. Jonathan M. Rothberg, et al., An integrated semiconductor device enabling non-optical genome sequencing. *Nature*, 2011. **475**(7356): 348-352.

56. E. R. Mardis, DNA sequencing technologies: 2006-2016. *Nat Protoc*, 2017. **12**(2): 213-218.

57. John Eid, et al., Real-Time DNA Sequencing from Single Polymerase Molecules. *Science*, 2009. **323**(5910): 133-138.

58. Alan C. Ward and Wonyong Kim, MinION™: New, Long Read, Portable Nucleic Acid Sequencing Device. *Journal of Bacteriology and Virology*, 2015. **45**(4): 285.

Chapter 2.

Review on solid-state nanopore

2.1. Current issues of solid-state nanopore

As mentioned in chapter 1, biological nanopore have been developed to provide a proto-type DNA sequencer that is close to commercialization.[1] On the contrary, the progress of solid-state nanopore has been much slow and limited to merely detecting either the translocation of DNA molecules or the DNA-protein interactions untill now, although solid-state nanopore platforms offer obvious advantages over biological nanopore such as mechanical, chemical, long-term stability and pore dimension controllability.[2, 3] Figure 2-1 summarize the historical timeline of research achievements relate to DNA sequencing applications in biological nanopore and solid-state nanopore, respectively. Comparing the same research results, it can be seen that the solid-state nanopore is about 5 to 6 years behind the biological nanopore.

The issues raised in the field of synthetic nanopore research are summarized as follows.

(i) Enhancing the blockade signal

(ii) Lowering the electrical noise

(iii) Thinning the sensing zone thickness

(iv) Controlling the translocation speed

(v) Alternative detection methods

(vi) Target biomolecules

The first and second issues are related to ensuring a sufficient signal to noise ratio (SNR). Sensing simple translocation of biomolecule required a sufficient SNR, but distinguishing the differences in the nucleotides in the DNA needs much higher SNR. Sensing zone is related to the spatial resolution, which is how many nucleotides are contained in the pore. Therefore, studies have been tried to reduce the thickness of the membrane. Controlling the velocity of DNA passage has been the biggest problem in the nanopore field. It means that translocation speed of DNA is too fast to measure the signal of the nucleotide one by one using the measuring equipment. In biological nanopores, the use of polymerase to retard the speed at which a single nucleotide is passed down to 1 ms has become a major breakthrough to DNA sequencing. Addressing the three issues, mentioned so far, including SNR, spatial resolution and temporal resolution, solid-state nanopores can go one step further toward DNA sequencing application. In this chapter, we will mainly describe these issues.

The remaining two issues are available only in solid-state nanopores. Through the integration with an additional architecture, a new measurement method has been studied such as tunneling currents[4] or optical sensing[5, 6],rather than an existing ion current measurement (figure 2-2). In addition to DNA sensing, solid-state nanopores have the advantage of sensing other biomolecules, especially proteins. Protein sensing is a unique part of the solid-state nanopore,

because the size of the protein, in general, can not pass through the biological nanopore. Up to date, single protein, protein-protein and DNA-protein analysis results are reported using solid-state nanopore sensor.[3, 7, 8]

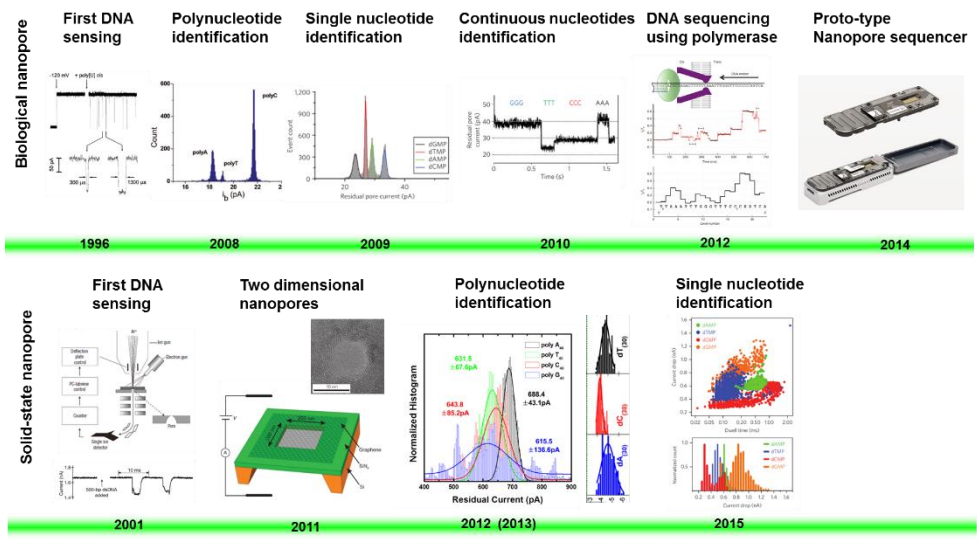

Figure 2-1. Historical timeline of major research achievements for DNA sequencing application in biological nanopore and solid-state nanopore.

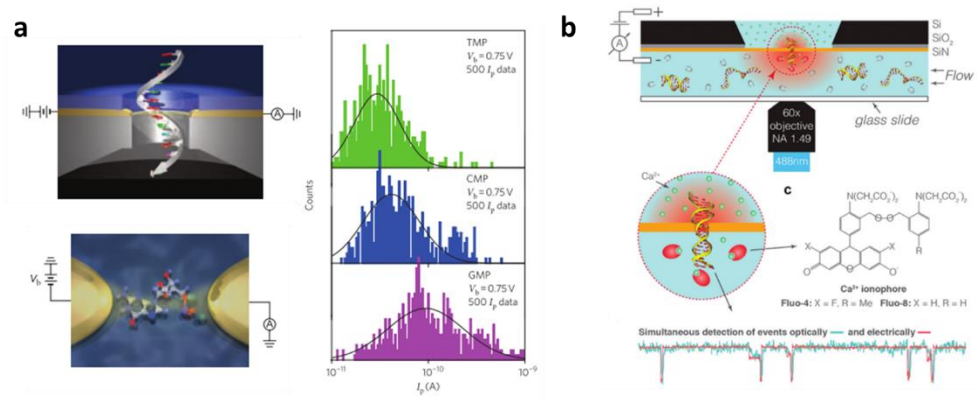

Figure 2-2. Alternative sensing methods in solid-state nanopore (a) A schematics of tunneling current measurement through the embedded gold nanogap. This device can demonstrate the discrimination of single nucleotides (TMP, CMP, GMP) (b) Optical sensing method in solid-state nanopore using Ca^{2+} ions and Ca^{2+} activated dye. It can operate simultaneous electrical and optical detection of DNA transports.

2.2. Reduction of electrical noise

2.2.1. Electrical current noise in nanopore system

As aforementioned in chapter 1, the nanopore device can detect the translocation of biomolecule by analyzing the mean amplitude of blockade current (ΔI) and the dwell time of biomolecules (t_d). However, the measurement of the biomolecules through ionic current measurement involves the electrical noise, so signal to noise ratio (SNR) becomes important factor of the device (figure 2-3a). SNR is defined as $SNR = \Delta I/I_{RMS}$, where I_{RMS} is the root-mean-quare (RMS) noise of DC currents.[9] In addition to the SNR of the typical biomolecule detection, the nanopore DNA sequencing needs higher SNR to discriminate each different nucleotide. Different nucleotides produce different residual currents, so the distinguishable SNR is defined as $SNR_{bp}= \Delta I_{bp}/I_{RMS,}$ where ΔI_{bp} is the difference between the current blockage of the different nucleotides in figure 2-3a.

Before introducing methods to reduce RMS noise, we will first explain how to analyze noise sources in the nanopore system. The power spectral density (PSD, S_I) curve of the measured current trace is used to analyze the noise characteristics of the nanopores (figure 2-2b). And the RMS noise (I_{RMS}) is estimated from the integration of the PSD with respect to the frequency up to the filter frequency. Typically, the PSD (S_I) is classified into four noise sources, which are the flicker noise ($S_{Flicker}$), thermal noise combined with shot noise ($S_{Thermal}$), dielectric noise ($S_{Dielectric}$) and amplifier noise (S_{Amp}). As expressed in equation 1, each noise source

has a specific frequency dependency, and the RMS noise (I_{RMS}) are expressed as the sum of four different noise sources in equation 2 :

$$S_I = S_{Flicker}(\propto 1/f) + S_{Ther}(\propto 1/R_P) + S_{Dielec}(\propto C_D D_D f) + S_{Amp}(\propto f^2) \quad (1)$$

$$\begin{aligned} I_{rms}{}^2 &= \int S_I df \\ &= I_{Flicker}{}^2(\propto \ln(f)) + I_{Ther}{}^2(\propto f/R_P) + I_{Dielec}{}^2(\propto C_D D_D f^2) + I_{Amp}{}^2(\propto f^3) \end{aligned} \quad (2)$$

where f is the frequency, R_P is the pore resistance and C_D and D_D are the capacitance and dielectric loss of the nanopore device.[10, 11]

Flicker noise or *1/f* noise is a noise source that is inversely proportional to the frequency and dominantly operates at low frequencies.[12, 13] Its noise power spectrum has the Hooge`s model expression in equation 3:

$$S_{Flicker}/I^2 = A_N/f^\beta = (\alpha/N_C)/f^\beta \quad (3)$$

where I is the ionic current of nanopore device, A_N is noise power, f is frequency, α is the Hooge parameter, N_C is the total number of charge carriers, and β is an fitting parameter that is commonly close to 1.[13] Hooge`s model suggest that flicker noise associated with fluctuations of the number of charge carrier or the mobility of charge carrier in bulk conductors, as well as in ionic current system.[14, 15] However, it is a subject still under debate which mechanism causes the charge fluctuation or mobility fluctuation.

Thermal noise is a frequency-independent noise source and has following relation in equation 4 for the nanopore device with resistance R (or conductance G):

$$S_{Ther} = 4kT / R = 4kTG \tag{4}$$

where, k, T, R, G is the Boltzman constant, temperature, resistance and conductance of nanopore, respectively. Thermal noise is less dominant than other noise sources because, for the common nanopore system, it is not easy to exceed 100 nS, where the nanopore device with 100 nS conductance has 1.6×10^{-3} $(\mathrm{pA}^2/\mathrm{Hz})$ and this level is typically lower than that of other noise sources.[11]

Aforementioned two noise sources, 1/f and thermal noise, are commonly considered as low frequency noise. On the contrast, dielectric noise is a main noise source in high frequency region (> 1 kHz) and is linearly proportional to the frequency. The noise source in this frequency range can be described as

$$S_{Dielec} = 4kTC_D D_D (2\pi f) \tag{5}$$

where k is Boltzmann's constant, T is the absolute temperature, and C_D and D_D are the chip capacitance and dielectric loss of the nanopore system.[10] Since the nanopore measurement system consists of electrochemical circuit, the entire nanopore device can be seen as a parallel-plate capacitor.[9, 11] From the viewpoint of the parallel-plate capacitor model, the substrate is responsible for many portion of the nanopore chip, which means C_D and D_D is largely determined by the substrate properties. In sum, the two noises described above are determined by the geometry

of the nanopore or the surface properties of the membrane, while the dielectric noise and the amplifier noise described below are significantly affected by the substrate properties.

The amplifier noise is proportional to the square of the frequency and can be described as

$$S_{Amp} \approx (2\pi f (C_D + C_W + C_A) v_n)^2 \quad (6)$$

, where C_D, C_W, C_A is the capacitance related to the nanopore device, the electrode wiring, the input of amplifier, respectively, and v_n is the input-referred voltage noise of the amplifier ($V/\sqrt{Hz}$).[16] As you can see from the above equation, the amplifier noise is also affected by the chip of the nanopore, but it mostly depends on the performance of the amplifier equipment itself. Amplifier noise was not a big concern in the past because this noise mainly acts at extremely high frequency (> 100 kHz) and the low pass filter works at 10 kHz or 100 kHz with a typical Axopatch 200B patch clamp system. However, with the demand for high bandwidth measurement, amplifiers capable of being measured with MHz bandwidth have been built, making the amplifier noise more important.

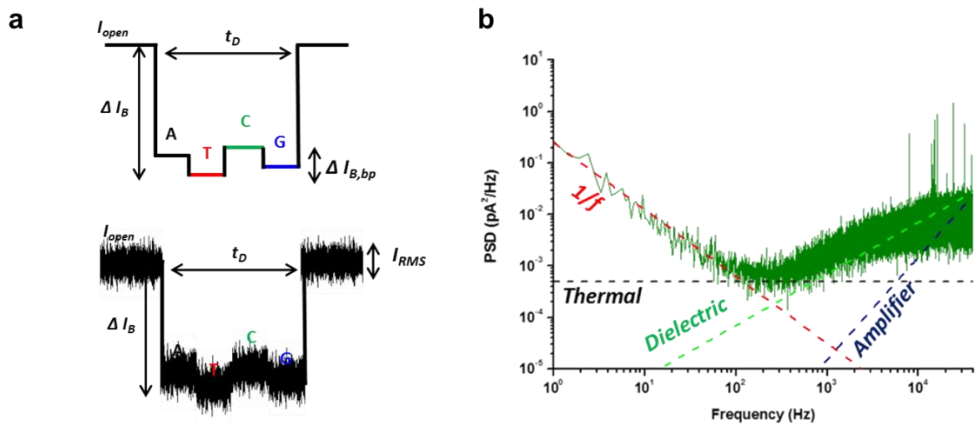

Figure 2-3. Blockade signal and electrical noise in nanopore system (a) Schematic example of DNA translocation.

2.2.2. Approaches for noise reduction

Studies to reduce the electrical noise in solid-state nanopores have been progressed on lowering the aforementioned noise sources except the thermal noise. As described above, in a typical nanopore measurement with a sub-10 nm pore size and 1 M potassium chloride (KCl) solution for example, the thermal noise generally has a much lower PSD level than that of other noise sources.

The power spectral density of the 1/f noise is given a good description according to Hooge`s relation, but the origin is not clearly revealed, even in electronic system. Some groups proposed that the low frequency noise in solid-state nanopores may be attributed to the surface state of inner nanopore wall, where there are several mechanisms such as inhomogeneous surface charge[17], nanobubble formation[18], carbon contaminations deposited on the e-beam radiated site during TEM drilling[19] or imperfect hydrophilicity of SiNx nanopore surface[20]. To suppress the generation of 1/f noise, ALD coating or surface modification method have been tried and the effect of decreasing 1/f noise has been obtained, but these methods have disadvantages in process complexity. As presented in figure 2-4a, Tabard-Cossa et.al. demonstrated the treatment of nanopore surface with piranha solution (H_2SO_4 : H_2O_2) is effective in reducing the flicker noise by about two orders of magnitude (~1/f pA^2/Hz) over the bare state (~100/f pA^2/Hz).[21] Currently, piranha solution treatments in solid state nanopores are used by many groups as part of the protocol.[16, 22]

The above-mentioned 1/f noise is related to the charateristics of commonly used SiN_x nanopores. Similarly, a two dimensional membrane nanopores such as graphene has a high flicker noise, which showed flicker noises about two orders of magnitude higher than SiN_x membranes.[23] The initial suggestion is that this excess 1/f noise of 2-D nanopores is the hydrophobicity of the 2-D materials or structural defects in the membrane, such as pinholes and domain boundaries. However, further studies revealed that fewer layers instead of a single layer or the small opening area (> Φ 100 nm) of the supporting layer for the 2-D membrane can be helpful to improve the noise properties in both graphene and boron nitride (BN) nanopores (figure 2-4b).[24-27] Indeed, BN nanopore treated with both few layers (6~8 layer) and small opening size reported the improvement of 1/f noise level comparable to that of SiNx devices.[28] It is interpreted that membrane fluctuation affects fluid or ion flow because a thin membrane with a large area serves as a diaphragm in the solution. These results suggest that the mechanical stability related to the membrane fluctuation in the 2-D material may be one of the major factors that influence the flicker noise.[27]

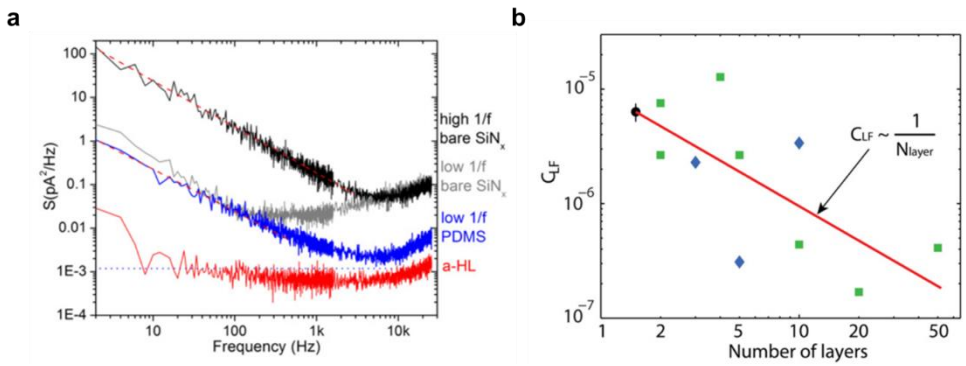

Figure 2-4. Flicker noise (1/f) noise in solid-state nanopore. (a) PSD curves for a-hemolysin, piranha treated and non-treated SiN_x nanopores. (b) 1/f noise power of graphene and h-BN nanopores with respect to the number of layers. Adopted from ref. 21 and ref. 27

The high frequency noise, including dielectric noise and amplifier noise, has a significant impact on the increase in RMS noise because it occupies a significant portion of the frequency domain. As expressed in equation 5 and 6, the elevated parasitic capacitance of nanopore chip generates both high frequency noises that prevents sampling at high bandwidths. To effectively reduce the chip capacitance, several methods have been adopted and can be categorized into four ways as follow; i) polymeric material sealing [11, 21, 29] ii) thick dielectric layer deposition underneath an active membrane [16, 22, 30] iii) alternative substrate based instead of Si [6, 31-33] iv) the utilization of Glass nanopipette [34, 35]. The reported dielectric noise and capacitance values for these methods are summarized in table 2-1. Indeed, while bare Si based nanopores reported a capacitance of approximately 300 pF[13], All these improved platforms have resulted in a significant reduction of the dielectric noise level to about one to two orders. For instance, our group developed a novel solid-state nanopore platform based on quartz substrate, not Si substrate (figure 2-5a).[32] As shown figure 2-5b, the nanopore fabricated directly on top of the quartz substrate displayed an extremely low noise level with a typical RMS value of 5 pA_{RMS} compared with that of the Si-based nanopore (40 pA_{RMS}). This phenomenon is clearly observed by the polynomial fit of the power spectrum as the dielectric noise level of the quartz-based nanopore ($5.2 \times 10^{-7} f$ (pA^2/Hz) is about two orders of magnitude lower than that of the silicon-based nanopore $1.5 \times$

$10^{-5}f$ (pA^2/Hz)).

Polymeric material, typically PDMS, is entirely coated, leaving only SiNx membrane area on the Si-based chip (figure 2-6). In addition, it has been reported that the dielectric noise has a lower value as the smaller area is left by using a photo-sensitive polyimide or a photo-definable PDMS capable of patterning a few um.[11, 29] As shown figure 2-6c, the reduction of RMS noise is determined by the dielectric property of the polymeric material and the coverage area.[29] Also, PDMS sealing method is often used in combination with a method of thick dielectric layer deposition such as Al_2O_3 or SiO_2 underneath an active membrane (figure 2-6d). In fact, many groups have used Si-based devices with PDMS coating method, on which few um-thick SiO_2 is deposited between a Si substrate and active membrane, and this device with few um-thick SiO_2 layer was reported to have approximately 50 pF capacitance. [16, 22, 36, 37]

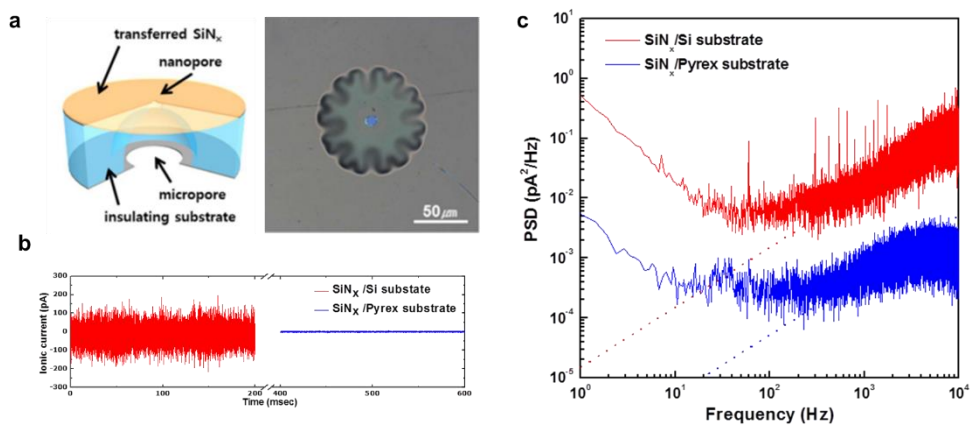

Figure 2-5. An example dielectric noise in solid-state nanopore. (a) Illustration of a quartz-based nanopore device. This device consists of a micrometer-sized pore in a quartz substrate and freestanding SiN_x membrane. (b) Comparison of raw current traces of Si and pyrex substrate based nanopore devices at 0 mV. (c) PSD curves corresponding to panel b. Adopted from ref. 32

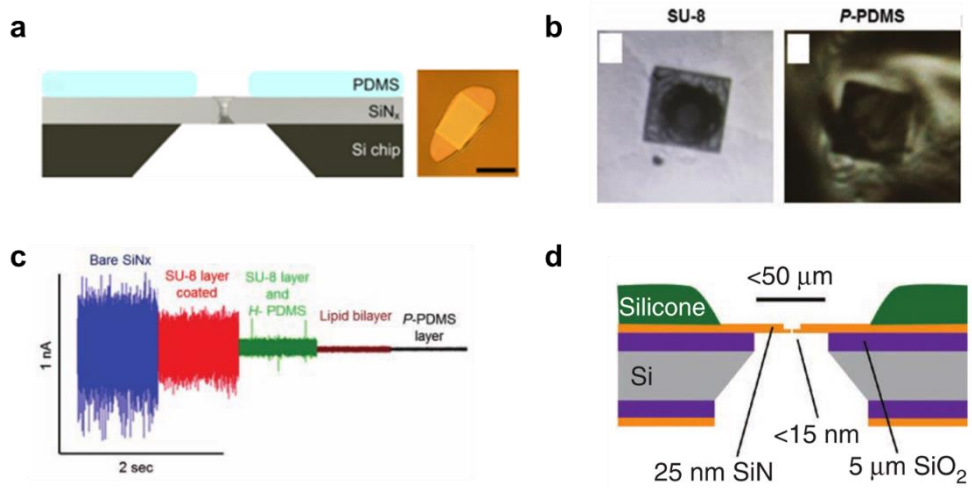

Figure 2-6. Dielectric reduction methods in solid-state nanopores (a) Schematic cross-sectional diagram of PDMS coated nanopore chip and its optical image. (b) Optical image of the nanopore chip coated with SU-8 and p-PDMS. (c) Raw current traces of nanopore devices coated with various polymeric layers. (d) Illustration of µm-thick SiO_2 inserted nanopore chip. Adopted from ref. 21, ref. 29 and ref. 16

Table 2-1. Summary of the dielectric noise level and its reduction methods in solid-state nanopores.

Reference	Platform	Dielectric noise level ($C \times f$ pA²/Hz)
Nanotechnology **18**, 305505, (2007)[21]	Bare Si/SiN_x	3.1×10^{-6} f
PNAS **105**, 417, (2008)[13]	Bare Si/SiN_x	5.3×10^{-5} f
Nanotechnology **18**, 305505, (2007)	α-HL	4.4×10^{-8} f
Nanotechnology **18**, 305505, (2007)	PDMS-covered	1.4×10^{-7} f
Nanotechnology **21**, 065502, (2010)[11]	Imide-covered	1.6×10^{-7} f
Journal of Nanoscience & Nanotechnology **15**, 5971, (2015)[29]	p-PDMS covered	9.6×10^{-8} f
ACS Nano **7**, 4629, (2013)[22]	2.5 μm thick SiO_2 inserting	1.1×10^{-7} f
Nano Lett **14**, 7215, (2014)[9]	Glass bonding	4.3×10^{-8} f
Nano Lett **16**, 4483, (2016)[38]	Glass bonding + CMOS amplifier	2.5×10^{-8} f
Anal Chem **85**, 3871, (2013)[31]	PDMS substrate	2.5×10^{-8} f
Scientific reports **4**, 7448, (2014)[32]	Quartz substrate	5.5×10^{-8} f
Nanoscale **8**, 5755, (2016)[28]	Pyrex substrate	3.0×10^{-8} f

However, since there is a relatively high dissipation loss between Si and electrolyte,[31] fabrication methods have been developed to replace it with a dielectric substrate other than a Si substrate. As mentioned abovem, figure 2-5a presents an illustration of fabricating well-defined solid-state nanopore on whole quartz substrate and optical microscope image of free-standing SiNx region on quartz.[32] To define a microfluidic channel through the quartz substrate, they used two step wet etch process using HF, so the membrane area of a-Si is opened as minimum 20um. And then, a SiNx layer of 5–20 nm thickness was transferred onto the top of this substrate and an aperture size of SiNx membrane was defined as 2 um. This process is meaningful to reduce the area of the membrane exposed to electrolyte solution to that defined by the width of the microfluidic channels, which decreases the chip capacitance.[9, 31] Similarly, such excellent dielectric property of glass substrate have also helped to ensure good dielectric noise in devices with glass-bonded Si substrate (figure 2-7-b).[9] Also, figure 2-7a exhibit a microfluidic-integrated nanopore device based on PDMS substrate and its optical image.[31] This device also used a SiNx membrane transfer method and has a minimum opening area of 6 μm^2 by adjusting the width of the microfluidic channel. As shown in table 2-1, all these devices based on dielectric substrates show a similar order level (~10^{-8} pA^2/Hz) of dielectric noise.

Unlike these substrate-based devices, figure 2-7c shows the use of a glass nanopipette as a solid-state nanopore. Thus, while conventional substrate-based

solid-state nanopores have a membrane structure, these glass nanopipettes have laser pulled glass nanocapillaries, which have a conical shape and a nm-sized orifice at their tip.[34, 39] However, the glass nanopipette has a problem of low signal to noise ratio (SNR) in order to detect DNA with a hole size of several tens of nanometers, although it guarantees low noise. To increase SNR, the newly developed technique was introduced by SEM-induced shrinking of diameter to 10 nm (figure 2-7c).[34] The shrinking glass nanopipettes showed simple dsDNA translocations and even characterization of DNA−protein complexes and protein–protein interactions.[40, 41]

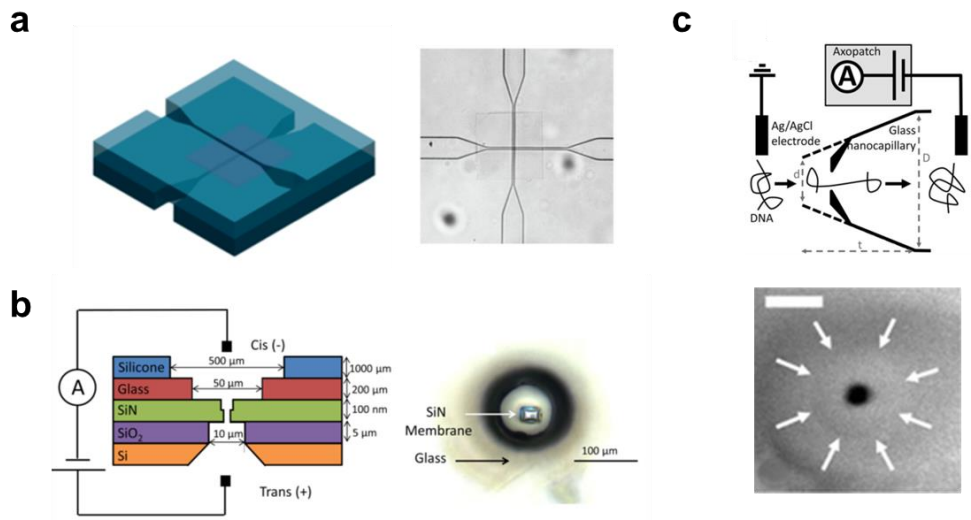

Figure 2-7. Dielectric reduction methods in solid-state nanopores by alternative substrates (a) Microfluidics-integrated nanopore device based on PDMS substrate (b) Shematic diagram and its optic image of glass-bonded nanopore device. (c) Measurement setup of glass nanocapillary and SEM image of electron-beam-induced shrinkage. Adopted from ref. 31, ref. 9 and ref. 34

Typically, the high frequency noise (>10 kHz) can be ignored by the application of digital or analog low-pass filters, but the importance for high bandwidth measurements has increased to avoid the distortion of blockade signal by temporal resolution. So, several efforts have focused on enhancing the bandwidth of measurement amplifiers, through custom-designed amplifiers such as CMOS-integrated amplifier[16, 42, 43] and Chimera instruments [9, 22], up to 1MHz.. Recently, a CMOS nanopore amplifier capable of temporal resolutions down to 100 ns (10 MHz bandwidth) has been developed.[38] In fact, when measuring with typical Axopatch 200B, which have a maximum bandwidth of 100 kHz, sufficient signal to noise ratio can be obtained using a device with a chip capacitance of 50 pF.[37] However, above 100 kHz bandwidth, the amplifier noise becomes a dominant noise source, and is affected by system capacitance, related to nanopore chip (C_D), wiring (C_W) and amplifier (C_A), and the input-referred voltage noise of the amplifier (v_n) according to the equation 6. As shown in figure 2-8 a, a standard chip with 43 pF exhibits approximately 400 pA_{RMS} larger noise value (558 pA_{RMS}) at 1 MHz bandwidth than (149 pA_{RMS}) that of a glass bonded nanopore chip with 5.8 pF.[9] Even, as can be seen from a difference of 30 pA_{RMS} between the device with 5.8 pF and 1.9 pF, it is important to reduce the chip capacitance to an extreme at high bandwidths above 1MHz. Based on this result, an improved two-step fabrication design with an insulating glass substrate was developed, resulting in sub-1 pF capacitance chips.[33]

As mentioned above, the high frequency noise is important for the capacitance of the nanopore device, but also depends on the performance of the amplifier including the amplifier capacitance (C_A) and the input-referred voltage noise of the amplifier (v_n). In figure 2-8b, CMOS-integrated amplifier have much lower high frequency noise than the ready-made amplifier Axopatch 200B, which is due to the value difference of C_A itself (CMOS-integrated C_A: ~2pF vs. Axopatch 200B C_A: 20pF).[16] Also, when measured with a 6 pF nanopore chip, the CMOS amplifiers showed RMS noise (I_{RMS} : 12.9 pA_{RMS}) about twice as low as the Axopatch (I_{RMS} : 21.8 pA_{RMS}) at 100 kHz bandwidth.[16] Recently, a CMOS-integrated nanopore amplifier with improved noise and bandwidth has also been developed, which can measure up to 10 MHz (100ns temporal resolution).[38] This most advanced CMOS amplifier has an open-headstage noise level of 8.1 pA_{RMS} at 200 kHz, 47.8 pA_{RMS} at 1MHz, and 481 pA_{RMS} at 5 MHz and 1.62 nA_{RMS} at the full 10 MHz measurement bandwidth.[38] Figure 2-8c shows the ionic current trace of 100 nt single-stranded DNA translocation events at 900 mV with 10 kHz, 200 kHz, 1 MHz and 5 MHz and figure 2-8d displays corresponding scatter plots of mean blockade current and dwell time. As the low-pass filtering frequency decreases, the attenuation of blockade signals for fast translocations increased, which means some events fail to get detected at lower bandwidths. In other words, there is a trade-off between improving temporal resolution and reducing

RMS noise and it is important to choose appropriate bandwidth for high SNR detection.[23]

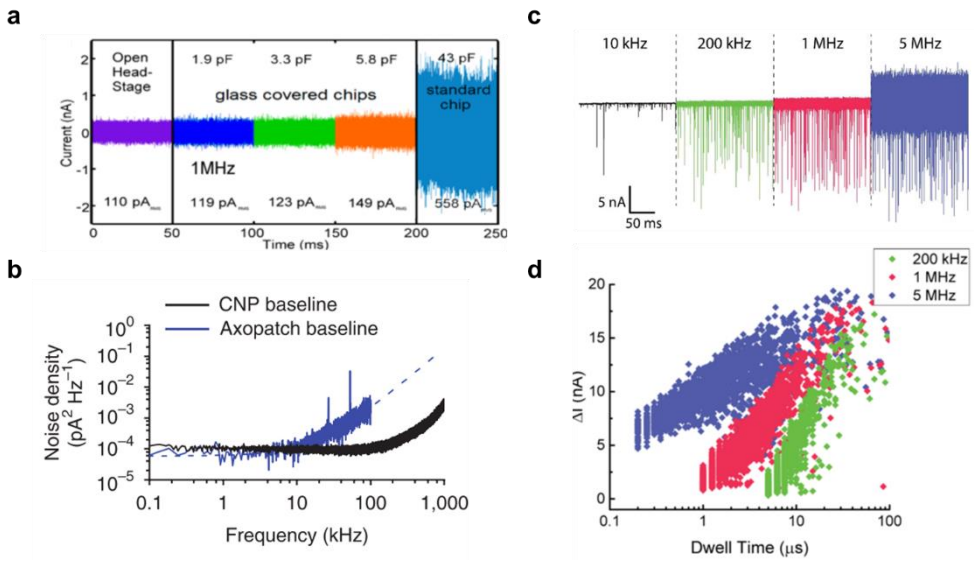

Figure 2-8. Amplifier noise of solid-state nanopores in high frequency region. (a) Ionic current traces for glass-bonded nanopore devices and standard Si-based device with various chip capacitances at 1 MHz bandwidth and 0 mV. (b) Power spectrum density plots for CMOS-based amplifier and an Axopatch 200B in whole-cell mode (c) Raw current traces of 100 nt ssDNA translocations at 900 mV bias as an application of 10 kHz, 200 kHz, 1MHz and 5 MHz filters. (d) Scatter plots for blockade current and dwell time corresponding to panel c. Adopted from ref. 9, ref. 16 and ref. 38

2.3. Improving signal and spatial resolution

2.3.1. Thin membrane materials

To ensure SNR for DNA sequencing through the nanopore, a large portion of nanopore research has been dedicated to enhancing the ionic current signal of DNA translocation, as well as reducing noise properties of nanopore device mentioned in previous section. In the condition of high electrolyte concentration (>0.1 M), the ionic current I_0 and the blockade current ΔI are determined by the pore diameter d and the membrane thickness L , as expressed in equation 7 and equation 8.

$$I_0 = \sigma V \left(\frac{4L}{\pi d^2} + \frac{1}{d}\right)^{-1} \tag{7}$$

$$\Delta I = I_0 - \sigma V \left(\frac{4L}{\pi {d_{eff}}^2} + \frac{1}{d_{eff}}\right)^{-1} \cong \sigma V \left(\frac{4L}{\pi {d_{DNA}}^2} + \frac{1}{d_{DNA}}\right)^{-1} \tag{8}$$

where, V is the applied voltage, σ is the conductivity of electrolyte solution, d_{DNA} is the DNA diameter (d_{DNA} = 2.2 nm for double-stranded DNA and d_{DNA} = 1.1 nm for single stranded DNA) and the effective pore diameter blocked by DNA in the pore, given by $d_{eff} = \sqrt{d^2 - {d_{DNA}}^2}$.[44] According to the above formula, the blockade current can be increased in three ways: high mol concentration [45, 46], small pore size[44, 47], and thin membrane thickness[32, 48].

Among them, various processes have focused on thinning membrane thickness because there is room for improvement in controlling the thickness according to the fabrication process. For instance, figure 2-9a displays ionic current traces and corresponding scatter plots of 40nt ssDNA for a 2 nm diamether nanopore in SiNx membrane with thickness variation.[32] As consistent with equation 7 and 8, both the baseline current and the amplitude of DNA blockade increase as the membrane thickness is decreased. Also, thinning the membrane is important for the vertical resolution, as well as for the increase of the signal. Assuming common translocation experiment in SiN_x membrane with 20 nm thickness, approximately 50 base pairs stay inside the pore at any given time. Therefore, many studies have been performed to obtain a membrane thickness of sub-10 nm.

Figure 2-10 summarizes the various fabrication methods of nanopore devices to thin the membrane thickness. Figure 2-10a is the membrane thinning process of common SiNx membrane using e-beam lithography to sub-10 nm thickness.[48] As shown in AFM image of figure 2-10a, e-beam lithography defined the etch area at the sub-um level and the thickness was controlled by the etch time of the SF_6 gas. Since the entire size of the SiN_x membrane made with KOH is more than 10 μm, if total area of the membrane is etched without e-beam lithography, the mechanical stability of the membrane can not be secured. The resulting nanopore devices have a minimum thickness of 5 nm, which is

comparable to the thickness of lipid bilayers.[22] In addition, a method for transferring membrane to a quartz substrate has been demonstrated to fabricate SiN_x membrane of 5 nm thickness.[32]

For a further reduction of thickness to less than 5 nm, the new fabrication process has been proposed using a sacrificial layer of poly-Si or SiO_2.[49] This device is fabricated by using SiN_x as a strong etch mask of KOH aqueous solution. As seen in figure 2-10b, even 3 nm thick SiNx layer was deposited in this process and survived during the two etch processes of Si substrate and poly Si layer. The active SiN_x layer has an opening size of approximately 500 nm through e-beam lithography and isotropic wet etching to obtain the robustness of the membrane. The thinnest effective thickness was found to be 0.6 nm and is comparable to the thickness of single layered graphene nanopore. In addition, the devices are used in combination with poring method through dielectric breakdown, resulting in reproducible nanopores with sub 2 nm diameter.[50]

Figure 2-10c depicts the electron-irradiation-based thinning method of Si-based films using a scanning transmission electron microscope (STEM).[51] Here, the thinning area was about $63 \times 63\ nm^2$ and current density of a scanning probe was $4.8 \times 10^9\ \mathrm{A/m^2}$, where the atomic ratio N/Si was below 0.1 and the resulting membrane was referred to amorphous-Si membrane with sub 2 nm thickness. Also, they demonstrated the theoretical thickness limitation of a-Si

membranes, which was established to be ~1 nm with MD simulations, and the high blockade conductance (ΔG ~ 10 nS) and SNR (~70 at 100 kHz) for dsDNA.

Besides thinning SiN_x fims, various efforts have been made to apply new materials as alternative membranes with high vertical resolution. Representatively, atomic layer deposition (ALD) of Al_2O_3[52, 53] or HfO_2[36, 37, 54] was introduced. Basically, the ALD oxide films were deposited on the SiN_x membrane and remained in the form of membrane through the process of selective etching the SiN_x (figure 2-10d). In fact, Al_2O_3 nanopores were reported to be about 50 nm thick, but HfO_2 nanopores were reported to have a minimum 3 nm thickness. Remarkably, HfO_2 nanopores exhibit better long-term stability than that of SiN_x pores with similar thickness during continuous measurements with DNA translocation signals.[37, 49] Also, HfO_2 inner wall was found to interact with phosphate group of DNA backbone, which induced slow transports of both dsDNA and ssDNA.

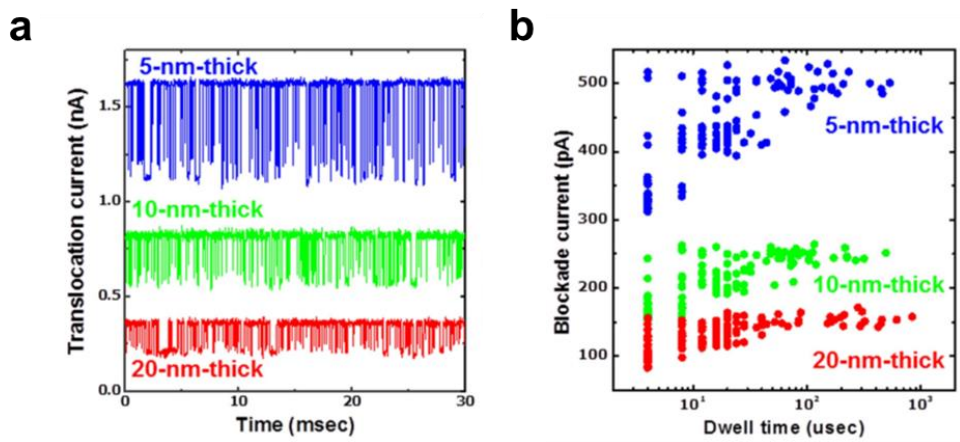

Figure 2-9. Membrane thickness effect on blockade current. (a) Ionic current traces for DNA translocation of 40 nt ssDNA through nanopore with different SiN_x membrane of 20, 10 and 5 nm thickness. (b) Corresponding scatter plots of blockade current and dwell time to panel a. Adopted from ref. 32

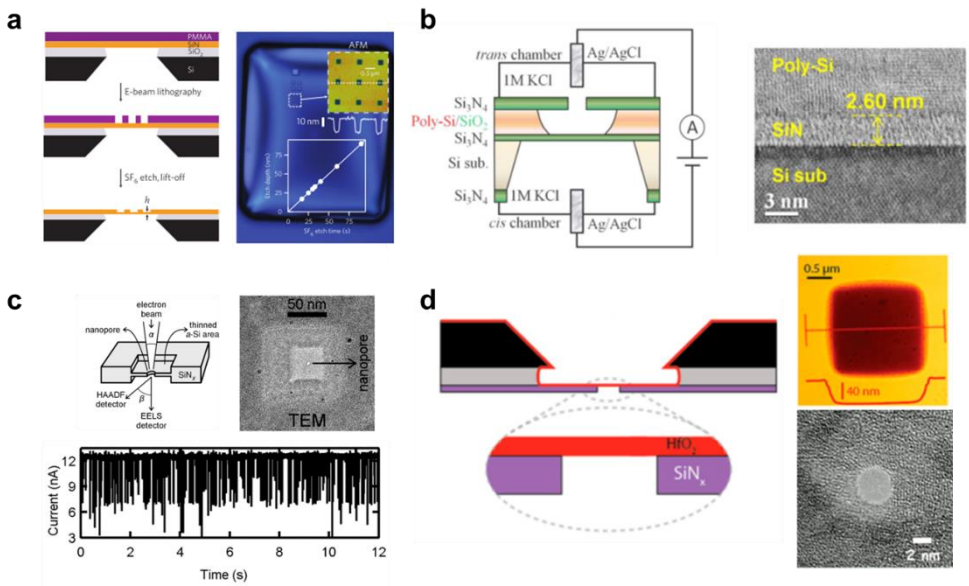

Figure 2-10. Fabrication advances for thin membrane nanopores (a) Thinning process of SiN_x membrane involving e-beam lithography and dry etching process. (b) Sub 3nm-thick SiNx membrane using the poly-Si sacrificial layer process. Right image is cross-sectional STEM image for sub 3 nm-thick SiNx layer. (c) Membrane thinning process based on electron-irradiation and TEM micrograph of an a-Si thinned area with nanopore. The bottom image is the ionic current trace of dsDNA translocation through Φ 4.6 nm nanopore in thinned a-Si membrane. (d) Fabrication of 3 -8 nm thick ALD HfO_2 nanopore. AFM topography shows a freestanding HfO_2 region and TEM image shows Φ 3 nm HfO_2. nanopore. Adopted from ref. 48 , ref. 50, ref. 51 and ref. 37

2.3.2. Two dimensional materials

Two dimensional (2-D) materials, especially graphene, has attracted a lot of interests in nanopore systems as the thinnest possible materials with thickness comparable to the gap between the base pairs of DNA (0.3 ~ 0.5 nm).[55, 56] Three individual groups reported the demonstration of dsDNA translocation through graphene nanopores around the same time in 2010 (figure 2-11a).[23, 57, 58] As expected, graphene nanopores exhibited larger value of blockade currents compared with conventional silicon nitride pores due to its thin membrane (figure 2-11b).[24, 57] However, graphene nanopores were reported to have high 1/f noise at low frequency and the mechanical stability of 2-D membranes may be suspected to be the origin of high noise.[25, 27] The 1/f noise of graphene nanopores was effectively reduced by ALD oxide coating on graphene membrane[23, 59], the small opening area of supporting layer[24] and using fewer layered graphene[25, 27], where all of these methods may be related to the improvement of the mechanical stability. Another issue is the clogging problem of pores during ssDNA translocation, which results from the attractive hydrophobic π–π stacking interactions between the nucleobases and graphene and can be prevented by hydrophilic coating[60] and measurement in high mol concentration and high pH[24].

With a similar concept, other 2-D materials have been explored to make atomically thin nanopores. In figure 2-11c, Liu et.al. has firstly introduced boron nitride (BN) material into the nanopore devices and demonstrated the

enhancement of DNA signal compared with the similar sized SiN_x nanopores.[61] The merit of BN is that it isn`t damaged by the UV-ozone or O_2 plasma treatment for enhancing hydrophilicity unlike graphene, which is advantageous in wetting property and inhibiting the DNA clogging.[26] As with graphene nanopores, high 1/f noise was an issue in BN nanopores. Chapter 3 represented a good improvement of both flicker and dielectric noise, which resulted in dsDNA translocations with high SNR around 50 at 100 kHz bandwidth (figure 2-11d).[28]

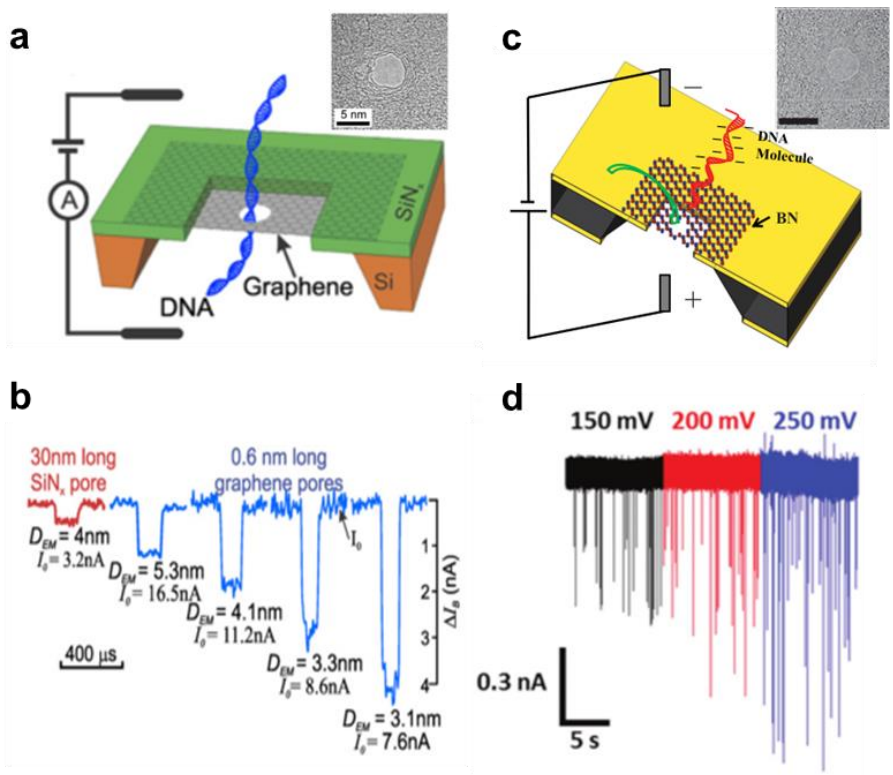

Figure 2-11. Two dimensional membrane nanopores using graphene and boron nitride (a) Schematic diagram of nanopore device using a suspended graphene material. (b) Representative event traces of dsDNA through graphene nanopores with different diameters, compared to SiN_x device. (c) Measurement scheme of nanopore device using a suspend BN membrane. (d) Raw current traces of 1 kbp dsDNA transport, filtered at 100 kHz, through multilayered BN nanopore with low noise substrate. Adopted from ref. 24, ref. 57, ref. 61 and ref. 28

Recently, metal sulfides such as molybdenum disulfide (MoS_2)[62-66] and tungsten disulfides (WS_2)[67, 68] is a newly emerging material as alternatives of two dimensional materials. In figure 2-12a, nanopore device in atomically thin MoS_2 membrane demonstrated the translocations for various types of dsDNA with different lengths and conformations, showing improved sensitivity (SNR > 10) compared to the conventional SiNx nanopores with tens of nanometers thickness.[62] As shown in figure 2-11b, MoS_2 nanopores can be made by the new nanopore engineering on single layer MoS_2 with in-situ electrochemical reaction (ECR), which starts for a certain critical voltage bias (~0.8 V) at a defect/vacancy present in the MoS_2 membrane.[63] In particular, *Feng et al.* achieved the identification of single-stranded DNA homopolymers (poly A_{30}, T_{30}, C_{30}, G_{30}) and even single nucleotides using MoS_2 nanopores (figure 2-11c).[64] Small sized MoS_2 nanopores (~2 nm) was integrated with a viscosity gradient system based on room temperature ionic liquids for retarding DNA translocation speed. This system was effective enough to detect single nucleotides measured even at 10 kHz filter.

One of the long-standing problems of 2D nanopores is the difficulty of wafer-scale process because it involves the membrane transfer process during the fabrication of 2D nanopores. Also, transfer protocol may cause the yield of the device to deteriorate by inducing pinholes, cracks, and contamination during the transfer process. In graphene nanopores, a novel approach has been reported

to fabricate in-situ, large arrays of few-layer freestanding pinhole-free graphene membranes.[69] In MoS_2 nanopores, similar approach has been proposed to grow free-standing high quality MoS_2 membranes directly on um-sized aperture in SiNx (figure 2-11d).[66] Since growth of MoS_2 requires no catalyst, there is no need to deposit the catalyst and remove it separately like graphene process. In addition to applications in nanopore analysis, there is a lot of attraction in such directly grown 2-D membrane process for ion filtration and other membrane applications.

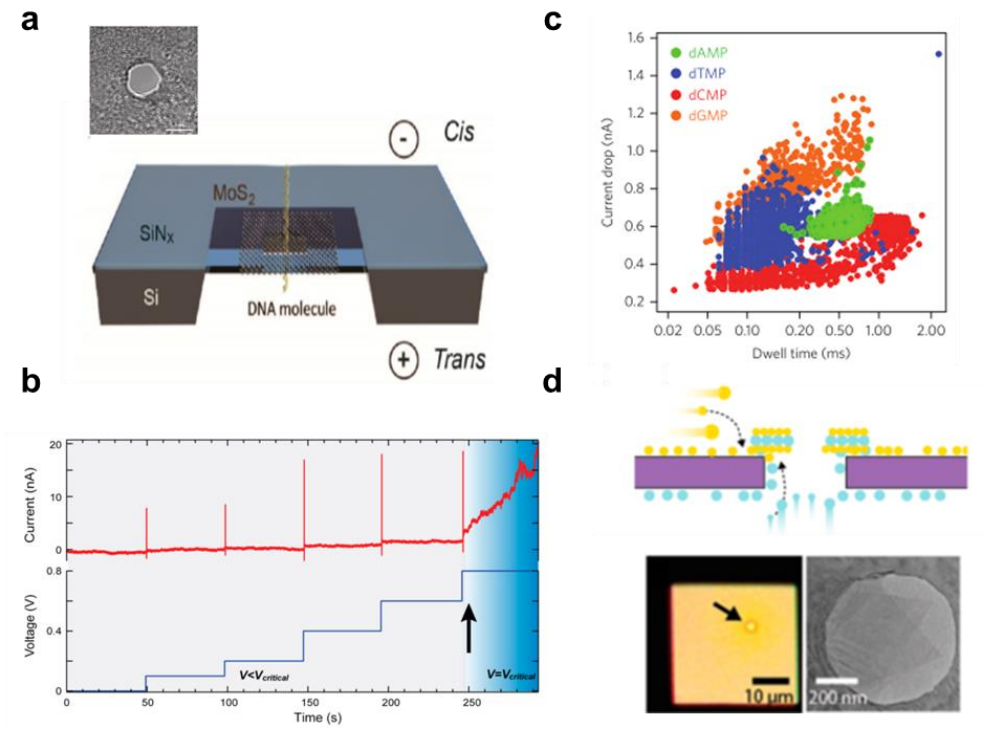

Figure 2-12. Two dimensional membrane nanopores using moly disulfide (MoS_2) materials (a) Nanopore device of a MoS_2 membrane and TEM image of a nanopore in MoS_2 membrane. (b) Ionic current and voltage trace for nanopore creation in MoS_2 membrane by electrochemical reaction. (c) Scatter plots of single nucleotide translocation events through single layered MoS2 pore using RTILs/KCl viscosity gradient system for retarding translocation speed. (d) Direct growth method for MoS_2 membrane on SiN_x window. Optical and TEM images show MoS_2 membrane on a ~ 1 μm circular window of a SiNx film. Adopted from ref. 62, ref. 63, ref. 64 and ref. 66

Reference

1. Miten Jain, et al., Improved data analysis for the MinION nanopore sequencer. *Nature Methods*, 2015. **12**(4): 351-356.
2. M. Wanunu, Nanopores: A journey towards DNA sequencing. *Phys Life Rev*, 2012. **9**(2): 125-58.
3. W. Shi, et al., Nanopore Sensing. *Anal Chem*, 2017. **89**(1): 157-188.
4. Makusu Tsutsui, et al., Identifying single nucleotides by tunnelling current. *Nat Nano*, 2010. **5**(4): 286-290.
5. T. Gilboa and A. Meller, Optical sensing and analyte manipulation in solid-state nanopores. *Analyst*, 2015. **140**(14): 4733-47.
6. William H. Pitchford, et al., Synchronized Optical and Electronic Detection of Biomolecules Using a Low Noise Nanopore Platform. *ACS Nano*, 2015. **9**(2): 1740-1748.
7. A. H. Squires, et al., Single-Molecule Characterization of DNA–Protein Interactions Using Nanopore Biosensors. 2016.
8. A. Oukhaled, et al., Sensing proteins through nanopores: fundamental to applications. *ACS Chem Biol*, 2012. **7**(12): 1935-49.
9. A. Balan, et al., Improving Signal-to-Noise Performance for DNA Translocation in Solid-State Nanopores at MHz Bandwidths. *Nano Lett*, 2014. **14**(12): 7215-20.
10. Jeffrey D. Uram, et al., Noise and Bandwidth of Current Recordings from Submicrometer Pores and Nanopores. *ACS Nano*, 2008. **2**(5): 857-872.
11. V. Dimitrov, et al., Nanopores in solid-state membranes engineered for single molecule detection. *Nanotechnology*, 2010. **21**(6): 065502.

12. R. M. Smeets, et al., Low-frequency noise in solid-state nanopores. *Nanotechnology*, 2009. **20**(9): 095501.

13. R. M. M. Smeets, et al., Noise in solid-state nanopores. *Proceedings of the National Academy of Sciences of the United States of America*, 2008. **105**(2): 417-421.

14. F. N. Hooge, 1f noise in the conductance of ions in aqueous solutions. *Physics Letters A*, 1970. **33**(3): 169-170.

15. F. N. Hooge, 1/f noise sources. *IEEE Transactions on Electron Devices*, 1994. **41**(11): 1926-1935.

16. J. K. Rosenstein, et al., Integrated nanopore sensing platform with sub-microsecond temporal resolution. *Nat Methods*, 2012. **9**(5): 487-92.

17. D. P. Hoogerheide, et al., Probing Surface Charge Fluctuations with Solid-State Nanopores. *Physical Review Letters*, 2009. **102**(25).

18. R. M. M. Smeets, et al., Nanobubbles in Solid-State Nanopores. *Physical Review Letters*, 2006. **97**(8).

19. Aleksandra Radenovic, et al., Fabrication of 10 nm diameter hydrocarbon nanopores. *Applied Physics Letters*, 2008. **93**(18): 183101.

20. E. Beamish, et al., Precise control of the size and noise of solid-state nanopores using high electric fields. *Nanotechnology*, 2012. **23**(40): 405301.

21. Vincent Tabard-Cossa, et al., Noise analysis and reduction in solid-state nanopores. *Nanotechnology*, 2007. **18**(30): 305505.

22. Kimberly Venta, et al., Differentiation of Short, Single-Stranded DNA Homopolymers in Solid-State Nanopores. *ACS Nano*, 2013. **7**(5): 4629-4636.

23. C. A. Merchant, et al., DNA translocation through graphene nanopores. *Nano Lett*, 2010. **10**(8): 2915-21.

24. S. Garaj, et al., Molecule-hugging graphene nanopores. *Proc Natl Acad Sci U S A*, 2013. **110**(30): 12192-6.

25. A. Kumar, et al., Noise and its reduction in graphene based nanopore devices. *Nanotechnology*, 2013. **24**(49): 495503.

26. Z. Zhou, et al., DNA Translocation through Hydrophilic Nanopore in Hexagonal Boron Nitride. *Sci Rep*, 2013. **3**: 3287.

27. S. J. Heerema, et al., 1/f noise in graphene nanopores. *Nanotechnology*, 2015. **26**(7): 074001.

28. Kyeong-Beom Park, et al., Noise and sensitivity characteristics of solid-state nanopores with a boron nitride 2-D membrane on a pyrex substrate. *Nanoscale*, 2016. **8**(10): 5755-5763.

29. Min-Cheol Lim, et al., A Mask-Free Passivation Process for Low Noise Nanopore Devices. *Journal of Nanoscience and Nanotechnology*, 2015. **15**(8): 5971-5977.

30. Min-Hyun Lee, et al., Leakage current in a Si-based nanopore structure and its influence on noise characteristics. *Microfluidics and Nanofluidics*, 2013. **16**(1-2): 123-130.

31. T. Jain, et al., Integration of solid-state nanopores in microfluidic networks via transfer printing of suspended membranes. *Anal Chem*, 2013. **85**(8): 3871-8.

32. Min-Hyun Lee, et al., A Low-Noise Solid-State Nanopore Platform Based on a Highly Insulating Substrate. *Scientific Reports*, 2014. **4**: 7448.

33. A. Balan, et al., Suspended Solid-state Membranes on Glass Chips with

Sub 1-pF Capacitance for Biomolecule Sensing Applications. *Sci Rep*, 2015. **5**: 17775.

34. Lorenz J. Steinbock, et al., DNA Translocation through Low-Noise Glass Nanopores. *ACS Nano*, 2013. **7**(12): 11255-11262.
35. Wenhong Li, et al., Single Protein Molecule Detection by Glass Nanopores. *ACS Nano*, 2013. **7**(5): 4129-4134.
36. J. Larkin, et al., High-bandwidth protein analysis using solid-state nanopores. *Biophys J*, 2014. **106**(3): 696-704.
37. J. Larkin, et al., Slow DNA transport through nanopores in hafnium oxide membranes. *ACS Nano*, 2013. **7**(11): 10121-8.
38. S. Shekar, et al., Measurement of DNA Translocation Dynamics in a Solid-State Nanopore at 100 ns Temporal Resolution. *Nano Lett*, 2016. **16**(7): 4483-9.
39. J. A. Bafna and G. V. Soni, Fabrication of Low Noise Borosilicate Glass Nanopores for Single Molecule Sensing. *PLoS One*, 2016. **11**(6): e0157399.
40. Roman D. Bulushev, et al., Single Molecule Localization and Discrimination of DNA–Protein Complexes by Controlled Translocation Through Nanocapillaries. *Nano Letters*, 2016.
41. Purushottam Babu Tiwari, et al., Quantitative study of protein-protein interactions by quartz nanopipettes. *Nanoscale*, 2014. **6**(17): 10255-10263.
42. Raquel L. Fraccari, et al., High-bandwidth detection of short DNA in nanopipettes. *Faraday Discussions*, 2016. **193**(0): 459-470.
43. P. Nuttall, et al., Single-Molecule Studies of Unlabeled Full-Length p53

Protein Binding to DNA. *J Phys Chem B*, 2016. **120**(9): 2106-14.

44. Stefan W. Kowalczyk, et al., Modeling the conductance and DNA blockade of solid-state nanopores. *Nanotechnology*, 2011. **22**(31): 315101.

45. S. W. Kowalczyk, et al., Slowing down DNA translocation through a nanopore in lithium chloride. *Nano Lett*, 2012. **12**(2): 1038-44.

46. D. Fologea, et al., Slowing DNA translocation in a solid-state nanopore. *Nano Letters*, 2005. **5**(9): 1734-1737.

47. M. J Kim, et al., Rapid Fabrication of Uniformly Sized Nanopores and Nanopore Arrays for Parallel DNA Analysis. *Advanced Materials*, 2006. **18**(23): 3149-3153.

48. Meni Wanunu, et al., Rapid electronic detection of probe-specific microRNAs using thin nanopore sensors. *Nat Nano*, 2010. **5**(11): 807-814.

49. Itaru Yanagi, et al., Fabrication of 3-nm-thick Si3N4 membranes for solid-state nanopores using the poly-Si sacrificial layer process. *Scientific Reports*, 2015. **5**: 14656.

50. Itaru Yanagi, et al., Thickness-dependent dielectric breakdown and nanopore creation on sub-10-nm-thick SiN membranes in solution. *Journal of Applied Physics*, 2017. **121**(4): 045301.

51. Julio A. Rodríguez-Manzo, et al., DNA Translocation in Nanometer Thick Silicon Nanopores. *ACS Nano*, 2015. **9**(6): 6555-6564.

52. B. M. Venkatesan, et al., Highly Sensitive, Mechanically Stable Nanopore Sensors for DNA Analysis. *Advanced Materials*, 2009. **21**(27): 2771-+.

53. Bala Murali Venkatesan, et al., DNA Sensing Using Nanocrystalline

Surface-Enhanced Al2O3Nanopore Sensors. *Advanced Functional Materials*, 2010. **20**(8): 1266-1275.

54. J. Shim, et al., Electron beam induced local crystallization of HfO2 nanopores for biosensing applications. *Nanoscale*, 2013. **5**(22): 10887-93.

55. Stephanie J. Heerema and Cees Dekker, Graphene nanodevices for DNA sequencing. *Nat Nano*, 2016. **11**(2): 127-136.

56. Hadi Arjmandi-Tash, et al., Single molecule detection with graphene and other two-dimensional materials: nanopores and beyond. *Chemical Society Reviews*, 2016. **45**(3): 476-493.

57. S. Garaj, et al., Graphene as a subnanometre trans-electrode membrane. *Nature*, 2010. **467**(7312): 190-3.

58. G. F. Schneider, et al., DNA Translocation through Graphene Nanopores. *Nano Letters*, 2010. **10**(8): 3163-3167.

59. Bala Murali Venkatesan, et al., Stacked Graphene-Al2O3 Nanopore Sensors for Sensitive Detection of DNA and DNA–Protein Complexes. *ACS Nano*, 2011. **6**(1): 441-450.

60. G. F. Schneider, et al., Tailoring the hydrophobicity of graphene for its use as nanopores for DNA translocation. *Nat Commun*, 2013. **4**: 2619.

61. S. Liu, et al., Boron Nitride Nanopores: Highly Sensitive DNA Single-Molecule Detectors. *Adv. Mater*, 2013. **25**: 4549-4554.

62. Ke Liu, et al., Atomically Thin Molybdenum Disulfide Nanopores with High Sensitivity for DNA Translocation. *ACS Nano*, 2014. **8**(3): 2504-2511.

63. J. Feng, et al., Electrochemical Reaction in Single Layer MoS2:

Nanopores Opened Atom by Atom. *Nano Letters*, 2015. **15**(5): 3431-3438.

64. Jiandong Feng, et al., Identification of single nucleotides in MoS2 nanopores. *Nat Nano*, 2015. **10**(12): 1070-1076.

65. J. Feng, et al., Single-layer MoS2 nanopores as nanopower generators. *Nature*, 2016.

66. P. Waduge, et al., Direct and Scalable Deposition of Atomically Thin Low-Noise MoS2 Membranes on Apertures. *ACS Nano*, 2015. **9**(7): 7352-9.

67. Anderson G. Vieira, et al., Temperature- and power-dependent phonon properties of suspended continuous WS2 monolayer films. *Vibrational Spectroscopy*, 2016. **86**: 270-276.

68. G. Danda, et al., Monolayer WS2 Nanopores for DNA Translocation with Light-Adjustable Sizes. *ACS Nano*, 2017.

69. Pradeep Waduge, et al., Programmed Synthesis of Freestanding Graphene Nanomembrane Arrays. *Small*, 2015. **11**(5): 597-603.

Chapter 3.

Noise and sensitivity characteristics of solid-state nanopores with a boron nitride 2-D membrane on a pyrex substrate

This chapter is based the paper published in

Nanoscale, **8** (10), 5755 (2016).

3.1. Introduction

Considerable progress has been made recently with biological nanopores for a single nucleotide identification[1] and plausible DNA sequencing[2-4]. This progress has resulted from the advantages inherent to biological nanopores, such as (a) reproducible formations of extremely small pore sizes (less than 1.5 nm), (b) extremely small thickness sensing zones (approximately 1 nm or less depending on protein utilized), (c) excellent low noise levels of the protein nanopore with less than 10 pA I_{RMS}, (d) controlling the DNA translocation speed using enzymes, and (e) relatively small interactions between the DNA and protein pore wall (infrequent sticking or clogging of DNA to the pore wall). On the contrary, the progress in solid-state nanopores has been much slower due to the lack of such advantages of protein nanopores. Still, solid-state nanopores are still an attractive alternative because of their long term stability and versatility. Solid-state nanopores can be operated in harsh environments, be produced in a scalable manner, and can be engineered to act as an active device by itself or integrated with other sensing mechanisms.[5-7]

The basic structure of solid-state nanopores and their operating mechanism are almost the same as those of biological nanopores. A thin membrane with a nanometer scale pore provides a structure to sense biomolecules on a single molecule level by electrically trapping and translocating them through the pore.[5]

Here, the structure is utilized as a resistive pulse sensor to monitor the transient reduction of the pore conductance and time of reduction when the analyte biomolecules are electrophoretically driven through the pore. Up until now, a wide range of analytes have been studied with solid-state nanopores, most commonly single- and double-stranded DNA, RNA, and proteins, as well as the interaction between these molecules.[6, 8-18] Still, various hindrances remain to successful application of solid-state nanopores for biomolecule detection in general and, in particular, for DNA sequencing. These issues include (a) controlling the translocation speed of the biomolecule, (b) improving the trapping probability, and (c) enhancing both the spatial (lateral and vertical) and temporal resolution of the device.

In particular, the application of atomically thin two-dimensional materials such as graphene[19-22], boron nitride (BN) [23, 24] as well as recently developed transition metal-chalcogenide of MoS_2[25-27] as a membrane is an attractive method to improve the vertical resolution of these devices. For instance, to sequence DNA using solid-state nanopores, the vertical resolution of the device, namely, the thickness of membrane, should be less than 0.5 nm for a single base-pair resolution. Because the thickness of a single layer of graphene, BN, and MoS_2 are approximately 0.3-0.7 nm, these are the ideal membrane materials for highly sensitive solid-state nanopore devices. Moreover, thinner membranes are

expected to enhance the blockade signal to enhance the signal-to-noise ratio (SNR), assuming that the noise level is the same.[10, 17] However, the initial attempts of fabricating 2-D membrane nanopores using graphene were not satisfactory due to the high flicker noise that resulted.[19-21] High flicker noise has also been obtained from other 2-D membrane materials such as BN and MoS_2[23, 26, 26], which showed flicker noises about two orders of magnitude higher than SiN_x membranes. Initially, the hydrophobic nature of the 2-D membrane material and structural defects in the membrane, such as pinholes and domain boundaries, were suggested as the source of this high flicker noise.[20] However, recent reports by Kumar *et al.*[28] and Heerema *et al.*[29] reveal that the flicker noise level can be greatly reduced using fewer graphene layers instead of a single layer, which suggests that the mechanical stability of the membrane might be the major source of the flicker noise. Similarly, other researchers found out that decreasing the opening area of the supporting layer for the 2-D membrane effectively reduces the flicker noise in both graphene[22] and BN[24]. All of these results suggest that the mechanical stability of the membrane material is indeed one of the major factors that influence the flicker noise.

In this chapter, we would like to present the fabrication scheme of a highly sensitive, low noise solid-state nanopore device using a hexagonal-BN (h-BN) membrane. Hexagonal-BN layers are insulators with a wide band gap (~5.9 eV),

unlike the graphene which is a conductor.[30] Additionally, h-BN nanopores are highly resistant to oxidation and turned to hydrophilic by UV-oxygen treatments.[24] Both of these attributes are important considerations in the search for solid-state nanopore membrane materials. First of all, h-BN membranes were transferred on two different substrate materials, Si and pyrex substrate, to compare the dielectric noise. Previously, we reported that the dielectric noise of the solid-state nanopore can be significantly improved by using a pyrex substrate instead of a Si substrate due to the low capacitance and dielectric loss of the pyrex substrate.[17] Again, in this work, pyrex-based BN pores exhibit two orders lower dielectric noise level than Si based, and the reduced dielectric noise permits sub 5 pA root mean square (RMS) noise level at 10 kHz frequency. The flicker noise level was compared using a single layer of h-BN versus multiple layers of h-BN. Here, the membrane layer(s) was transferred onto a 100 nm thick SiN_x supporting layer with only about an 80 nm opening area diameter. It is shown that the flicker noise power is two orders of magnitude smaller when using multiple layers of BN than when using a single layer.

Finally, we demonstrate how the DNA translocation signal varies with the filter frequency (10 kHz versus 100 kHz) for the translocating signals of a 1 kbp double-stranded DNA. The resulting 2D devices enable a sufficient noise level to measure dsDNA translocation events with a 100 kHz filter frequency. The

dsDNA translocation signal appears quite different depending on the filter frequency employed, which shows the importance of improving both the spatial and temporal resolution of the nanopores

3.2. Experimental details

The fabrication process of the h-BN nanopores is schematically illustrated in figure 3-1a. Firstly, a low dielectric noise substrate of pyrex was prepared. The details of the device fabrication process were reported in our previous works.[17] Briefly, a 200 nm thick a-Si film was deposited on the top and bottom surfaces of a pyrex substrate by low pressure chemical vapor deposition (LPCVD). Then, an a-Si layer was lithographically defined and dry etched while the pyrex substrate was wet-chemically etched using diluted-HF until a microchannel was vertically formed through the substrate. The resulting structure formed a 2 μm circular opening on the top-side of the a-Si layer (Figure 3-1b). Then, a LPCVD SiNx membrane with 100 nm thickness was transferred onto the pyrex substrate, and a sub-100 nm hole was drilled in the SiNx membrane by a focused ion beam (*FIB; Carl Zeiss, AURIGA*), as shown in figure 3-1c. This layer acted as a mechanical supporting layer for the BN membrane. We tried to reduce the area of the opening of the SiN membrane because the mechanical stability of the membrane (or free standing area) is quite important in reducing the flicker noise level.[22, 24]

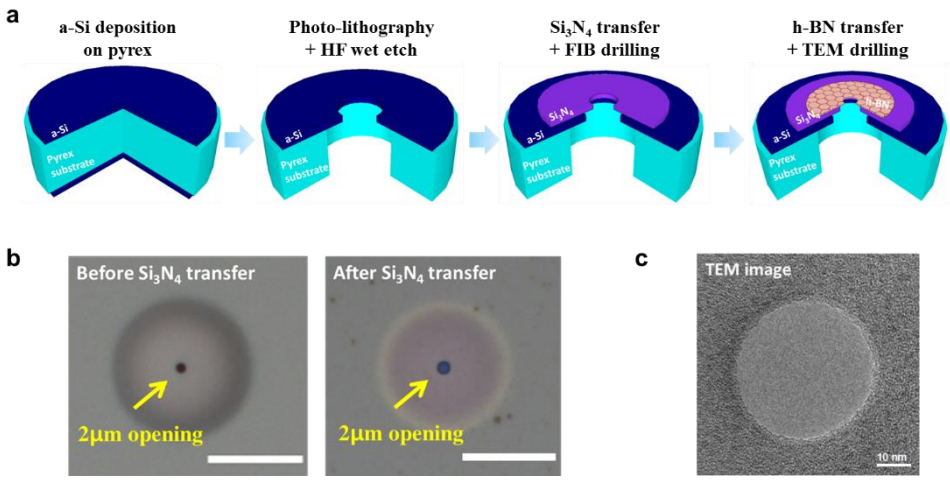

Figure 3-1. Fabrication process of h-BN nanopore. (a) Fabrication steps of h-BN nanopore on pyrex substrate. Thickness of each layer is defined as follows; pyrex – 300 μm, a-Si – 200 nm, SiN_x – 100 nm, h-BN – 6 ~8 layers. (b) Optical microscopy images of the top side of pyrex platform before and after SiN_x layer transfer. Scale bar is 25 μm. (c) TEM image of SiN_x window with sub 100 nm diameter by FIB milling.

Multiple layers of hexagonal-BN (h-BN) films were grown by chemical vapor deposition (CVD) on Cu foil (*Alfa Aesar*, 125μm thickness) using ammonia borane (NH_3-BH_3) as the source gas. The h-BN film grown at this condition was identified to have 6-8 layers by cross-sectional TEM analysis.[31] The h-BN films were then transferred onto the SiN supporting layer by a PMMA coating, wet-chemical etching of Cu foil, and PMMA cleaning with an annealing process. Figure 3-2a shows that the Raman spectrum peak of the h-BN appears at 1366 cm $^{-1}$, which agrees with the published B-N vibration mode (E_{2g}).[32] The XPS data also shows that the binding energies of N 1s and B 1s is 397.8 eV and 190.3 eV, respectively, which are very close to the reported values of the CVD grown h-BN film (Figure 3-2b).[18, 27] Once the BN membrane was transferred onto the SiNx/pyrex sample with a sub-100 nm hole in the SiNx, a nanometer-size pore was drilled in the BN membrane by a transmission electron microscope (*TEM; JEOL JEM 2100F*) with the pore size ranging from 3 to 12 nm.

Before the ionic current measurements of the BN nanopores, the sample was treated with oxygen plasma (*PELCO easiGlowTM*) at a 0.2 mbar working pressure and 15 mA plasma current for 5 min, similarly to the UV-oxygen treatment of the BN layer, to enhance the wettability of the sample.[24] Then, the nanopore chip was mounted on a microfluidic flow cell with a PDMS gasket, and both chambers were filled with a 1 M KCl electrolyte and TE

buffer solution (10 mM Tris-HCl and 1 mM EDTA buffer, pH 8.0). The Ag/AgCl electrodes were inserted into both chambers, and the two electrodes were connected to an Axopatch 200B amplifier with a 250 kHz sampling rate and low pass four-pole Bessel filter at 10 kHz or 100 kHz. For the dsDNA experiments, 1 kbp Fermentas NoLimits DNA fragments (*Thermo Scientific*) were used and 1 nM of dsDNA was inserted into the cis-chamber.

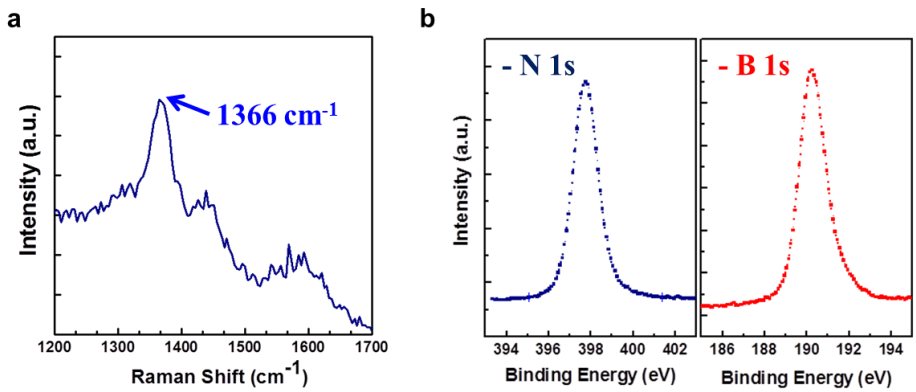

Figure 3-2. Characterization of h-BN film. (a) Raman spectra of transferred BN film on SiO_2/Si substrate. The peak position is 1366 cm^{-1}(b) XPS characteristic of BN thin film on SiO_2/Si substrate. Main peak of N 1s is 397.8 eV and B 1s is 190.3 eV.

3.3. Results and discussion

3.3.1. Ionic conductance measurements

As mentioned in the section of experimental method, h-BN membrane is suspended on SiNx window with sub 100 nm diameter (figure 3-3a). Figure 3-3b shows representative TEM images of nanopores fabricated on multiple layers of h-BN film with sizes ranging from 3 nm to 8 nm. With these device, the I-V responses are measured from -200 mV to 200 mV, as presented in figure 3-4a. The ionic current clearly shows a linear ohmic behavior in the voltage ranges that were measured. In figure 3-4b, the pore conductance value is plotted with respect to the pore diameter. It is known that the pore conductance depends on the pore diameter and thickness of the membrane when the effect of the surface charge is negligible due to the high electrolyte concentration.

$$G_{nanopore} = \sigma_{KCl} / (\frac{4L_{eff}}{\pi D^2} + \frac{1}{D})$$

where, σ_{KCl} is the conductivity of electrolyte solution (11.1 S/m for 1 M KCl), L_{eff} is the effective thickness of the membrane and D is the pore diameter.[33] The first and second term in the equation imply that the channel resistance and access resistance contribute to the conductance. As is shown in figure 3-4a, the pore conductance follows a linear dependency on the pore diameter with an effective membrane thickness of $L_{eff} = 1.4 \pm 0.2$ nm. Considering that our h-BN films have 6 ~ 8 layers with a physical thickness of 2.0 ~ 3.0 nm, this fitting

value is in the reasonable range because the effective thickness is typically smaller than the physical thickness. [34] Moreover, the linear dependency of the pore conductance on the pore diameter indicates that the pore conductance is mainly dependent on the access resistance, as is observed when the membrane thickness is smaller than the pore diameter.

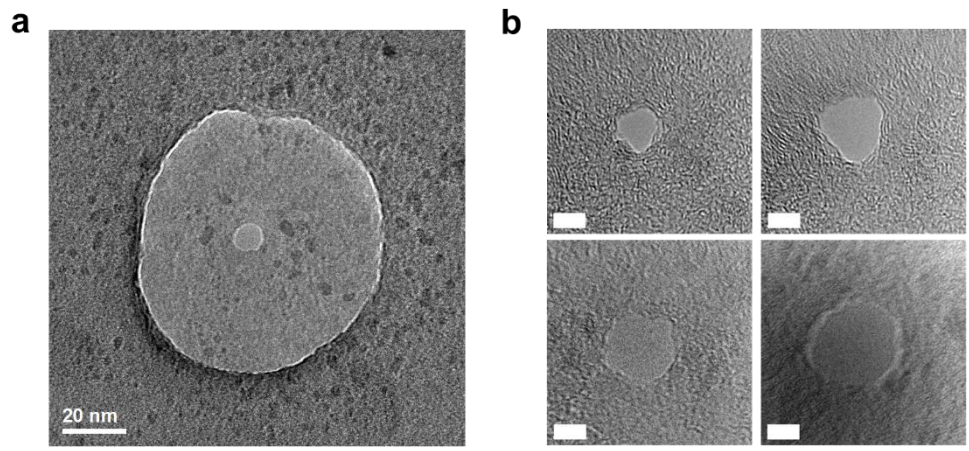

Figure 3-3. Nanopore perforation of h-BN membrane by e-beam radiation in TEM. (a) Low-magnification TEM image of h-BN membrane on SiN_x window. (b) High-magnification TEM image of h-BN nanopores with 3 to 8 nm diameter. Scale bar is 3 nm.

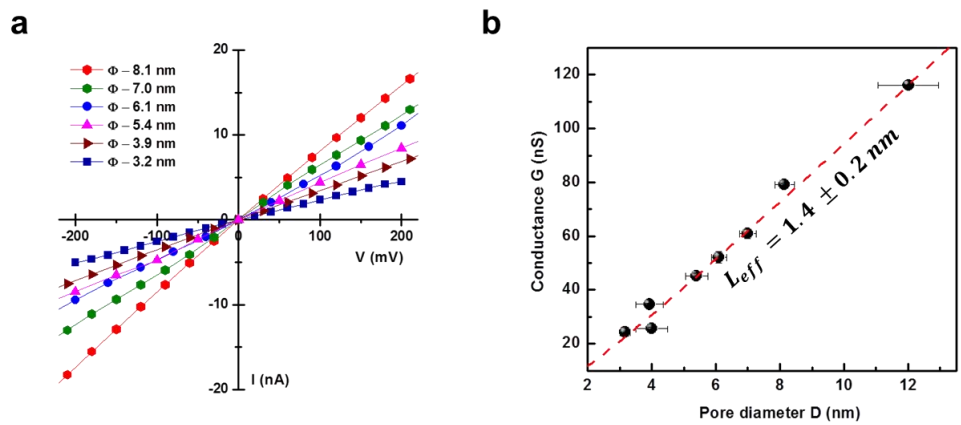

Figure 3-4. Ionic conductance measurement of multi-layered BN nanopores. (a) I-V characteristics of multi-layered BN nanopores with different diameters at 1 M KCl concentration. (b) Conductance vs. pore diameter plot for multi-layered BN devices. The effective thickness value is estimated from fitting into theoretical conductance formula.

3.3.2. Noise characteristics of BN nanopores

Two dominant noise sources of BN devices, named as flicker and dielectric noise, were improved as follow treatments. The dielectric noise was reduced by using a pyrex substrate instead of a Si substrate and then, the flicker noise by using multiple layers of h-BN instead of a single layer of BN; both were transferred to a SiN_x supporting layer with openings smaller than 100 nm. The noise characteristics of the nanopores were analyzed using the power spectral density (PSD, S_I) curve of the measured current traces and the RMS noise (I_{RMS}) obtained from the integration of the PSD with respect to the frequency up to the filter frequency. Here, the power spectral density (S_I) and the RMS noise (I_{RMS}) are expressed as the sum of four different noise sources as follows:

$$S_I = S_{Flicker}(\propto 1/f) + S_{Ther}(\propto 1/R_P) + S_{Dielec}(\propto C_D D_D f) + S_{Amp}(\propto f^2)$$

$$I_{rms}{}^2 = \int S_I df ,$$

$$I_{rms}{}^2 = I_{Flicker}{}^2(\propto \ln(f)) + I_{Ther}{}^2(\propto f/R_P) + I_{Dielec}{}^2(\propto C_D D_D f^2) + I_{Amp}{}^2(\propto f^3)$$

where, f is the frequency, R_P is the pore resistance and C_D and D_D are the capacitance and dielectric loss of the nanopore device.[35, 36] The four noise sources were the flicker noise ($S_{Flicker}$), thermal noise combined with shot noise ($S_{Thermal}$), dielectric noise ($S_{Dielectric}$) and amplifier noise (S_{Amp}), and each source has a specific frequency dependency.

Here, three different types of BN nanopore device structures were prepared to investigate the effect of the structural distinction on the noise properties: (a) *multiple*-BN/SiN_x/Pyrex (b) *single*-BN/SiN_x/Pyrex (c) *single*-BN/SiN_x/Si, where *multiple*-BN and *single*-BN means multiple layers of BN (CVD-growth) and single layer of BN (*Graphene Supermarket*).

Noise comparison with Si and pyrex substrate

To investigate the impact of the substrate material, the ionic current noise of a *single*-BN membrane nanopore fabricated on a conventional Si substrate was compared to that of a *single*-BN nanopore on a pyrex substrate. Figure 3-5a shows 2-second ionic current traces measured at 0 mV and 100 mV of (a) a *single*-BN on Si (red), (b) a *single*-BN on a pyrex substrate (blue), as well as (c) a *multiple*-BN on a pyrex substrate, with a pore diameter of approximately 4 and 5 nm. In addition, Figures 3-5b and 3-6c show the corresponding power spectral density (PSD) curves obtained at 0 mV and 100 mV, respectively. All the data shown in figure 3-5 and 3-6 were measured at a 250 kHz sampling frequency and were filtered at 10 kHz.

First of all, the pyrex-based *single*-BN pore considerably exhibitsthe low dielectric noise (figure 3-5b) due to the low capacitance and dielectric loss of the

pyrex substrate (5~10 pF in 1 M KCl). The dielectric noise level of a pyrex-based device is $3 \times 10^{-8}\ f$ (pA^2/Hz), which is two orders of magnitude lower than that of Si-based device, $5 \times 10^{-6}\ f$ (pA^2/Hz). Because of this large difference, the pyrex-based *single*-BN pore had a lower RMS noise, 3.6 pA$_{RMS,}$ while the Si-based *single*-BN pore had 28 pA$_{RMS}$ measured at 0 mV. When voltage is applied across the pore and the ionic current is measured, flicker noise (*1/f*) is generated as a function of voltage (or ionic current), $S_{Flicker}(f) = A_N I^2/f$, where A_N is the noise power and I is the ionic current.[37] For instance, figure 3-5c shows the PSD of the devices measured at 100 mV. Here, both devices (*single*-BN/pyrex and *single*-BN/Si) show similar *1/f* noise, where each fitting value is $36/f^{1.15}$ and $86/f^{1.15}$ (pA^2/Hz) for the pyrex and Si-based materials from the fitting with the function $S(f) = A/f^{\beta}$ (where A is fitting parameter and $0 < \beta < 2$, which parameter β is commonly close to 1). The slight discrepancy of the *1/f* noise level appears to be caused by the difference in the pore conductance of the two typed of pores, where the conductance of a *single*-BN/Si device ($G = 68\ nS$) is slightly higher than that of *single*-BN/Py device ($G = 43\ nS$). Figure 3-6a shows the corresponding frequency response of I_{RMS} to describe the contribution of each noise source to the total RMS value. The I_{RMS} curves have the plateau over the filter frequency, 10 kHz. The applied voltage (100 mV) across the pore amplified the RMS noise level to 36 pA$_{RMS}$ for the Si-based device and to 15 pA$_{RMS}$ for the pyrex-based device. Dotted lines in figure 3-6a

are the theoretically calculated dependency of *1/f* noise and the thermal + dielectric noise. The *single*-BN pyrex sample exhibited a similar trend to the flicker noise dependency, which means that only the *1/f* noise contributed to total the RMS noise. On the other hand, the flicker noise component of the *single*-BN /Si sample was dominant only up to 3000 Hz, and the remaining frequency domain was governed by the dielectric noise. Thus, the I_{RMS} values of the two pores showed a similar interval as the applied voltage increased from 0 mV to 200 mV in the I_{RMS} versus voltage curve (figure 3-6d), where the slope of this curve means the I_{RMS} dependency on the *1/f* noise and the I_{RMS} of both pores shows the proportional scaling to the applied voltage with a similar slope. In other words, the I_{RMS} of a *single*-BN pyrex pore shows lower values compared to that of a *single*-BN/Si pore because the latter is affected by the high dielectric noise as well as the *1/f* noise in the voltage range we measured.

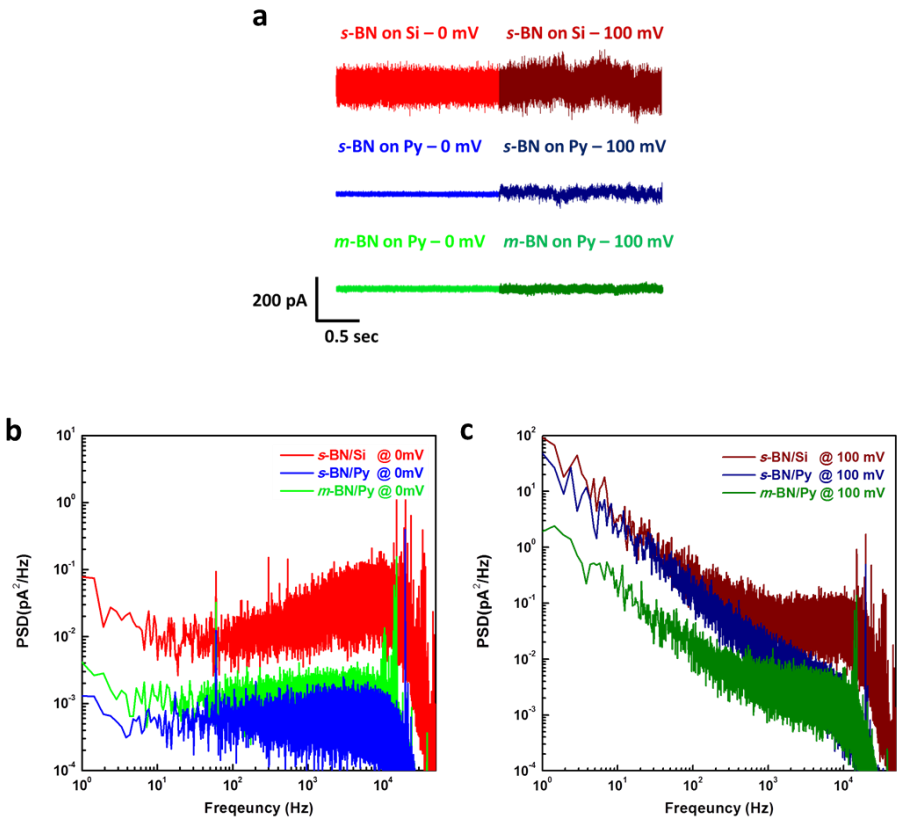

Figure 3-5. Noise analysis of BN nanopore devices with different structures. (a) Ionic current traces of single-layered BN pore on Si (s-BN, Φ 5 nm, G = 68 nS) and s-BN (Φ 4 nm, G = 43 nS) and multi-layered BN pore (m-BN, Φ 8 nm, G = 43 nS) under 0 mV and 100 mV. (b)(c) Power spectral density plots of the corresponding devices to panel a under 0 mV and 100 mV.

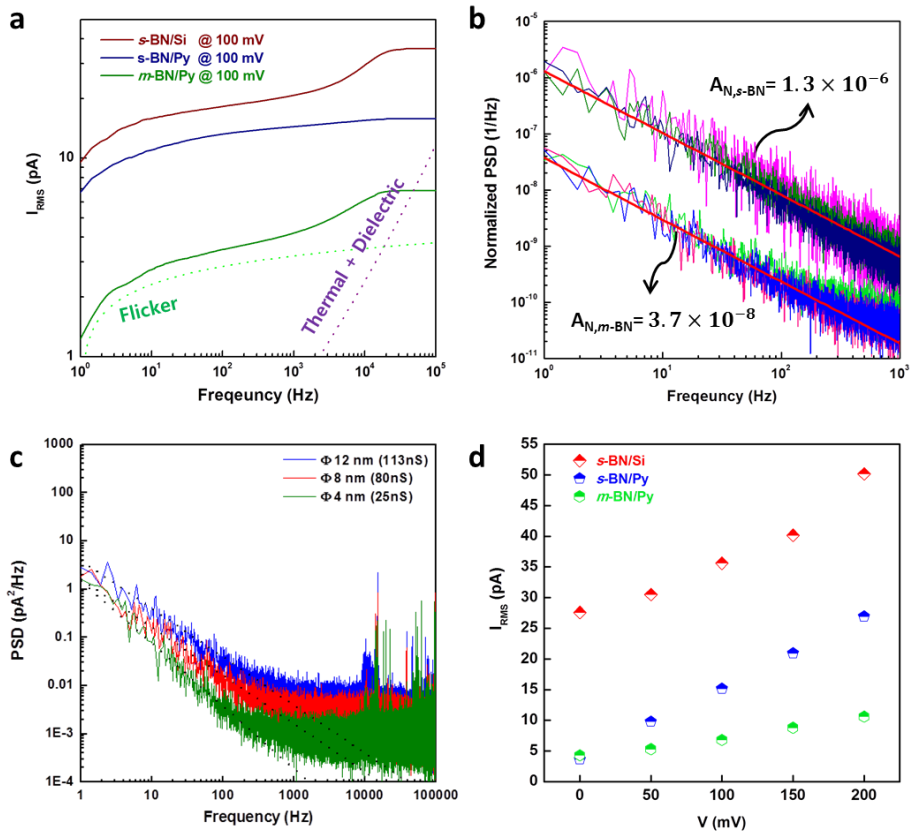

Figure 3-6. Noise characteristics of BN nanopore devices with different structures. (a) I_{RMS} versus frequency curves of s-BN device on Si, s-BN and m-BN device on pyrex. (b) Normalized power spectral density plots at various voltages for s-BN and m-BN device on pyrex. Each linear line results from the fitting of the data into the equation, $\mathbf{S_I/I^2 = A_N/f}$. (c) Power spectral densities of Φ 4 nm (25 nS), 8 nm (78 nS), 12 nm (113 nS) *m*-BN devices at 100 mV. (d) I_{RMS} of the corresponding pores against the applied voltages up to 200 mV.

Noise comparison with single and multiple-BN

Now we will turn our attention to the comparison of single-BN versus multiple-BN membrane with regard to the flicker noise. Figures 3-5a to 3-5c describe the current traces and PSD curves of *single*-BN (blue) and *multiple*-BN (green) on a pyrex substrate at 0 mV and 100 mV. Both the *single*-BN and *multiple*-BN pores show a very close ionic current noise at 0 mV (3.6 pA_{RMS} and 4.3 $pA_{RMS,}$ respectively). The PSD graph at 0 mV illustrates that the *multiple*-BN pore (Φ 8 nm, $G = 79\ nS$) have a slightly higher thermal noise floor than the *s*-BN pore (Φ 4 nm, $G = 43\ nS$) because the thermal noise is proportional to the conductance ($S_{ther} = 4kT/R_{pore} = 4kTG_{pore}$). Again, when voltage was applied, flicker noise was generated and the noise level goes up to 15 and 6.8 pA_{RMS} for the *single*-BN and *multiple*-BN based devices. As shown in figure 3-5c, the *1/f* noise level of the *multiple*-BN based device ($2.3/f^{1.05}$ pA^2/Hz) was one order of magnitude lower than that of the *single*-BN based device ($36/f^{1.15}$ pA^2/Hz). As described in figure3-6c, the *1/f* noise levels of our *multiple*-BN nanopores ranged from *1/f* to *10/f* magnitudes (pA^2/Hz) at 100 mV, depending on the pore size. Figure 3-6b shows the normalized power spectral densities (S_I/I^2) of the *single*-BN and *multiple*-BN nanopores to compare the noise power A_N, which is independent of the current and applied voltage. The PSD of each pore was converted to the normalized PSD with three different voltages, and each of the normalized PSD curves overlap the same

range of magnitudes. Each spectrum was fitted to the following relation, $S_I/I^2 = A_N/f$ to find the value of noise power. The fitting result of A_N was 1.3×10^{-6} (dimensionless) and 3.7×10^{-8} for the *single*-BN and *multiple*-BN pore, respectively.

The A_N value of the multiple-BN nanopores varied from 7.6×10^{-7} to 2.1×10^{-8} as the pore diameter changed from Φ 4 nm to 12 nm. Table 3-1 shows the previously reported values of A_N. Considering the pore size tested, our value of A_N (3.7×10^{-8} for 8 nm pore size, 2.1×10^{-8} for 12 nm pore size) was one order lower than the reported BN pore with Φ 10 nm (6.7×10^{-7}).[24] Additionally, our value is comparable to the A_N value of typical SiN_x pores (5×10^{-8}).[29, 37] This indicates that *multiple*-BN pores combined with the small opening area in the SiNx supporting layer and improved the noise level in response to the applied voltage. This result agrees with the recently published results of the flicker noise reduction with increasing graphene layer thicknesses[15, 16] and small opening window sizes[22, 24], which is explained by the enhancement of the mechanical stability. In Figure 3-6d, the influence of the applied voltage on the I_{RMS} is investigated in corresponding *single*-BN and *multiple*-BN device by varying the voltage from 0 to 200 mV. Figure 3-6d shows that the I_{RMS} values of the *multiple*-BN based pore have a much lower voltage dependency than those of the *single*-BN based pore, where the slope of the former is about four-times

lower than that of the latter. This slope discrepancy is well matched with the difference in the *1/f* noise level of the *single*-BN and *multiple*-BN pore, considering the relation $I_{RMS}^2 = \int S_I df$. As a result of the low 1/f noise dependency, the *multiple*-BN nanopores showed approximately 10 pA_{RMS} even at 200 mV.

Table 3-1. Noise powers values compared with the reported 2-D nanopores.

REF.	Type	Dimension	Supporting layer	A_N, Noise power
[20]	Graphene	Φ 8 nm / 3 ~ 15 layer	Φ 1.5 μm window / SiN 40 nm	7×10^{-6}
	Graphene with TiO2	Φ 7.5 nm / Gr with TiO_2 5 nm		2.5×10^{-7}
[28]	Graphene	Φ 5 nm / few layers (1~3 nm)	Φ 60 ~ 80 nm window/ SiN 20 nm	6.7×10^{-7}
[29]	Graphene	Φ 10 nm / single layer	Φ 1 μm window / SiN 200 nm	6.3×10^{-6}
[24]	BN	Φ 10 nm / 1~2 layer	200 x 200 nm window/ SiN 50 nm	6.7×10^{-7}
Our results	BN	Φ 4 nm / single layer	Φ 60~ 80 nm window/ SiN 100 nm	1.3×10^{-6}
		Φ 4 nm / few layers		7.6×10^{-7}
		Φ 8 nm / few layers		3.7×10^{-8}
		Φ 12 nm / few layers		2.1×10^{-8}

Noise comparison with 10 kHz and 100 kHz

The high bandwidth for nanopore measurements is required to detect accurate current blockades, but increasing bandwidth is accompanied with increasing noise and decreasing SNR. To explore the possibility of high bandwidth, the noise characteristics of the *multiple*-BN pore on a pyrex substrate was measured at 100 kHz bandwidth and compared with that at 10 kHz filter frequency. As an example, figure 3-7a shows the PSD plot of the Φ 8 nm *multiple*-BN pore at 0 and 100 mV, filtered at 10 kHz and 100 kHz. The PSD curves were dampened in the region of each filter frequency. The spectral densities of the 100 kHz filter show a thermal noise floor combined with a low dielectric noise and are located in the 10^{-2} and 10^{-3} pA^2/Hz region at 10^4 to 10^5 Hz frequencies.

Figure 3-7b shows the increase in the I_{RMS} value by the existing thermal and dielectric noise in the 10 - 100 kHz bandwidth as observed in the theoretical fits. Thus, the difference in the I_{RMS} values using the 10 kHz and 100 kHz filter frequencies is almost the same, approximately 8 to 10 pA, and independent of the applied voltage. Although this device showed an RMS noise increase of approximately 10 pA with a 100 kHz filter, the noise level was still below 20 pA_{RMS} at 200 mV as presented in figure 3-7c, which provides sufficient noise level to detect biomolecule translocations.

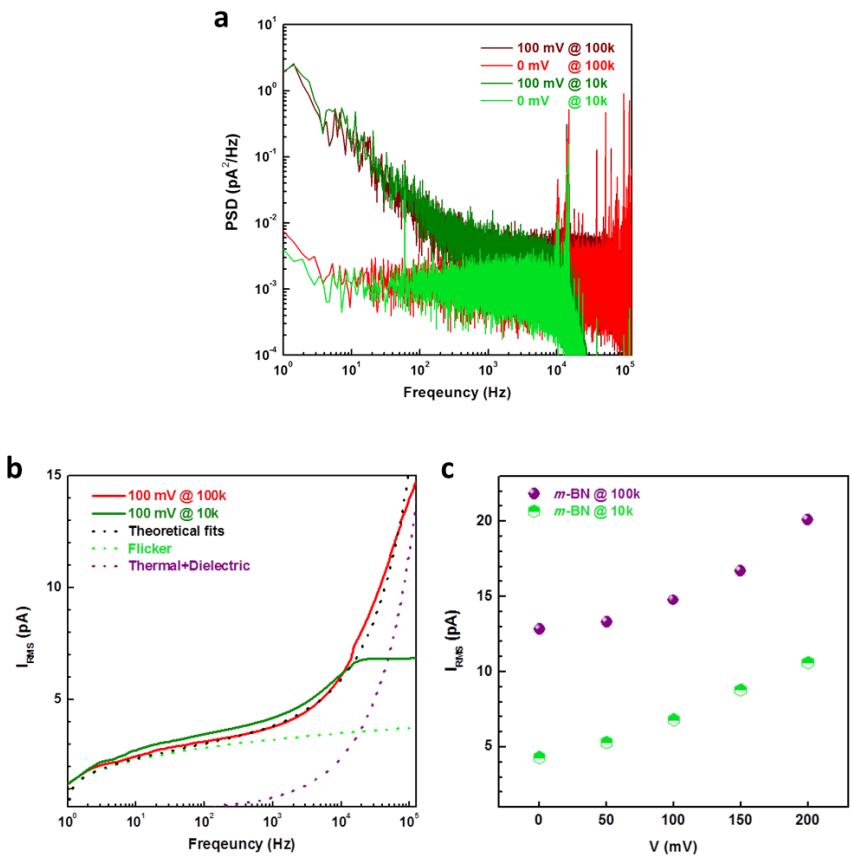

Figure 3-7. Noise characteristics of low-pass filter effect with 10 kHz and 100 kHz. (a) Power spectral densities of *m*-BN pore on pyrex under 0 mV and 100 mV, filtered at 10 kHz and 100 kHz. (b) RMS noise versus frequency curves of the same pore for 10 kHz and 100 kHz filter under 100 mV, as described in panel a. The black dotted line results from the theoretical fits and it can be split into flicker and other noise part. (c) RMS noise of the corresponding *m*-BN pore with 10 kHz and 100 kHz against the applied voltages up to 200 mV.

3.3.3. Double-stranded DNA transport

The translocation events of the 1 kbp ds-DNA through the Φ 4 nm *multiple*-BN pore (25 nS) were measured at different filter frequencies (100 kHz and 10 kHz). The electrolyte solution was 1 M KCl with 10 mM Tris and 1 mM EDTA (pH 8.0), and the concentration of the dsDNA was adjusted to 1 nM. To see the bandwidth effect, 1 kbp ds-DNA were selected for this experiment because the mean translocation time of this size of DNA was reported to locate in 10 μs (100 kHz filter frequency) to 100 μs (10 kHz filter frequency).[9] Figure 3-8a show the continuous ionic current traces measured with 150 mV (black), 200 mV (red) and 250 mV (blue), filtered at 100 kHz. Also, data sets of 10 kHz filter frequency are displayed in figure 3-8d to 3-8e. From the ionic current traces, the real translocation events were additionally collected to exclude bouncing or collision spikes. For instance, the histogram of all current drops of 200 mV is shown in figure 3-9a and it shows two Gaussian distributions. Here, we regard the first Gaussian portion as bouncing spikes and the second Gaussian as real translocation events. Indeed, both t_d and ΔI of the bouncing spikes are independent of the applied voltage (figure 3-9b). So, the events involved in Gaussian distribution of translocations were selected and exhibited in the scatter plots.

The scatter plots for the blockade current (ΔI) and dwell time (t_d) with 150 mV, 200 mV, and 250 mV of the applied voltage are summarized in figure 3-8b

(100 kHz filter) and figure 3-8e (10 kHz filter). It is noted that the mean blockade currents filtered at 10 kHz look about two times lower than the ones filtered at 100 kHz over all the voltage conditions. For instance, the mean blockade current measured at 10 kHz varies from 350 to 550 pA with applied voltages of 150 - 250 mV, while it varies from 600 to 1100 pA when measured at 100 kHz in the same applied volatge range. This tendency means that the translocation events at 10 kHz were distorted due to the relatively short translocation time. In fact, it is known that the signal for fast single molecule events below the temperal resolution is notably attenuated.[38] As is shown in figure 3-8b, the mean dwell time of the 1 kbp ds-DNA translocation measured at 100 kHz was approximately 45, 29 and 23 μs at the applied voltages of 150, 200, and 250 mV, respectively, which is smaller than the temporal resolution of the 10 kHz filter (100 μs). To support this, figure 3-10a shows a 30 sec continuous current trace measured with the 100 kHz filter as well as those digitally filtered to 10 kHz using an 8 pole Bessel filter. In addition, figure 3-10b represents an example of 7 DNA translocation events where the translocation time varied from 20 to 200 μs. This is shown to demonstrate how the electrical filter distorts the blockade signal when $t_d \leq 2\tau_{rise}$, where τ_{rise} is the finite rise time of the filter and is related to the filter frequency f_c: $\tau_{rise} \approx 0.33/f_c$ (= 33 μs for 10 kHz filter).[36, 39] Accodingly, the first four events with a t_d less than 66 μs (=$2\tau_{rise}$) were clearly attenuated by the 10 kHz filter while the DNA events longer than 66 μs

were not.

The normalized histograms of ΔI with three different voltages are shown in figures 3-8c (100 kHz). The mean ΔI values obtained from a Gaussian fitting are shown with respect to the applied voltages in the inset of figure 3-8c. As expected, the ΔI shows a linear dependency on the applied voltages and the slope of the linear fitting matches the blockade conductance ΔG ($\Delta I = V\Delta G$). The measured blockade conductance for 1 kbp dsDNA was 4.3 ± 0.2 nS at 100 kHz. This is the comparable value to ΔG of single layered graphene nanopore with 4 nm diameter, which is ~ 4.8 nS when scaled to 1M KCl ($\Delta G \sim 12$ nS in 3 M KCl).[22] In figure 3-8f, the measured ΔG at 10 kHz was distorted to 2.3 ± 0.1 nS and about two times lower than that at 100 kHz.

Finally, the signal to noise ratio ($SNR = \Delta I / I_{RMS}$) was obtained with respect to the voltages from 150 mV to 250 mV with two different filters (figure 3-11). Although the SNR measured at 100 kHz is lower than those at 10 kHz, our BN pore has a sufficient SNR value at 100 kHz bandwidth (from 40 to 55). This implies that we have a feasibility of applying high bandwidth more than 100 kHz with 1 MHz bandwidth equipment.[40]

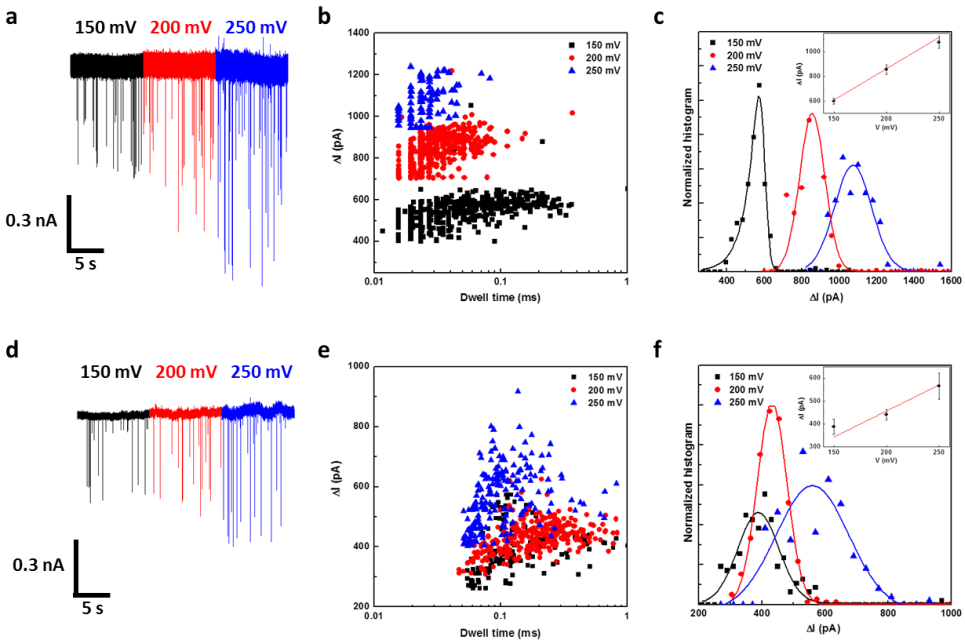

Figure 3-8. dsDNA translocation through m-BN nanopore. (a) Ionic current traces for 1kbp dsDNA translocation at 150 mV (black), 200 mV (red) and 250 mV (blue) through Φ 4 nm m-BN nanopore in 1M KCl with TE buffer (pH 8.0), filtered at 100 kHz. Each trace is measured during 10 sec. (b) The scatter plots of blockade current (ΔI) and dwell time for 150 mV, 200 mV and 250 mV. (c) Normalized histogram of ΔI corresponding to b with different voltages. The inset is blockade current level as a function of voltage, showing linear dependency of ΔI on the applied voltage. (d-e) Similar data set to panel a-c, filtered at 10 kHz.

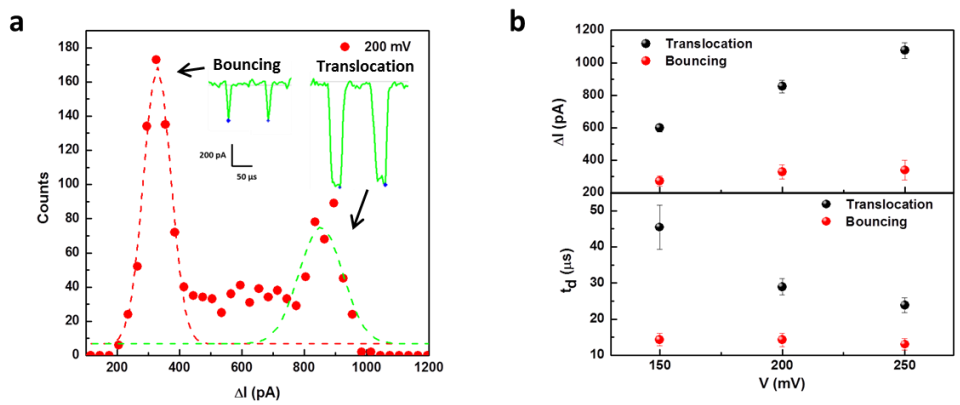

Figure 3-9. An example of criteria to discriminate real translocation events from bouncing or collisions. (a) Histogram of current drops, which magnitude is larger than 10×*I_RMS*, at 200mV and 100 kHz. Inset shows a magnified view of representative bouncing and translocation events. (b) Mean blockade currents and dwell time values of translocations and bouncing as a function of voltage.

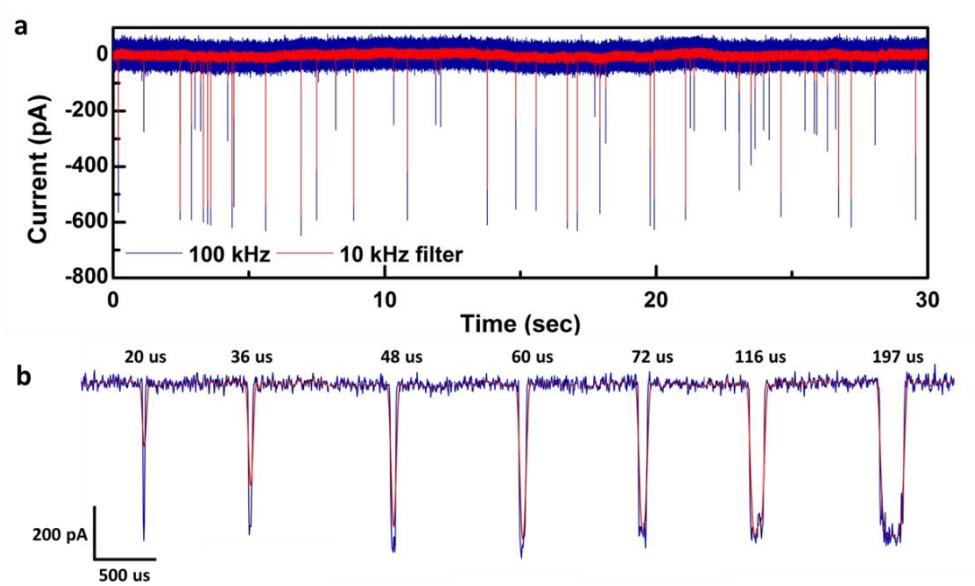

Figure 3-10. Low-pass filter effect on blockade signals. (a) Ionic current traces for 1 kbp dsDNA translocation through Φ 4 nm *m*-BN pore at 150 mV applied voltage, filtered at 100 kHz (blue) and 10kHz (red) in 1M KCl with TE buffer (pH 8.0). (b) A magnified view of 7 DNA translocation events with different duration, ranged from 20 μs and 200 μs.

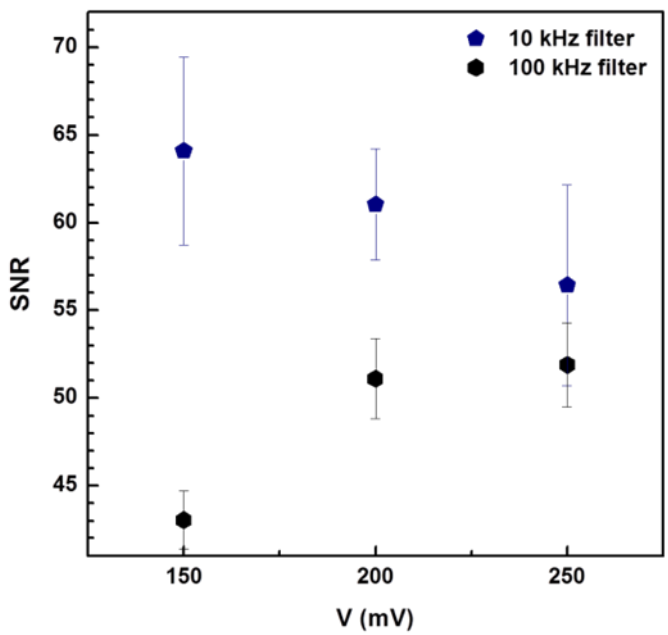

Figure 3-11. Signal to noise ratio as a function of voltage at 10 kHz and 100 kHz; SNR = $\boldsymbol{\Delta I / I_{RMS}}$.

3.3.4. Correlation between stability and 1/f noise

From noise comparison in section 3.3.2, we have found that improving the mechanical stability can lower the 1/f noise level. This result is in good agreements in other reports of 2-D nanopores, including the use of multiple layers[28, 29], small opening area[24] or ALD oxide deposition[20, 41]. Studies to reduce flicker noise in these 2-D nanopores show the indirect effect that mechanical stability can reduce flicker noise, but the mechanical stability is not exactly defined. So we tried to analyze the ambiguous concept of mechanical stability more specifically.

We assume that the suspended thin membrane acts as a circular diaphragm in electrolyte solution and its vibration or fluctuation have an impact on ion flows or fluid flows, resulting in the excess 1/f noise. So, we introduce the specific parameter, the spring constant of circular membrane, and it is expressed as follow,

$$\mathrm{k} = \mathrm{k`} + \mathrm{k``} = \frac{4\pi E t^3}{3D^2(1-v^2)} + 4\pi\sigma t$$

where, E is Young`s modulus, $v$ is Poisson`s ratio of membrane, D and t are the membrane diameter and thickness, respectively, and σ is the biaxial residual stress.[42] The first term results from the stiffness of the suspended membrane due to material characteristics such as Young`s modulus, E or Poisson`s ratio, v. The second term is caused by the biaxial residual stress within the membrane by fabrication process. Here, we consider only the first term of the membrane

stiffness because we can`t define the residual stress in the membrane and its value may not differ significantly from each 2-D nanopores.

To spring constant related to the stiffness, the pore dimension and the membrane diameter in the reported 2-D nanopores are summarized in table 3-2. Also, each flicker noise level is extracted from fitting PSD data into $S(f) = A/f^{\beta}$ and is normalized to a vaule of 100 mV considering the applied voltage. From the summarized values, the plot for $S_{I,100\,mV}$ versus spring constant in the reported 2-D nanopores is described in figure 3-12. As shown in the graph, the values of $S_{I,100\,mV}$ tend to be inversely proportional to the spring constant. It is found that $S_{I,100\,mV}$ decreases as a power of spring constant k`,

$$S_{I,100mV} \propto 1/(k`)^{\alpha}$$

with an exponent $\alpha = 0.48$. This result indicates that the mechanical stability, more directly, the stiffness of the membrane affects the flicker noise of the 2-D nanopore.

Table 3-2. Correlation of spring constant and 1/f noise in 2-D nanopores

REF.	Membrane	Pore dimension	Opening window	Spring constant (*N/m*)	$S_{I,100\ mV}$ (pA²/Hz)
[20]	Graphene	Φ 8 nm / 3~15 layer	Φ 1.5 μm	7.45×10^{-3}	780
	Gr with TiO_2	Φ 7.5 nm / L 6 nm		1.61	6.1
[41]	Graphene	Φ 8 nm / 1~2 layer	Φ 0.3 ~ 0.4 μm	0.04	15
	Gr with Al_2O_3	Φ 8 nm / L 7.6 nm		60.1	2.025
[28]	Graphene	Φ 6 nm / 1 layer	Φ 60 ~ 80 nm	0.045	460
		Φ 5 nm / 8 layer		45.3	35
[29]	Graphene	Φ 10 nm / 1 layer	Φ 1 μm	1.24×10^{-4}	1700
[43]	Graphene	Φ 7.5 nm / L 6 nm	Φ 0.5 μm	14.5	35
[24]	BN	Φ 10 nm / 1~2 layer	Φ 200 nm	0.023	150
[26]	MoS_2	Φ 10 nm / 1 layer	Φ 300 nm	6.39×10^{-3}	107.5
[27]	MoS_2	Φ 10 nm / 1 layer	Φ 100 nm	0.058	137.5
[25]	MoS_2	Φ 10 nm / 1 layer	Φ 400 nm	3.59×10^{-3}	30
This work	BN	Φ 4 nm / 1 layer	Φ 60~ 80 nm	0.033	70
		Φ 4 nm / 8 layer		16.8	5

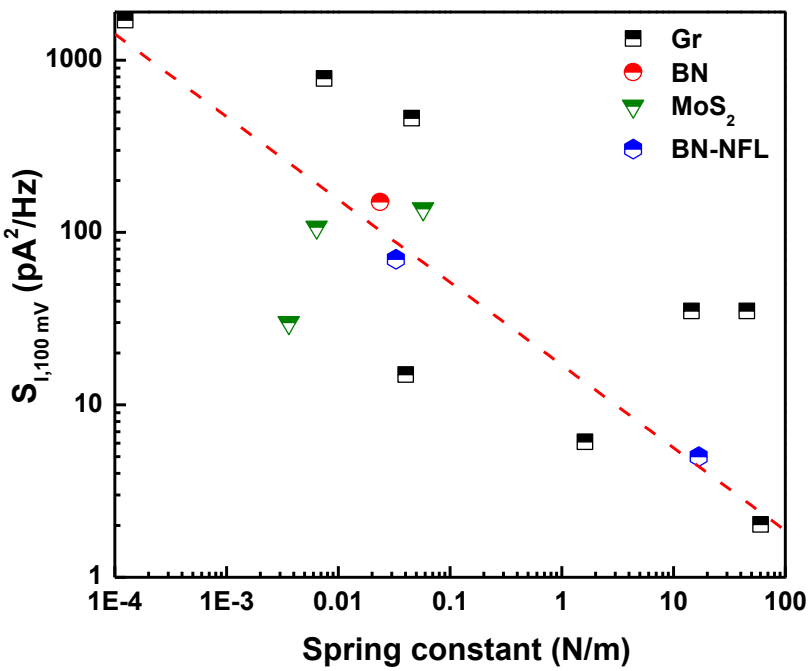

Figure 3-12. Relationship of spring constant and normalized flicker noise level at 100 mV in 2-D membrane nanopores. All data are presented in table 3-2.

3.4. Summary

The aim of the research in this chapter is to improve the noise properties of BN nanopores. We developed the BN pore using a low-noise substrate platform and multi-layered BN membranes with small opening area. After comparing the effect of the substrate material, we demonstrated that our *m*-BN based devices had a lower *1/f* noise level than *s*-BN based devices. As a result of the reduced *1/f* and dielectric noise, the *multiple*-BN pores had an ionic current noise level of 10 pA_{RMS} at 200 mV. With these devise, we detected 1 kbp dsDNA translocation events through low noise *m*-BN nanopores with 100 kHz and 10 kHz filters. We also confirmed that the signal to noise ratio of this device was approximately 50 for both filters. Finally, we found the correlation of mechanical stability and flicker noise in 2-D nanopores by introducing the membrane stiffness. Although we demonstrated simple double-stranded DNA transport with *m*-BN pore in this manuscript, we anticipate that our developed BN nanopores, which have a high SNR, have the potential to identify the four base pairs of DNA and realize DNA sequencing, eventually.

Reference

1. J. Clarke, et al., Continuous base identification for single-molecule nanopore DNA sequencing. *Nat Nanotechnol*, 2009. **4**(4): 265-70.
2. A. H. Laszlo, et al., Decoding long nanopore sequencing reads of natural DNA. *Nat Biotechnol*, 2014.
3. Gerald M. Cherf, et al., Automated forward and reverse ratcheting of DNA in a nanopore at 5-A precision. *Nat Biotech*, 2012. **30**(4): 344-348.
4. Elizabeth A. Manrao, et al., Reading DNA at single-nucleotide resolution with a mutant MspA nanopore and phi29 DNA polymerase. *Nat Biotech*, 2012. **30**(4): 349-353.
5. M. Wanunu, Nanopores: A journey towards DNA sequencing. *Phys Life Rev*, 2012. **9**(2): 125-58.
6. Bala Murali Venkatesan and Rashid Bashir, Nanopore sensors for nucleic acid analysis. *Nat Nano*, 2011. **6**(10): 615-624.
7. T. Gilboa and A. Meller, Optical sensing and analyte manipulation in solid-state nanopores. *Analyst*, 2015. **140**(14): 4733-47.
8. J. L. Li, et al., DNA molecules and configurations in a solid-state nanopore microscope. *Nature Materials*, 2003. **2**(9): 611-615.
9. Cees Dekker, Solid-state nanopores. *Nat Nano*, 2007. **2**(4): 209-215.
10. Meni Wanunu, et al., Rapid electronic detection of probe-specific microRNAs using thin nanopore sensors. *Nat Nano*, 2010. **5**(11): 807-814.
11. Kimberly Venta, et al., Differentiation of Short, Single-Stranded DNA

Homopolymers in Solid-State Nanopores. *ACS Nano*, 2013. **7**(5): 4629-4636.

12. Jiwook Shim, et al., Nanopore-Based Assay for Detection of Methylation in Double-Stranded DNA Fragments. *ACS Nano*, 2015. **9**(1): 290-300.
13. K. J. Freedman, et al., Chemical, thermal, and electric field induced unfolding of single protein molecules studied using nanopores. *Anal Chem*, 2011. **83**(13): 5137-44.
14. D. Fologea, et al., Electrical characterization of protein molecules by a solid-state nanopore. *Appl Phys Lett*, 2007. **91**(5): 539011-539013.
15. Calin Plesa, et al., Fast Translocation of Proteins through Solid State Nanopores. *Nano Letters*, 2013. **13**(2): 658-663.
16. J. S. Yu, et al., Identifying the Location of a Single Protein along the DNA Strand Using Solid-State Nanopores. *ACS Nano*, 2015. **9**(5): 5289-98.
17. Min-Hyun Lee, et al., A Low-Noise Solid-State Nanopore Platform Based on a Highly Insulating Substrate. *Scientific Reports*, 2014. **4**: 7448.
18. Daniel Fologea, et al., Detecting Single Stranded DNA with a Solid State Nanopore. *Nano Letters*, 2005. **5**(10): 1905-1909.
19. S. Garaj, et al., Graphene as a subnanometre trans-electrode membrane. *Nature*, 2010. **467**(7312): 190-3.
20. C. A. Merchant, et al., DNA translocation through graphene nanopores. *Nano Lett*, 2010. **10**(8): 2915-21.
21. G. F. Schneider, et al., DNA Translocation through Graphene

Nanopores. *Nano Letters*, 2010. **10**(8): 3163-3167.

22. S. Garaj, et al., Molecule-hugging graphene nanopores. *Proc Natl Acad Sci U S A*, 2013. **110**(30): 12192-6.
23. S. Liu, et al., Boron Nitride Nanopores: Highly Sensitive DNA Single-Molecule Detectors. *Adv. Mater*, 2013. **25**: 4549-4554.
24. Z. Zhou, et al., DNA Translocation through Hydrophilic Nanopore in Hexagonal Boron Nitride. *Sci Rep*, 2013. **3**: 3287.
25. P. Waduge, et al., Direct and Scalable Deposition of Atomically Thin Low-Noise MoS2 Membranes on Apertures. *ACS Nano*, 2015. **9**(7): 7352-9.
26. Ke Liu, et al., Atomically Thin Molybdenum Disulfide Nanopores with High Sensitivity for DNA Translocation. *ACS Nano*, 2014. **8**(3): 2504-2511.
27. Jiandong Feng, et al., Identification of single nucleotides in MoS2 nanopores. *Nat Nano*, 2015. **10**(12): 1070-1076.
28. A. Kumar, et al., Noise and its reduction in graphene based nanopore devices. *Nanotechnology*, 2013. **24**(49): 495503.
29. S. J. Heerema, et al., 1/f noise in graphene nanopores. *Nanotechnology*, 2015. **26**(7): 074001.
30. Kenji Watanabe, et al., Direct-bandgap properties and evidence for ultraviolet lasing of hexagonal boron nitride single crystal. *Nat Mater*, 2004. **3**(6): 404-409.
31. K. H. Lee, et al., Large-scale synthesis of high-quality hexagonal boron nitride nanosheets for large-area graphene electronics. *Nano Lett*, 2012. **12**(2): 714-8.

32. Roman V. Gorbachev, et al., Hunting for Monolayer Boron Nitride: Optical and Raman Signatures. *Small*, 2011. **7**(4): 465-468.

33. Stefan W. Kowalczyk, et al., Modeling the conductance and DNA blockade of solid-state nanopores. *Nanotechnology*, 2011. **22**(31): 315101.

34. M. J Kim, et al., Rapid Fabrication of Uniformly Sized Nanopores and Nanopore Arrays for Parallel DNA Analysis. *Advanced Materials*, 2006. **18**(23): 3149-3153.

35. V. Dimitrov, et al., Nanopores in solid-state membranes engineered for single molecule detection. *Nanotechnology*, 2010. **21**(6): 065502.

36. Jeffrey D. Uram, et al., Noise and Bandwidth of Current Recordings from Submicrometer Pores and Nanopores. *ACS Nano*, 2008. **2**(5): 857-872.

37. R. M. M. Smeets, et al., Noise in solid-state nanopores. *Proceedings of the National Academy of Sciences of the United States of America*, 2008. **105**(2): 417-421.

38. J. K. Rosenstein, et al., Integrated nanopore sensing platform with sub-microsecond temporal resolution. *Nat Methods*, 2012. **9**(5): 487-92.

39. Daniel Pedone, et al., Data Analysis of Translocation Events in Nanopore Experiments. *Analytical Chemistry*, 2009. **81**(23): 9689-9694.

40. A. Balan, et al., Improving Signal-to-Noise Performance for DNA Translocation in Solid-State Nanopores at MHz Bandwidths. *Nano Lett*, 2014. **14**(12): 7215-20.

41. Bala Murali Venkatesan, et al., Stacked Graphene-Al2O3 Nanopore

Sensors for Sensitive Detection of DNA and DNA–Protein Complexes. *ACS Nano*, 2011. **6**(1): 441-450.

42. Gabriel M Rebeiz, *RF MEMS: theory, design, and technology, Chapter 2. Mechanical Modeling of MEMS Devices: Static Analysis*. 2004, John Wiley & Sons.

43. Pradeep Waduge, et al., Programmed Synthesis of Freestanding Graphene Nanomembrane Arrays. *Small*, 2015. **11**(5): 597-603.

Chapter 4.

Slow DNA Translocation through Zinc Oxide Nanopores in Transfer-free Quartz platform

4.1. Introduction

Nanopore technologies have drawn considerable attention as an emerging technology for detection and analysis of DNA, RNA, proteins and DNA-protein complexes on a single molecule basis.[1-4] In particular, nanopore sensors have been developed to achieve long-read single-molecule DNA sequencing with very high throughput at low cost.[5-7] Here, the charged molecules are electrophoretically driven through the nanopore, resulting changes in ionic current, which can be associated with the sequence of nucleotides. There have been a series of impressive developments in the field of protein nanopores using α-heamolysin[8] or MspA[9] since they possess such advantages of (i) an excellent low noise level, (ii) the reproducible formation of small-sized pore (< 1.5 nm) and (iii) an extreme thin sensing zone of approximately 1 nm. Especially, the introduction of polymerase enzymes, which regulate the motion of single-strand DNA to one base pair at a time, on biological nanopore platform led a closer to DNA sequencing.[10-12]

On the contrary, the progress of solid-state nanopores has been much slow and limited to merely detecting either the translocation of DNA molecules or the DNA-protein interactions till now, although solid-state nanopore platforms offer obvious merits over biological nanopores such as long-term stability, controllable pore geometry, and the possibility to integrate with other sensing mechnisms such as electronic tunneling or optical sensing techniques.[7, 13] In order to provide comparable device to the protein nanopore, the remaining challenges of solid-state nanopore include (i) enhancing signal to noise ratio to differentiate each nucleotides (ii) spatial resolution and (iii) temporal resolution

of ionic current signals containing single nucleotide. Until now, only a few group have reported in distinguishing single-stranded DNA homopolymers, with the help of the high bandwidth equipment[14] or the low noise substrate[15].

Studies to reduce noise in solid-state nanopores have been conducted in the direction of lowering the well-known noise sources of flicker noise, thermal noise at low frequency (< 1 kHz) and dielectric noise, amplifier noise at high frequency.[16, 17] In recent years, the importance of high frequency noise has increased, which is related to the development of an amplifier capable of measuring bandwidth above 1 MHz.[18] Extending measurement bandwidth offers temporal resolution in microseconds, but it is accompanied by an increase in RMS noise due to the influence of expanded high frequency noise, resulting from the parasitic capacitance of nanopore chip. Up until now, several efforts have focused on reducing the chip capacitance such as polymeric material sealing[17, 19], thick dielectric layer deposition underneath an active membrane[14, 18] and glass based platform instead of Si substrate[15, 20-22]. Of these, a glass based low noise platforms have been reported to reduce capacitance to sub 5 pF. Currently, two methods have been developed to fabricate glass substrate-based solid-state nanopores, all of which have their own limitations. Kim`s group have developed the two step wet-etching of glass substrate to confine the opening window of active membrane into 2 μm, which need additional transfer proess of $SiN_x$.[20] Drndic`s group have reported the two step wet etching method without membrane transfer, where it need an electron beam lithography to control the opening window of SiN_x membrane.[22]

In terms of improving current signals of DNA blockade, the amplitude of blockade signals is enhanced with the smaller pore diameter and the thinner

thickness membrane.[23-26] In particular, many research have highlighted on the fabrication of thin membrane because the membrane thickness is related to the spatial resolution, as well as the current blockage. For instance, 2-D materials[27-30] and ALD-grown oxides involving Al_2O_3[31, 32] and HfO_2[33, 34] have been applied as sensing membrane. In particular, atomic layer deposition (ALD) process is able to meet the needs of solid-state nanopores for the precise thickness control at sub-nanometer level and the mechanical stability of the membranes with sub-10 nm thickness.[35] Still, however, only two oxides, Al_2O_3 and HfO_2, have been demonstrated the viability to nanopore devices.

In this chapter, we develop transfer-free fabrication process of solid-state nanopore platform based on quartz substrate with the membrane of 2 μm opening aperture by using a polycrystalline Si (poly-Si) as a protection layer. Furthermore, we investigate the feasibility of zinc oxide (ZnO) nanopores. ZnO has attracted great interest as a wide band gap (3.37 eV) semiconductor for application in transparent electrode due to its optical properties, long term stability and large exciton binding energy (60 meV).[36] In addition, various ZnO nanostructures also are considered for biomedical applications because of their high chemical stability, non-toxic nature, easy surface modification, good biocompatibility, and high isoelectric point (~9.5).[37] Moreover, hexagonal wurtzite ZnO have a possibility to form two dimensional layer by transformation to a trigonal plarnar coordination.[38] Nevertheless, the application of ZnO as a membrane material for nanopore DNA-sensing has not been studied yet, to our knowledge. First, we display the fabrication scheme of ultrathin ZnO membrane

by atomic layer deposition (ALD) on transfer-free platform and the nanopore formation using focused e-beam radiation in TEM. Then, we analyze ionic current and noise characteristics in such nanopores. Finally, we demonstrate the first translocation of double-stranded DNA through ZnO nanopores and observed their translocation speeds are much slower than that of SiN_x nanopore. For further understanding the slow effect of ZnO device, we propose that the electrostatic interaction between positively charged ZnO pore wall, resulted from high isoelectric point of ZnO, and negatively charged phosphate backbone provides additional frictional force to slow down the DNA translocation.

4.2. Experimental details

Nanopore device preparation

The overall fabrication process of transfer-free platform on quartz substrate is described in figure 4-1a. To fabricate transfer-free low noise platform based on quartz substrate, quartz substrate (300 μm thickness) was prepared because it has a high softening temperature (~ 1665 ℃) allowing the low pressure chemical vacuum deposition (LPCVD) process for high quality SiN_x films. On both sides of quartz wafer an amorphous Si (a-Si) layer of 200 nm thickness and a SiN_x layer of 100 nm thickness were deposited by LPCVD process, where a-Si is used as a HF etch mask and SiN_x as active membrane. Then, a layer of 200 nm-thick polycrystalline Si (poly-Si) was deposited on top side on SiN_x and it acted as supporting layer of active membrane with 2 um opening window. After photo-lithography and reactive ion etching process on both sides, the top of poly-Si was etched with an opening aperture of 2 um. To create microfluidic channel through quartz substrate, we performed sandblast process combined with HF wet-etching. A 150 x150 mm^2 opening area was defined on the other side of the substrate by lithography and RIE. Thereafter, most depth (~250 μm) of quartz water was etched by sandblast process and the remained portion was removed by HF wet etching. After the a-Si layer was etched by a wet KOH etching, the free-standing SiN_x membrane was formed.

Zinc oxide layer was deposited on the freestanding SiN_x layer by atomic layer deposition process (ALD). ALD equipment (LUCIDA D-100, NCD technology) was operated at a deposition temperature of 200C. The used

precursors are diethylzinc (DEZ) and H_2O, and the total cycle is 45 for 7 nm thickness (~0.14 nm/cycle). To leave only ZnO membrane, SiN_x was selectively removed by reactive ion etching with CF_4 gas. Finally the nanopores were drilled into the ZnO membrane by a highly focused electron beam using a JEOL 2010F TEM with a modified TEM holder.

Nanopore measurements

Prior to ionic current measurement, the nanopore chip was treated with oxygen plasma (*PELCO easiGlow*^{TM}) at a 0.2 mbar working pressure and 10 mA plasma current for 5 min to enhance the wetting property of the sample. Then, 5 mm x 5mm nanopore chip was mounted on a custom-made PTFE microfluidic flow cell with a 3 mm diameter PDMS gasket, and both chambers were filled with a 1 M KCl electrolyte and TE buffer solution (10 mM Tris-HCl and 1 mM EDTA buffer, pH 8.0). The Ag/AgCl wire electrodes were inserted into both chambers, and the two electrodes were connected to an Axopatch 200B amplifier with a 250 kHz sampling rate. All ion currents data in this work were measured with low pass four-pole Bessel filter at 100 kHz. For the dsDNA experiments, 1 kbp Fermentas NoLimits DNA fragments (Thermo Scientific) were used and 1 nM of dsDNA was inserted into the cis-chamber. Translocation events were collected and analyzed using Clampfit 10.4 software. To distinguish real translocations from collision or bouncing spikes, events with blockade current larger than 10 times of noise rms values are determined as real translocations.

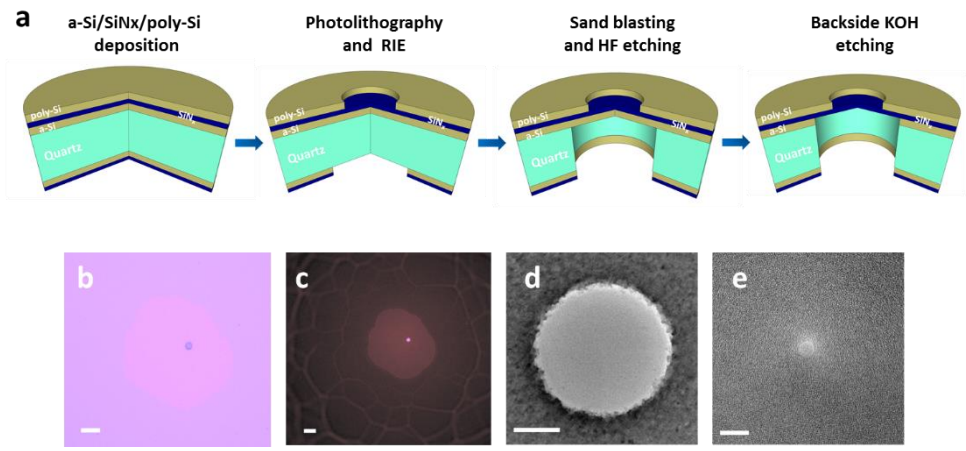

Figure 4-1. Fabrication of transfer-free device on quartz substrate. (a) Overall fabrication process of the transfer-free nanopore platform based on quartz substrate. (b)(c) Optical microscope image of top and bottom side of nanopore device with micrometer sized window. (scale bar: 10 μm) (d) Transmission electron microscopy (TEM) images of a free-standing SiN_x membrane with poly-Si supporting layer. An aperture size of poly-Si is 2~3 μm. (scale bar: 1 μm) (e) TEM image of 4 nm diameter nanopore perforated in SiN_x membrane. (scale bar: 10 nm)

.

4.3. Results and discussion

4.3.1. Fabrication of transfer-free platform

Figure 4-1a illustrates the fabrication steps for this nanopore device based on quartz substrate, which has a high softening temperature (~1665 ℃) allowing the low pressure chemical vacuum deposition (LPCVD) process for high quality SiN_x film deposition. Detailed process steps are described in the experimental detail section. Unlike our previous report[15], we performed a sandblast process combined with HF wet etching to create microfluidic channel through quartz substrate because of extremely slow etch rate of quartz by wet HF etching. After coating dry resist film on the bottom side, the quartz substrate was mostly etched down to ~ 250 um depth by sand blasting and the remaining was perforated by wet chemical etching under 49 % HF. As shown in figure 4-1b and 4-1c, the bottom opening area of SiN_x membrane is approximately 100 x 100 um^2, but the top opening aperture of SiN_x is defined to ~2 um by the poly-Si supporting layer. Such confinement of SiN_x is helpful to reduce the chip capacitance, as well as to enhance the mechanical stability.

Figure 4-2 shows calculated chip capacitance as a function of opening diameter of SiN_x membrane. The C_{chip} can be calculated by the corresponding circuit model, $C_{chip} = \sum \varepsilon_i \left({}^{A_i}/_{L_i}\right)$ [21], and parameters of chip structure are described in the table 4-1. At 10 um diameter of membrane, the chip capacitances

is both less than 2 pF irrespective whether it has poly-Si supporting layer or not. However, the chip capacitance is becoming much different as the opening window increases. For instance, the chip with 2 um poly-Si supporting has a value less than 5 pF, while the chip without supporting layer have more than 50 pF at 100 um opening. In other words, the introduction of poly-Si supporting layer lowers the chip capacitance efficiently regardless of the opening size by HF etching. This transfer-free platform can be used directly with SiN nanopores through membrane thinning and poring processes (figure 4-1d and 4-1e).

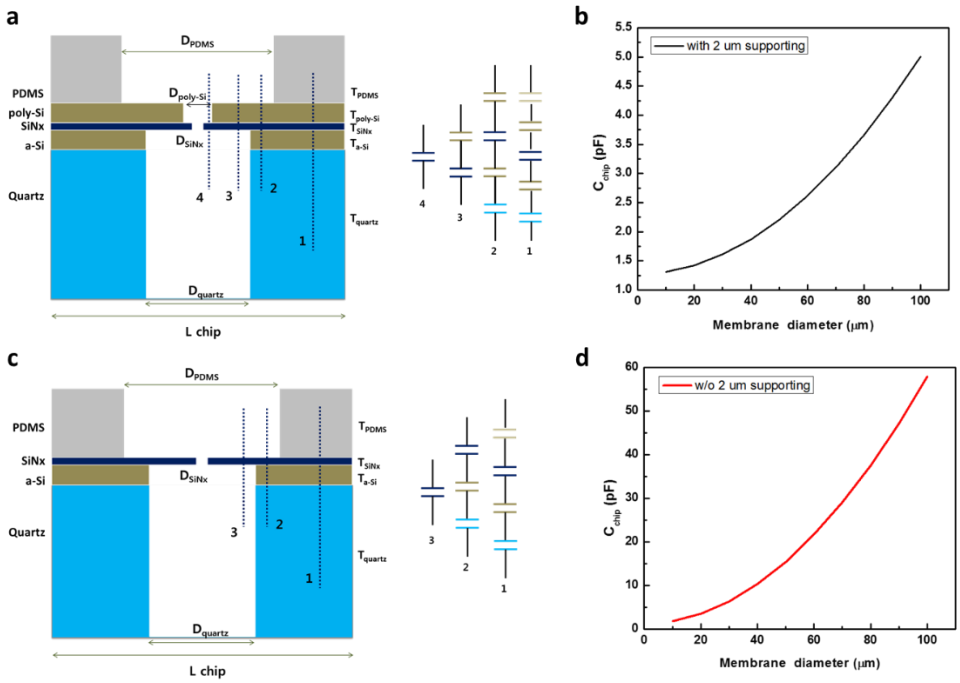

Figure 4-2. Chip capacitance calculation considering chip structure. (a) Schematic image of quartz-based chip structure with poly-Si supporting layer. The labeled vertical region is the series connection of the capacitance, and the total capacitance is calculated by the parallel connection of the capacitance of each region. (b) The calculated chip capacitance as a function of opening diameter with the device corresponding to panel a. (c) Schematic image of quartz-based chip structure without poly-Si supporting layer. The calculation procedure is same to panel a. (d) The calculated chip capacitance as a function of opening diameter with the device corresponding to panel c.

Table 4-1. The specific chip parameters including dielectric constant of each material and the geometry of each layer.

	Dielectric constant		dimension		Thickness
PDMS	2.55	Chip size	5 x 5 mm		
LP SIN	8.15	Quartz	10 ~ 100 um	Quartz	300 um
		a-Si	100 um	a-Si	200 nm
Si	11.5	pore size	5 nm	SiN	10 nm
Quartz	4.35	PDMS	3 mm	PDMS	1 mm
		poly-Si	2 um	poly-Si	200 nm

4.3.2. Fabrication of ZnO nanopores

The fabrication process of the ZnO nanopores on transfer-free platform is schematically illustrated in figure 4-3a. In fact, we can use SiN_x membrane directly as a membrane material. However, it is not an easy matter to thin down the SiNx layer less than 10 nm scale. Therefore, we used the fabrication method of controllable deposition and selective etching of underneath layer, which makes it easier to have thin membrane. On the top side of SiN_x membrane, crystalline ZnO film with 7-nm thickness was deposited by atomic layer deposition (ALD), which have merits of excellent uniformity, conformal deposition, precise control of thickness and high reproducibility.[35] The deposition rate of ALD ZnO is ~0.14 nm/cycle, which was confirmed in our previous report using spectroscopic ellipsometry.[39] Then, the entire SiN_x layer on back side was etched by reactive ion etching (RIE) using CF4 gas, which is the well-known etchant for Si compounds but is reported to have very small etching rate on ZnO film.[40] After slightly over-etching of SiN_x layer, the free-standing ZnO membrane was formed in the 2 um hole as seen in scanning electron microscope (SEM) image (figure 4-3b). The elemental composition of membrane region was investigated using energy dispersive X-ray spectroscopy (EDS) with scanning electron microscope (AURIGA, Carl Zeiss). In figure 4-3c, EDS elemental analysis on 2 um etched area of samples before and after SiN_x layer etching were performed. As shown in figure 4-3c, the peaks for Si, Zn and O elements were characterized in both

spectra but N signal were not detected in SiN_x-etched sample, which means the layer of SiN_x was clearly removed. In addition, EDS carried out in the mode of elemental mapping. Figure 4-3b shows the EDS mapping of Si, Zn and O signals, where Zinc and Oxygen elements were detected in the entire mapping region, but Si signal was rarely detected in the etched area of poly-Si layer. In particular, the signals of zinc and oxygen were detected more densely around the edge of the hole. It can be explained by the conformal deposition of ALD ZnO film on the micro pore wall of poly-Si and the electron penetration into a relatively thick region in the vertical axis. The EDS line scan describing the distribution of Si, Zn and O across the membrane shows the same tendency of EDS mapping results. As seen in figure 4-3d, the distributions of Zn and O have a relatively high signal only near the edge of the micro pore and show a similar signal both inside and outside of the membrane. On the other hand, the signal of Si shows a clear difference between the inside and the outside of the membrane, and the point of decrease of Si distribution exactly coincides with that of increase of Zn and O. These results imply the formation of stable ZnO membrane by conformal deposition of ALD process and the selective removal of SiN_x layer.

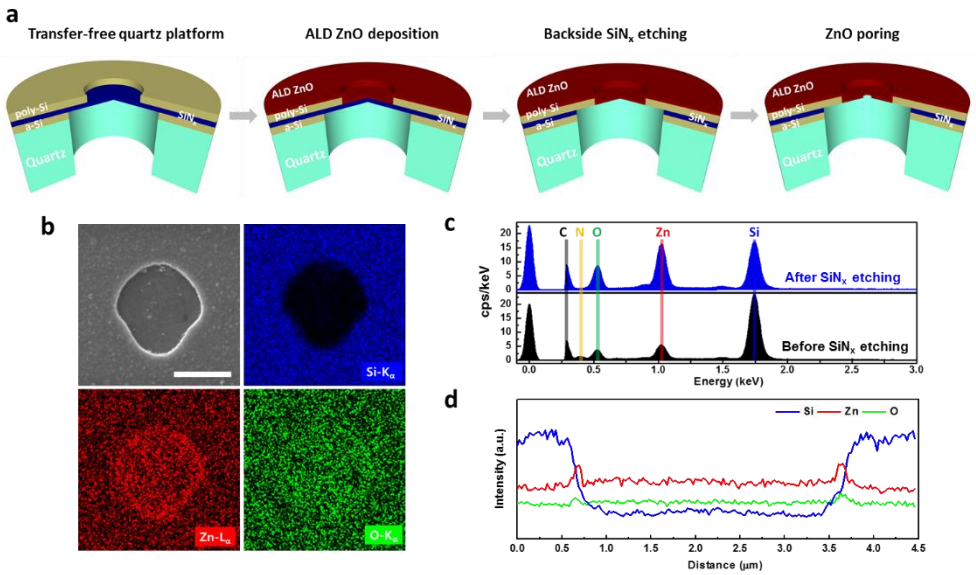

Figure 4-3. ZnO device on transfer-free platform. (a) Fabrication process of ZnO nanopore on transfer-free platform. A 7-nm thick ZnO is deposited by atomic layer deposition on suspended SiN_x window. The free-standing ZnO membrane is formed by selective removing of SiN_x using reactive ion etching, (b) SEM image of an area of ZnO membrane and EDS elemental mapping of Si, Zn and O in this region. (scale bar: 1 μm) (c) EDS spectra of micro-hole region in ZnO nanopore devices before and after SiN_x layer etching. (d) EDS line scan of Si, Zn and O elements across ZnO membrane.

4.3.3. Characterization of ZnO nanopores

Figure 4-4a shows the TEM image and selective area electron diffraction pattern (SAED) of the free-standing ZnO membrane. The SAED pattern indicate ALD ZnO film is a polycrystalline with the wurtzite structure. The plane distances of 1st to 3rd diffraction rings were estimated to be 2.86, 2.64 and 2.52 Å, respectively, and these values are in good agreement with $(10\bar{1}0)$, (0002) and $(10\bar{1}2)$ planes of wurtzite ZnO. The final fabrication step was nanopore drilling by highly focused electron beam using TEM (JEOL 2010F, 200 kV). By controlling the beam current density and drill time, nanopores with 1.3 nm to 6 nm diameter were perforated as seen in figure 4-4b. In previously reported ALD oxide nanopores such as Al_2O_3 and HfO_2, phase transitions were observed during pore formation from amorphous phase to poly- or nanocrystalline phase.[31, 33] Unlike these ALD oxides, ZnO films maintained the polycrystalline structure after e-beam irradiation. The poring process of most ZnO nanopores were completed in less than one minute like SiN_x nanopores with similar thickness.

Following nanopore fabrication, the devices were treated with oxygen plasma to remove organic contaminations and enhance wettability of the pores. After the nanopore chip was mounted on a custom-made PTFE flow cell with a PDMS gasket, the ionic conductances of ZnO nanopores were measured in 1M KCl electrolyte solution with TE buffer (pH 8.0) using Axopatch 200B amplifier. Figure 4-4c shows the current-voltage curves for ZnO nanopores with 1.3 nm

(green), 4.0 nm (red) and 6.0 nm (blue) diameter. The ionic currents clearly show a linear and ohmic behavior as a function of the applied voltage. From the slope of I-V curves, each conductance value is estimated to be 2.1 nS, 14 nS and 24 nS, respectively. For high ionic strength concentration (>0.1 M), the ionic conductance G are determined by the pore diameter *d* and the effective membrane thickness L_{eff}.

$$G = \sigma\left(\frac{4L_{eff}}{\pi d^2} + \frac{1}{d}\right)^{-1}$$

where, σ is the conductivity of the electrolyte solution (10.5 S/m for 1 M KCl). From conductance equation, the effective thickness of ZnO membrane was approximately 6 nm to 8 nm, which is similar value to the physical thickness, 7 nm. Typically, the effective pore length is smaller than physical thickness since the nanopore of TEM drilling have an hourglass-shaped structure.[41] Unlike SiN_x pore, the unexpected high thickness was observed in HfO_2 nanopores, which is the effect of local crystallinity in e-beam radiation.[34] Therefore, in our ZnO nanopores, poring kinetics in polycrystalline membranes may be different from amorphous SiN_x membrane and may result in larger effective thickness value over physical thickness.

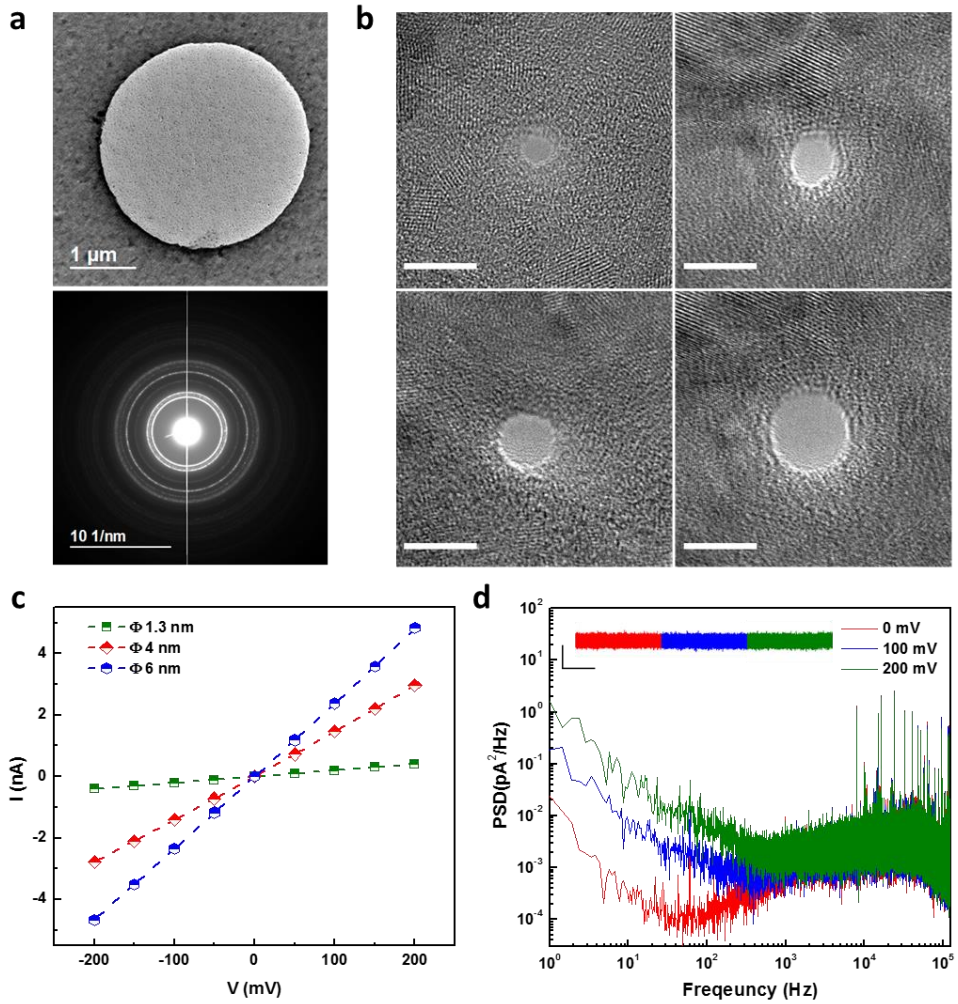

Figure 4-4. Characteristics of ZnO nanopores. (a) TEM image of a free-standing ZnO membrane and the corresponding selective area electron diffraction (SAED) pattern. (b) High-resolution TEM images of representative ZnO nanopores with estimated 1.3, nm (scale bar: 5 nm) (c) Ionic current vs. voltage characteristics for three ZnO nanopores of 1.3, 4 and 6 nm diameters. (d) Power spectral densities (PSD) of 1.3 nm pores (2 nS) under 0, 100 and 200 mV voltages in 1 M KCl electrolyte solution with TE buffer (pH 8.0), filtered at 100 kHz.

The noise characteristics were also analyzed from the power spectral density (PSD) plots. Figure 4-4d is the PSD graph of Φ 1.3 nm ZnO pore (2.1 nS) at 0, 100, 200 mV. The PSD data were obtained at a 250 kHz sampling rate and 100 kHz filter. Similar to other ALD oxide nanopores, ZnO nanopore exhibited good 1/f noise levels (< $1/f$ $\mathrm{pA^2/Hz}$). From the fitting with the function $S_{I,Flicker}(f) = A/f^{\beta}$ (where A is fitting parameter and $0 < \beta < 2$, which parameter β is commonly close to 1), each fitting value is $0.1/f^{0.9}$ and $0.5/f^{0.9}$ $(\mathrm{pA^2/Hz})$ for 100 mV and 200 mV. Each current trace has the RMS noise values of 18.8, 19.1, and 19.8 $\mathrm{pA_{RMS}}$ at 0, 100 and 200 mV, respectively, and the increase in RMS noise is not that significant as the voltage increases (inset of figure 4-4d). The low 1/ f noise in the oxide material is interpreted as a homogeneous surface charge of pore wall in aqueous solution, which is consistent with the results in piranha-treated SiN pores.[17]

However, unexpectedly, the nanopore based on ZnO membrane shows the excess dielectric noise compared to the device based on $\mathrm{SiN_x}$ membrane. As shown in figure 4-5a, $\mathrm{SiN_x}$ pore (G ~7 nS) exhibits low value of dielectric noise, $7 \times 10^{-8} f$ $(\mathrm{pA^2/Hz})$, which is well-fitted into linear relationship ($S_{I,Di}(f) = C \times f$, where C is fitting parameter). In contrast, ZnO nanopore shows the excess high frequency noise near 1 kHz, which is poorly fitted with linear relation. We suspect that such high frequency noise may be resulted from dielectric properties of ZnO material, which exhibits dielectric constant

dispersion in low frequency region due to space charge polarization and exhibits peak function behavior of the dielectric loss in the dispersion frequency region.[42] In fact, it was reported that maximum dielectric loss value of ZnO plate is near 1 kHz[43], which is very close to the range where the excess dielectric noise of ZnO nanopore is generated. Despite of the unexpected high frequency noise, the difference in RMS noise between SiN_x (15 pA_{RMS}) and ZnO pores (19 pA_{RMS}) is less than 5 pA_{RMS} at 100 kHz (figure 4-5b) and these noise level provide sufficient signal to noise ratio to detect DNA translocations.

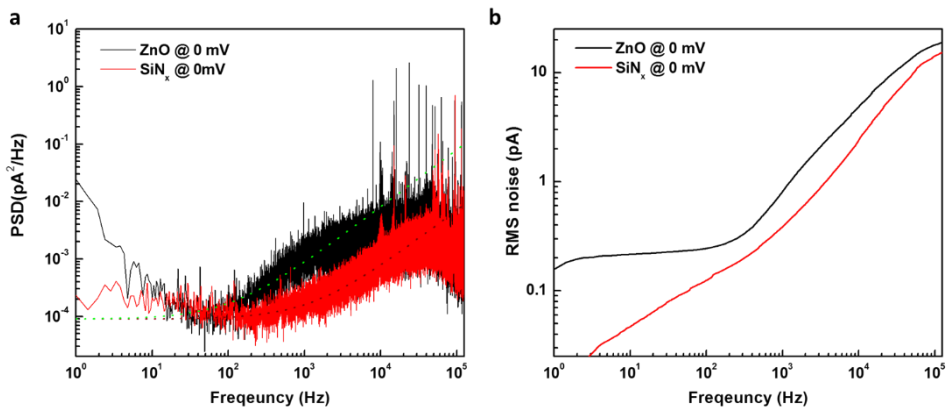

Figure 4-5. Noise characteristics of ZnO and SiNx devices. (a) Power spectral densities of ZnO and SiN_x nanopore devices with similar conductance (G ~ 7 nS) at 0 mV. The dotted lines are the fitting lines of thermal noise and dielectric noise. (b) RMS noise versus frequency plots corresponding to panel a. RMS noise is calculated by the integration of PSD (S_I) over frequency as following relation : $\mathbf{I_{RMS}} = \sqrt{\int \boldsymbol{S_I df}}$.

4.3.4. Double-stranded DNA translocation

To characterize the transport behavior of DNA molecules for ZnO nanopore, dsDNA translocations were performed using 1 kbp dsDNA through 4 nm nanopore in 1 M KCl with TE buffer (pH 8.0) at 100 kHz low-pass filter. Continuous 10-second raw current traces with corresponding voltages are shown in figure 4-6. Also, figure 4-7a shows the representative events of dsDNA translocation under 200 mV to 350 mV. From the current traces, each DNA events were collected to extract the dwell time (t_D) and the blockade current (ΔI). The scatter plots for ΔI versus t_D with 200 mV to 350 mV of the applied voltage are summarized in figure 4-7b. The number of total events according to each voltage is 335 (200 mV), 692 (250 mV), 786 (300 mV) and 767 (350 mV), respectively. The scatter plot exhibits a clear voltage dependency, as ΔI increases and t_D decreases as a function of the applied voltage. To obtain the mean values of blockade current, the histograms of ΔI corresponding to each scatter plots were plotted in figure 4-7c. Each histogram was fitted into Gaussian distribution, where the peak values were extracted and plotted with respect to the applied voltages in the inset. As expected, the mean values of current blockage increases linearly with the applied voltages and the blockade conductance ($\Delta G = \Delta I/V$) is obtained to 3.7 *nS* from linear fitting. Using the known geometry (pore size and thickness) of the used pore, the value of ΔG is estimated as

$$\Delta G = \sigma\left(\frac{4L_{eff}}{\pi d^2} + \frac{1}{d}\right)^{-1} - \sigma\left(\frac{4L_{eff}}{\pi {d_{eff}}^2} + \frac{1}{d_{eff}}\right)^{-1}$$

where σ is the conductivity of the electrolyte solution (10.5 S/m for 1 M KCl), d_{eff} is the effective diameter of the blocked pore given by $d_{eff} = \sqrt{d^2 - {d_{DNA}}^2}$ and $d_{DNA} = 2.2\ nm$ is the diameter of double stranded DNA (dsDNA).[23] Considering the used pore dimension (d = 4 nm and L_{eff} = 6 nm), the measured ΔG (3.7 *nS*) is consistent with that determined by the calculated ΔG (3.8 *nS*).

To determine the mean DNA dwell time (t_D), the histograms of logarithm of t_D at four voltages in the range 200 - 350 mV are plotted in figure 4-7d. From the Gaussian fitting, the most probable dwell times for the given voltages is shown in the inset of figure 4-7d. The fitted mean t_D are 13.8, 1.89, 0.93 and 0.53 msec at 200 – 350 mV, respectively, and these values decrease exponentially as a function of an applied voltages. Exponential dependence of dwell time on the voltage suggests the translocation process is governed by interaction with DNA molecule and pore wall.[44] Generally, the translocation time of 1 kbp DNA is in the range of about 100 μs[1], whereas the observed t_D through ZnO nanopore is more than 10 times slower (13.8 msec at 200 mV). Direct comparison of 1kbp dsDNA on SiN_x and ZnO pores is shown in figure 4-8a, where there is clear difference in dwell time of SiN_x and ZnO (85 μsec vs. 1.89 msec at 250 mV) as expected. The minimum translocation speed is ~13 μsec/bp at 200 mV, which is close to the range of ideal velocity for solid-state nanopore sequencing applications (1000-10 μsec /bp).[2]

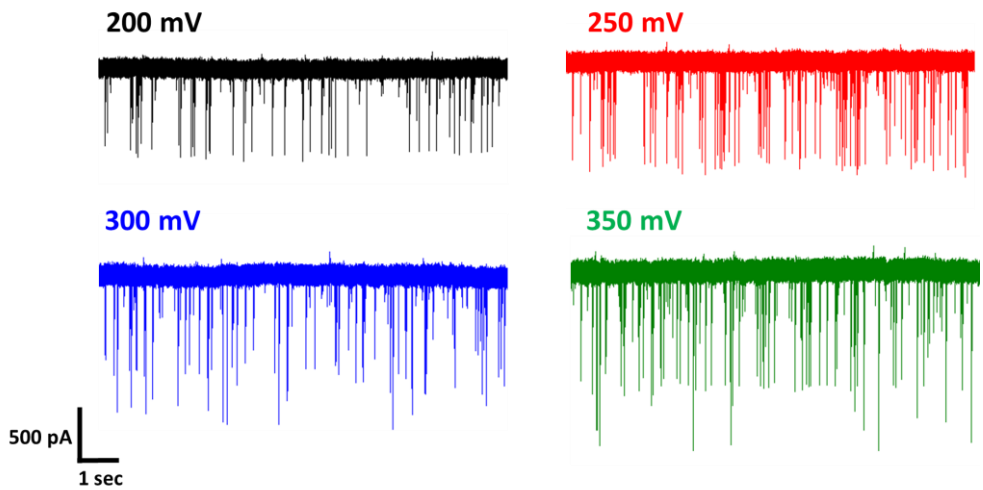

Figure 4-6. Continuous 10-sec ionic current trances for 1 kbp dsDNA translocation through Φ 4 nm ZnO nanopore in 1 M KCl with TE buffer (pH 8.0) at the voltages of 200 – 350 mV, filtered at 100 kHz.

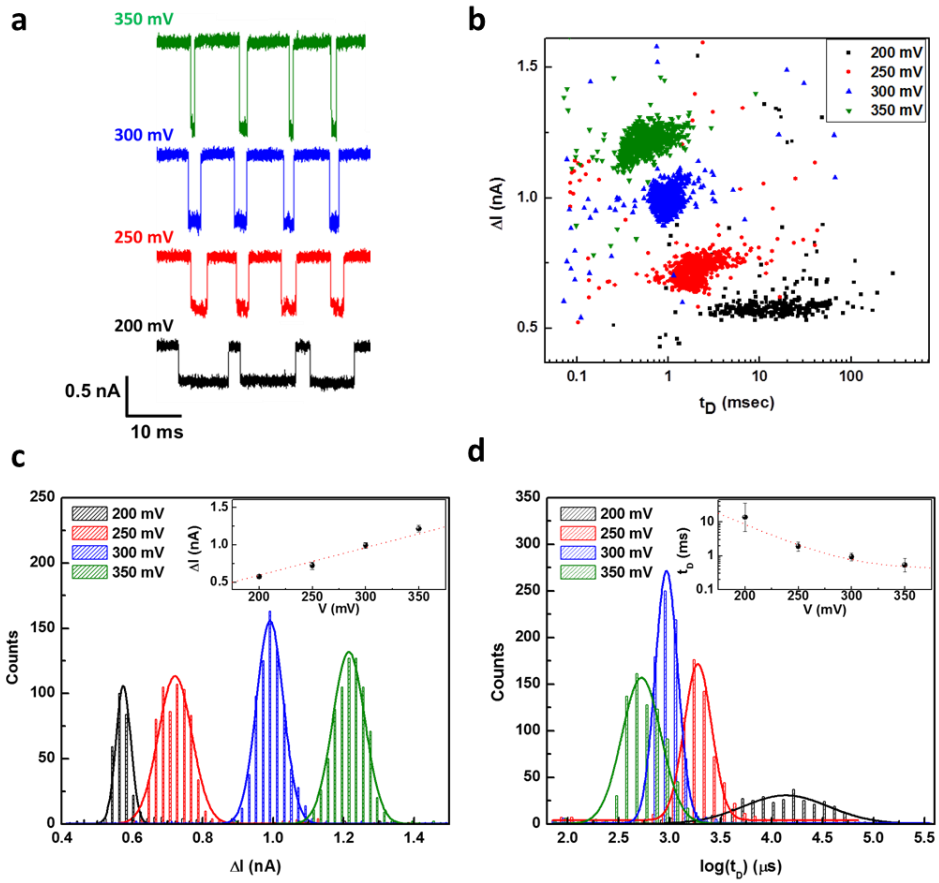

Figure 4-7. A study of dsDNA translocation through ZnO nanopore. (a) Representative translocation events of 1 kbp double-stranded DNA though ZnO pore with 4 nm diameter at various voltages in the range 200 mV to 350 mV. (b) Scatter plots of blockade current (ΔI) vs. dwell time (t_D) for 1 kbp dsDNA translocation events through 4 nm ZnO pore at the applied voltages with 200 mV to 350 mV. (c) Histograms of ΔI corresponding to panel b, in the 200 – 350 mV voltage range. Inset is the mean values of ΔI as voltages increases. (d) Histograms of logarithm of t_D in the 200 – 350 mV voltage range. Inset is the mean values of t_D as corresponding voltages. The data is fitted into exponential decay function in the dashed line.

The effective slowing of DNA translocation through ZnO nanopore can be understood as the effect of positively charged ZnO surface unlike the negative surface charge of SiN_x. In fact, bare ZnO having wurtzite type crystal structure had a point-of-zero-charge (PZC) of pH 9.1 and a zeta potential of about 20 mV at pH 8.0.[45] Such positively charged pore wall effect can be considered as (i) electroosmotic flow (EOF) by positive pore surface (ii) electrostatic interaction between negatively charged DNA backbone and positively charged pore wall. However, the slowing down of DNA translocation speed in our device cannot be explained by the EOF because positive pore wall induces the electric double layer filled with counter ion (Cl^-) and EOF composed of anion is in the same orientation of anionic DNA molecules under a driving voltage.[46] In fact, theoretical results demonstrated an increased capture rate and translocation speed by the EOF of positive gate bias.[47] On the other hand, experimental studies have shown the retarding DNA motion by the direct electrostatic interaction of positively charged surfaces such as organically functionalized nanopores[48, 49], ALD Al_2O_3 nanopores[31, 50] and positive-biased nanochannels[51, 52]. In particular, studies by Venkatesan *et al.*, on ALD Al_2O_3 nanopores which have PZC (pH 9.1 for α–Al_2O_3) for similar to ZnO observed long-time DNA translocation involving significant interactions with the nanopore.[31] Such difference between empirical and theoretical results can be explained by the fact that the hydrodynamics model used in the simulation model, where DNA strand is

considered as a rigid rod passing in the center of nanopore does not fully reflect the interaction between DNA and surface.[46] All the taken together, positively charged ZnO pores appear the dominant effect of DNA-pore surface interaction, rather than the EOF which is expected to yield high translocation speed.

To further investigate the effect of electrostatic interaction on DNA translocation, we first extract the value of velocity v and the diffusion constant D from the fit of dwell time distribution to 1D Fokker-Planck equation :

$$\mathrm{P(t)} = \frac{L}{\sqrt{4\pi D t^3}} \exp\left(-\frac{(L - vt)^2}{4Dt}\right)$$

,where L is the length of a long polymer.[53] The histograms of t_D at five different voltages were fitted with the model as shown in figure 4-9b. The corresponding values of v and D for SiN_x and ZnO pores were plotted in figure 4-8b. The average value of the diffusion constant for ZnO device under low bias values (200 mV – 300 mV) is D $\sim 3.5\ nm^2/\mu s$, which is approximately one order lower value than D of SiN_x ($\sim 57\ nm^2/\mu s$) under similar voltages. This result indicates that the additional drag force acts on DNA translocation through ZnO pore since the diffusion constant D is inversely proportional to the drag coefficient f from the Einstein-Smoluchowiki relation for charged particles, ($\mathrm{D} = k_B T/f$).[53] In order to correlate the additional friction force with the electrostatic interaction, we introduced a simple frictional force model for our system. We assumed that the electrostatic interaction of DNA and pore surface induced an additional friction force interfering with the passage of DNA

molecule. Considering one-dimensional Langevin equation and a stationary state (random force and acceleration term ~ 0), the force balance in our system is illustrated in figure 4-9a and its equation is described as

$$F_{el} - (f_{drag} + f_{in})v = 0$$

, where v is a velocity of the molecule, f_{drag} is a coefficient of hydrodynamic friction drag, f_{in} is a coefficient of additional surface friction by electrostatic interaction and F_{el} is a driving force due to electric field in the nanopore.[54] Electrophoretic force F_{el} is defined as $F_{el} = \lambda V_{bias}$, where the linear charge density λ is approximately - 0.2 e^-/bp.[54] The value of f_{drag} was calculated in the data of common SiN_x pores considering only a driving force ($F_{el} = \lambda V_{bias}$) and a drag force ($-vf_{drag}$). The resulting value of f_{drag} is $6.2\ \mathrm{nN \cdot s/m}$, which is independent in the voltages (figure 4-8c) and is well-matched with the previous reported value ($7.6\ \mathrm{nN \cdot s/m}$) for λ-DNA.[52] Thus, a rough estimation of such additional friction can be obtained from $f_{in} = \frac{\lambda V_{bias}}{v} - f_{drag}$ as a function of the applied voltages in figure 4-8c. The maximum value of friction coefficient by electrostatic interaction is $\sim 805\ \mathrm{nN \cdot s/m}$ at 200 mV, which is two orders of magnitude larger than the value of f_{drag}. In figure 4-8c, the drag friction exhibits a constant value regardless of voltage, while the interaction friction shows a tendency to decrease exponentially with increasing voltage. It means that the friction magnitude DNA-nanopore induced by electrostatic interaction decreases gradually as the electric driving force increases. This result

is in good agreement with the simulation studies by Ai et al., which predicted that while a particle-pore electrostatic interaction less affects the transport behavior as the electric field become stronger.[55] At 400 mV, the friction coefficients decreased to $42\ \mathrm{nN \cdot s/m}$, but this value is still about one order larger than the value of f_{drag}. Similarly, another three ZnO pores with different geometry show similar the mean dwell times (~400 μsec) at 400 mV, which imply that the slowing effect by additional friction force still remains in different dimension pores at relatively high voltage (figure 4-10).

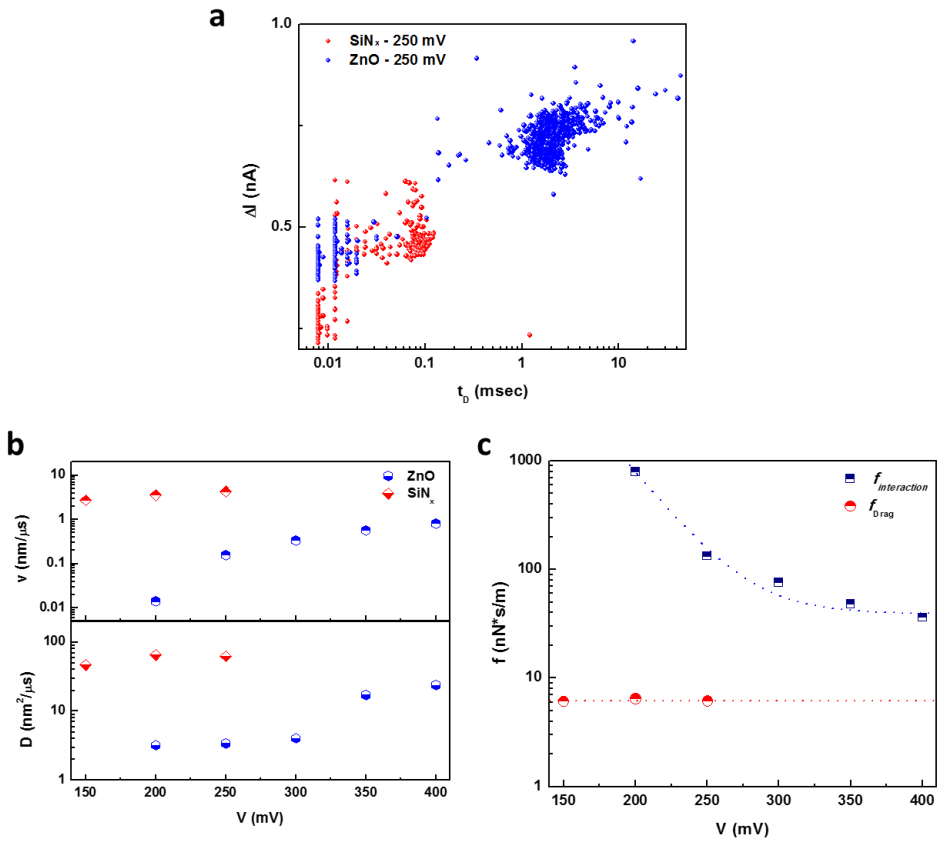

Figure 4-8. Further investigation of slowing effect of ZnO pore. (a) ΔI versus t_D scatter plots of 1 kbp dsDNA in Φ 4nm ZnO (red) and Φ 8 nm SiN_x (black) nanopores at 250 mV in 1M KCl with TE buffer (pH 8.0), low-pass filtered at 100 kHz. (b) Extracted values for drift velocity *v* and diffusion coefficient *D* of ZnO and SiNx devices as a function of the applied voltage from 1D Fokker-Planck equation. (c) Friction coefficients of hydrodynamic drag (f_{Drag}) and electrostatic interaction ($f_{interaction}$) in the range of the applied voltage.

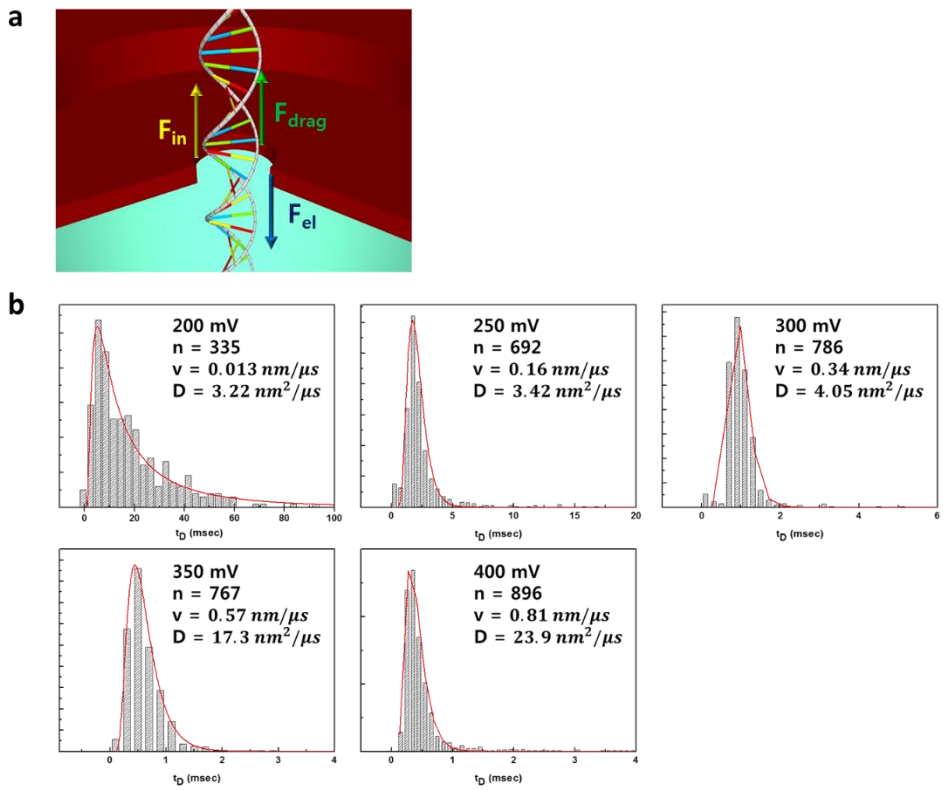

Figure 4-9. Friction force model in ZnO pore. (a) Scheme of a typical dsDNA translocation through a positively charged ZnO pore along with electrophoretic driving force (F_{el}), hydrodynamic drag force (F_{drag}) and surface frictional force (F_{in}) of electrostatic interaction. (b) Histograms of dwell time for 1kbp dsDNA translocation through 4 nm ZnO pore at 200 – 400 mV. The solid-lines are the fitting lines to 1D Fokker-Planck model for obtaining the drift velocity and diffusion coefficient.

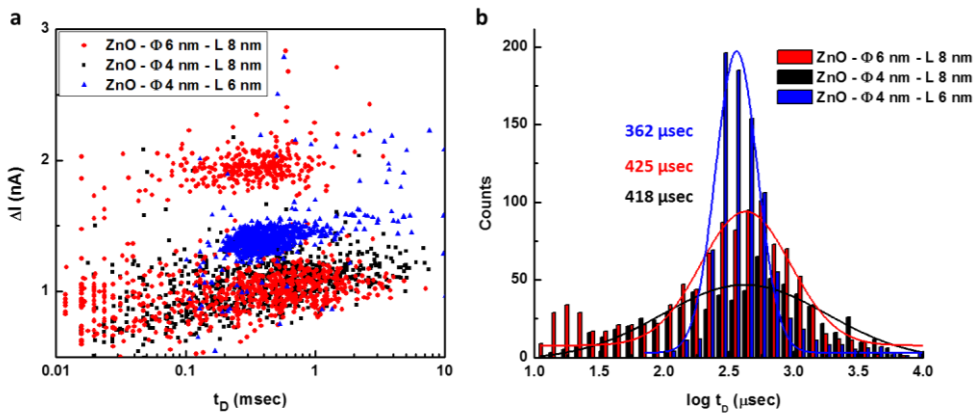

Figure 4-10. Reproducibility check of slow translocation in ZnO pores. (a) Scatter plots of ΔI and t_D through different ZnO pores at 400 mV. (b) The Histograms of logarithm of t_D corresponding to panel a.

4.4. Single-stranded DNA translocation

Finally, we demonstrated the characteristics of single-stranded DNA (ssDNA) through ZnO nanopores as a potential application for DNA sequencing. To confirm the compatibility of ZnO nanopores with ssDNA experiments, poly A_{60} ssDNA molecules were translocated through ZnO pore. For obtaining the high blockade signal in small-sized nanopore, we used 3 M KCl electrolyte solution with TE buffer (pH 8.0), which is expected that the signal amplitude is enhanced approximately three times more than that at 1M KCl solution. Figure 4-11a presents 30-second continuous ionic current trace for translocation events of poly A60 ssDNA through ZnO pore with Φ 1.2 nm diameter at 300 mV. As seen in the current trace, most translocation events are fully blocked enough to reach the base line. Scatter plots of blockade currents vs. dwell times for 250 mV and 300 m are shown in figure 4-11b. Similarly to the behavior of dsDNA, ssDNA molecules show the strong interactions with the ZnO pore wall from an enormous retardation of dwell times. As shown in the scatter plots, distribution of events is clearly divided into bouncing, which and real translocation. This trend for the discrimination of bouncing and real translocation is also shown in figure 4-11c for the histogram of logarithm of t_D. The mean dwell time value is 1 to 2 msec, which is significantly slow translocation considering the length of analyte ssDNA is 60 nt (~20 nm). Converting the dwell time to translocation speed, the velocity of poly A_{60} through Φ 1.2 nm ZnO pore is 15~30 μsec/nt, which is much slower value than ~0.3 μsec/nt in SiN_x pore.[56] This speed is slow

enough to measure a single nucleotide with a 100 kHz filter, which have 10 μsec temporal resolution.

To further investigate the controllability of ZnO pore with specific nucleotides, we evaluated and compared the transport kinetics between poly A_{60} and poly C_{60}. Adenine and cytosine are the representatives of purine (A, G) and pyrimidine (C, T) in DNA nucleotides. Each raw current trace for poly A_{60} and poly C_{60} through Φ 1.2 nm ZnO pore during 10 sec is shown in figure 4-12a. The experimental condition is the same to above experiment, where electrolyte solution is 3M KCl, the applied voltage is 300 mV and the low-pass filtering frequency is 100 kHz. The translocation events were analyzed and summarized in the scatter plots of figure 4-12b. The mean blockade signals of A and C are 1.35 nA for poly A and 1.31 nA for poly C. Although the difference in value was not significant, as expected, poly adenine showed a larger blockade signal than poly cytosine due to the difference in physical size, where purine has two carbon-nitrogen rings and pyrimidine has one carbon-nitrogen rings.[14] In terms of dwell times (figure 4-12d), interestingly, the mean dwell time of poly A_{60} (236 μsec) is two times slower than that of poly C_{60} (116 μsec). This result indicates that ZnO pore wall interacts more favorably with adenine nucleotide than cytosine. Our result is in good agreement with the adsorption probability of four nucleotides on ZnO surface, where dAMP shows more than twice as much adsorption amount as the other three single nucleotides.[57]

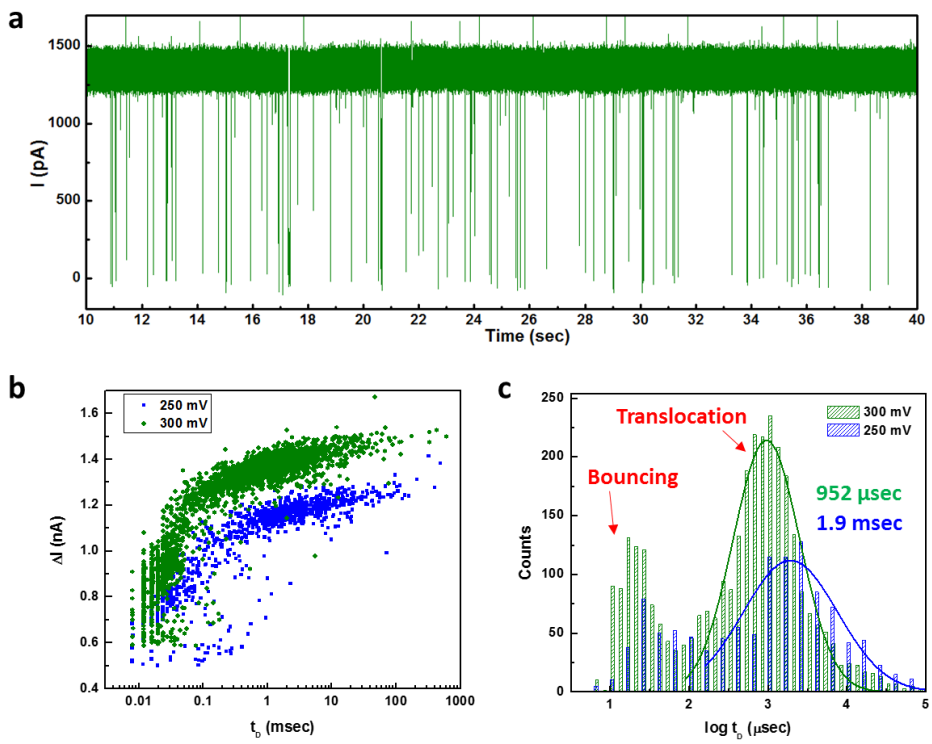

Figure 4-11. Poly A_{60} ssDNA translocation through ZnO nanopore. (a) Continuous current trace through ZnO pore with Φ 1.2 nm diameter in 3 M KCl concentration at 300 mV, filtered at 100 kHz. (b) Scatter plots of ΔI and t_D for poly A60 ssDNA at 250 mV and 300 mV. (c) Corresponding histograms of logarithm of t_D to panel b.

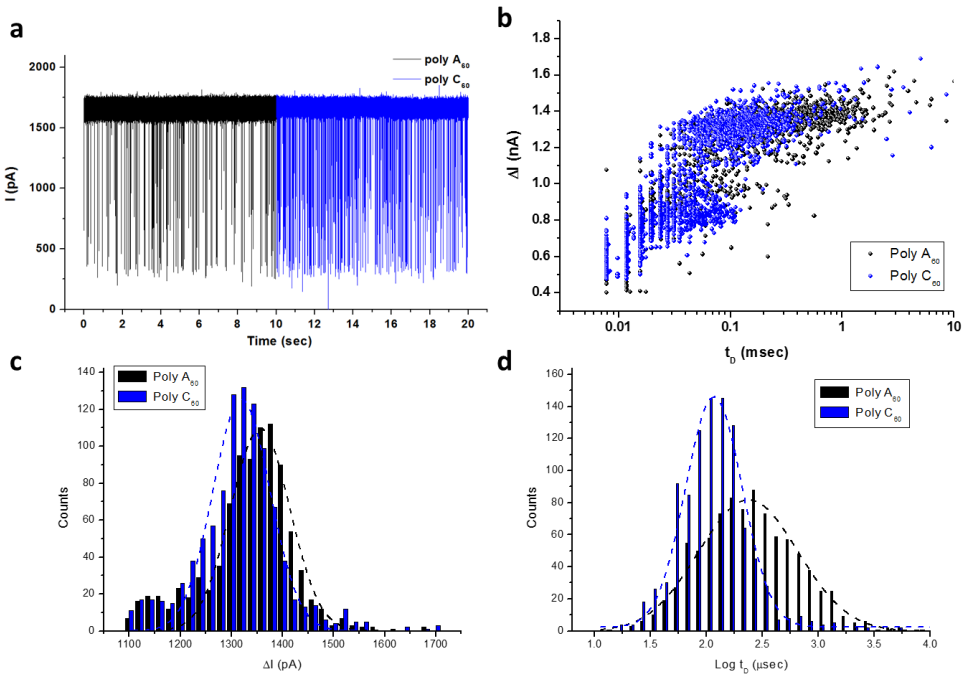

Figure 4-12. Transport behaviors of Poly A_{60} and Poly C_{60} ssDNA through ZnO nanopore. (a) 10-second continuous raw current traces for poly A_{60} and poly C_{60} ssDNA through Φ 1.8 nm in 3M KCl electrolyte solution with TE buffer (pH 8.0), filtered at 100 kHz. (b) Scatter plots of ΔI and t_D corresponding to panel a. (c) Histograms of ΔI for poly A_{60} and poly C_{60} translocations. (d) Histograms of logarithm of t_D for poly A_{60} and poly C_{60} translocations.

4.5. Summary

In conclusion, we have presented a novel fabrication process of transfer-free quartz substrate platform with low dielectric noise for single molecule analysis. Moreover, based on this platform, we have demonstrated the feasibility of ZnO materials as a new alternative to conventional SiN_x for solid-state nanopore sensors. Since ZnO nanopore has positive surface charge in pH 7~8 condition, it is expected to affect the translocation behavior of DNA molecules. To make thin membrane with sub-10 nm thickness, we used the atomic layer deposition process, and we can perforate ZnO nanopores using conventional TEM drilling method. ZnO nanopore devices exhibit superior flicker noise characteristics like the previously reported ALD oxide materials.

By dsDNA transport studies, we have revealed that ZnO nanopore can be used to detect DNA molecules efficiently and, in particular, have an effect of retarding the velocity of DNA translocation to ~13 μsec/bp, which is more than one order of magnitude reduction compared to that of SiN_x pores. Such effective reduction of DNA velocity imply that DNA-wall interaction by the positive surface charge of ZnO pore has a dominant effect on the translocation of negatively charged DNA rather than EOF. By suggesting simple friction force model, we have shown that the electrostatic interaction between negatively charged DNA and positive charged ZnO nanopore induces an additional surface friction to retard DNA motion and the friction coefficient in ZnO pore and the

friction coefficient of ZnO pore is at most two orders of magnitude higher than that of SiN_x. Further work will explore the transport behavior of ssDNA and the interaction of ZnO pore wall with specific nucleotides for DNA-based applications such as ideal DNA sequencing or single nucleotide polymorphism (SNP) detection.

Reference

1. Cees Dekker, Solid-state nanopores. *Nat Nano*, 2007. **2**(4): 209-215.
2. Bala Murali Venkatesan and Rashid Bashir, Nanopore sensors for nucleic acid analysis. *Nat Nano*, 2011. **6**(10): 615-624.
3. M. Wanunu, Nanopores: A journey towards DNA sequencing. *Phys Life Rev*, 2012. **9**(2): 125-58.
4. W. Shi, et al., Nanopore Sensing. *Anal Chem*, 2017. **89**(1): 157-188.
5. J. J. Kasianowicz, et al., Characterization of individual polynucleotide molecules using a membrane channel. *Proceedings of the National Academy of Sciences of the United States of America*, 1996. **93**(24): 13770-13773.
6. Daniel Branton, et al., The potential and challenges of nanopore sequencing. *Nature Biotechnology*, 2008. **26**(10): 1146-1153.
7. M. Taniguchi, Selective Multidetection Using Nanopores. *Anal Chem*, 2014.
8. R. F. Purnell and J. J. Schmidt, Discrimination of Single Base Substitutions in a DNA Strand Immobilized in a Biological Nanopore. *Acs Nano*, 2009. **3**(9): 2533-2538.
9. I. M. Derrington, et al., Nanopore DNA sequencing with MspA. *Proceedings of the National Academy of Sciences of the United States of America*, 2010. **107**(37): 16060-16065.
10. Gerald M. Cherf, et al., Automated forward and reverse ratcheting of DNA in a nanopore at 5-A precision. *Nat Biotech*, 2012. **30**(4): 344-348.

11. Elizabeth A. Manrao, et al., Reading DNA at single-nucleotide resolution with a mutant MspA nanopore and phi29 DNA polymerase. *Nat Biotech*, 2012. **30**(4): 349-353.

12. Andrew H. Laszlo, et al., Decoding long nanopore sequencing reads of natural DNA. *Nat Biotech*, 2014. **32**(8): 829-833.

13. T. Gilboa and A. Meller, Optical sensing and analyte manipulation in solid-state nanopores. *Analyst*, 2015. **140**(14): 4733-47.

14. Kimberly Venta, et al., Differentiation of Short, Single-Stranded DNA Homopolymers in Solid-State Nanopores. *ACS Nano*, 2013. **7**(5): 4629-4636.

15. Min-Hyun Lee, et al., A Low-Noise Solid-State Nanopore Platform Based on a Highly Insulating Substrate. *Scientific Reports*, 2014. **4**: 7448.

16. R. M. M. Smeets, et al., Noise in solid-state nanopores. *Proceedings of the National Academy of Sciences of the United States of America*, 2008. **105**(2): 417-421.

17. Vincent Tabard-Cossa, et al., Noise analysis and reduction in solid-state nanopores. *Nanotechnology*, 2007. **18**(30): 305505.

18. J. K. Rosenstein, et al., Integrated nanopore sensing platform with sub-microsecond temporal resolution. *Nat Methods*, 2012. **9**(5): 487-92.

19. Min-Cheol Lim, et al., A Mask-Free Passivation Process for Low Noise Nanopore Devices. *Journal of Nanoscience and Nanotechnology*, 2015. **15**(8): 5971-5977.

20. William H. Pitchford, et al., Synchronized Optical and Electronic Detection of Biomolecules Using a Low Noise Nanopore Platform. *ACS*

Nano, 2015. **9**(2): 1740-1748.

21. A. Balan, et al., Improving Signal-to-Noise Performance for DNA Translocation in Solid-State Nanopores at MHz Bandwidths. *Nano Lett*, 2014. **14**(12): 7215-20.
22. A. Balan, et al., Suspended Solid-state Membranes on Glass Chips with Sub 1-pF Capacitance for Biomolecule Sensing Applications. *Sci Rep*, 2015. **5**: 17775.
23. Stefan W. Kowalczyk, et al., Modeling the conductance and DNA blockade of solid-state nanopores. *Nanotechnology*, 2011. **22**(31): 315101.
24. S. Garaj, et al., Molecule-hugging graphene nanopores. *Proc Natl Acad Sci U S A*, 2013. **110**(30): 12192-6.
25. Meni Wanunu, et al., Rapid electronic detection of probe-specific microRNAs using thin nanopore sensors. *Nat Nano*, 2010. **5**(11): 807-814.
26. Julio A. Rodríguez-Manzo, et al., DNA Translocation in Nanometer Thick Silicon Nanopores. *ACS Nano*, 2015. **9**(6): 6555-6564.
27. Stephanie J. Heerema and Cees Dekker, Graphene nanodevices for DNA sequencing. *Nat Nano*, 2016. **11**(2): 127-136.
28. S. Garaj, et al., Graphene as a subnanometre trans-electrode membrane. *Nature*, 2010. **467**(7312): 190-3.
29. Kyeong-Beom Park, et al., Noise and sensitivity characteristics of solid-state nanopores with a boron nitride 2-D membrane on a pyrex substrate. *Nanoscale*, 2016. **8**(10): 5755-5763.
30. Ke Liu, et al., Atomically Thin Molybdenum Disulfide Nanopores with

High Sensitivity for DNA Translocation. *ACS Nano*, 2014. **8**(3): 2504-2511.

31. Bala Murali Venkatesan, et al., DNA Sensing Using Nanocrystalline Surface-Enhanced Al2O3Nanopore Sensors. *Advanced Functional Materials*, 2010. **20**(8): 1266-1275.
32. Bala Murali Venkatesan, et al., Stacked Graphene-Al2O3 Nanopore Sensors for Sensitive Detection of DNA and DNA–Protein Complexes. *ACS Nano*, 2011. **6**(1): 441-450.
33. J. Shim, et al., Electron beam induced local crystallization of HfO2 nanopores for biosensing applications. *Nanoscale*, 2013. **5**(22): 10887-93.
34. J. Larkin, et al., Slow DNA transport through nanopores in hafnium oxide membranes. *ACS Nano*, 2013. **7**(11): 10121-8.
35. Steven M. George, Atomic Layer Deposition: An Overview. *Chemical Reviews*, 2010. **110**(1): 111-131.
36. Tommi Tynell and Maarit Karppinen, Atomic layer deposition of ZnO: a review. *Semiconductor Science and Technology*, 2014. **29**(4): 043001.
37. Ang Wei, et al., Recent progress in the ZnO nanostructure-based sensors. *Materials Science and Engineering: B*, 2011. **176**(18): 1409-1421.
38. Hyo-Ki Hong, et al., Atomic Scale Study on Growth and Heteroepitaxy of ZnO Monolayer on Graphene. *Nano Letters*, 2017. **17**(1): 120-127.
39. Do-Joong Lee, et al., Atomic layer deposition of Ti-doped ZnO films with enhanced electron mobility. *Journal of Materials Chemistry C*, 2013. **1**(31): 4761.

40. Kim Doyoung, et al., Inductively Coupled-plasma Dry Etching of a ZnO Thin Film by Ar-diluted CF_4 Gas. *Journal of the Korean Physical Society*, 2011. **58**(52): 1536.

41. M. J Kim, et al., Rapid Fabrication of Uniformly Sized Nanopores and Nanopore Arrays for Parallel DNA Analysis. *Advanced Materials*, 2006. **18**(23): 3149-3153.

42. P. K. C. Pillai, et al., Space-charge polarisation in ZnO photoconductors. *Journal of Physics D: Applied Physics*, 1979. **12**(6): 961.

43. Reza Zamiri, et al., Influence of Mg doping on dielectric and optical properties of ZnO nano-plates prepared by wet chemical method. *Solid State Communications*, 2014. **195**: 74-79.

44. Kaifu Luo, et al., Translocation dynamics with attractive nanopore-polymer interactions. *Physical Review E*, 2008. **78**(6).

45. Mingdeng Luo, et al., Reducing ZnO nanoparticle cytotoxicity by surface modification. *Nanoscale*, 2014. **6**(11): 5791.

46. Y. H. He, et al., Controlling DNA Translocation through Gate Modulation of Nanopore Wall Surface Charges. *Acs Nano*, 2011. **5**(7): 5509-5518.

47. Y. H. He, et al., Gate Manipulation of DNA Capture into Nanopores. *Acs Nano*, 2011. **5**(10): 8391-8397.

48. Brett N. Anderson, et al., pH Tuning of DNA Translocation Time through Organically Functionalized Nanopores. *ACS Nano*, 2013. **7**(2): 1408-1414.

49. Young-Rok Kim, et al., Nanopore sensor for fast label-free detection

of short double-stranded DNAs. *Biosensors and Bioelectronics*, 2007. **22**(12): 2926-2931.

50. B. M. Venkatesan, et al., Highly Sensitive, Mechanically Stable Nanopore Sensors for DNA Analysis. *Advanced Materials*, 2009. **21**(27): 2771-+ .

51. M. Tsutsui, et al., Transverse electric field dragging of DNA in a nanochannel. *Sci Rep*, 2012. **2**: 394.

52. Y. Liu and L. Yobas, Slowing DNA Translocation in a Nanofluidic Field-Effect Transistor. *ACS Nano*, 2016. **10**(4): 3985-94.

53. Jiali Li and David S. Talaga, The distribution of DNA translocation times in solid-state nanopores. *Journal of Physics: Condensed Matter*, 2010. **22**(45): 454129.

54. Bo Lu, et al., Origins and Consequences of Velocity Fluctuations during DNA Passage through a Nanopore. *Biophysical Journal*, 2011. **101**(1): 70-79.

55. Y. Ai, et al., Field Effect Regulation of DNA Trans location through a Nanopore. *Analytical Chemistry*, 2010. **82**(19): 8217-8225.

56. Y. Goto, et al., Integrated solid-state nanopore platform for nanopore fabrication via dielectric breakdown, DNA-speed deceleration and noise reduction. *Sci Rep*, 2016. **6**: 31324.

57. Avnish Kumar Arora and Kamaluddin, Interaction of ribose nucleotides with zinc oxide and relevance in chemical evolution. *Colloids and Surfaces A: Physicochemical and Engineering Aspects*, 2007. **298**(3): 186-191.

Chapter 5.

Summary and conclusion

Since first idea of nanopore technology to detect single molecules through α-hemolysin was suggested in 1996, nanopore technology has been emerged as single molecule detectors such as DNA, RNA and protein molecules. Among them, its application toward DNA sequencing has drawn lots of attractions as next or next next generation sequencing platform. After 20 years of efforts, the proto-type of nanopore sequencer, named as 'Minion', based on biological nanopore has been released in 2014. Nanopore based system is attractive for 3rd generation DNA sequencing technology due to its label-free, amplification-free, real-time single molecule sensing, long read-length (> 1kbp) and possibility to portable system. However, solid-state nanopores still have limitations to overcome, compared to biological nanopores demonstrating the visible performance of DNA sequencing.

In this dissertation, experimental and fundamental research to utilize solid-state nanopore in DNA sequencing applications were conducted including general review on solid-state nanpore. In particular, the issues about signal to noise ratio and spatial resolution were studied in chapter2. The fundamental understanding on four noise sources, such as flicker, thermal, dielectric and amplifier noise, and various approach to reduce each noise source were discussed. Also, alternative solid-state membranes were introduced for enhancing signal to noise ratio or spatial resolution.

As a method for improving the noise level in two-dimensional nanopores, boron nitride (BN) device using a low-noise substrate platform and multi-layered

BN membranes with small opening area was developed in chapter 3. This work is performed in two approaches to reduce both the dielectric noise and flicker noise of device, which is one of the bottlenecks to making highly sensitive 2-D membrane nanopore devices. Flicker noise is minimized by employing multiple layers of BN with sub 100 nm opening size to enhance the mechanical stability of membrane. From these results, we proposed that the flicker noise has a correlation with the stiffness of membrane material, which is one property of mechanical stability. With these devise, we detected 1 kbp dsDNA translocation events through low noise *m*-BN nanopores with 100 kHz and 10 kHz filters.

In chapter 4, we have presented a novel fabrication process of transfer-free quartz substrate platform with low dielectric noise for single molecule analysis. Moreover, based on this platform, we have demonstrated the feasibility of ZnO materials as a new alternative to conventional SiN_x for solid-state nanopore sensors. Since ZnO nanopore has positive surface charge in pH 7~8 condition, it is expected to affect the translocation behavior of DNA molecules. By dsDNA and ssDNA transport studies, we have revealed that ZnO nanopore can be used to detect DNA molecules efficiently and, in particular, have an effect of retarding the velocity of DNA translocation to ~10 μsec/bp, which is a sufficient velocity to detect one nucleotide by 100 kHz bandwidth.

In summary, two novel fabrication methods were developed to overcome the limitations of noise and both spatial and temporal resolution. Despite of

various efforts in solid-state nanopore, it has not achieved visible results toward DNA sequencing application. As shown figure 2-1, the recent achievement in solid-state nanopore is the identification of four single nucleotides using RTIL and MoS_2 nanopore. However, it is still questionable how the signal could be distinguished by such a noisy device. The next step in solid-state nanopore is to distinguish continuous nucleotides in DNA. This work is only possible if all three of the above issues have been resolved. From this point of view, a ZnO material with a 2D structure is likely to be an alternative because it ensure both spatial resolution and temporal resolution. So, the integration of 2D ZnO membrane on low-noise platfrom will be studied in future work.

요약(국문초록)

DNA 염기서열 분석 기술은 각 개인의 질병 및 이와 관련된 신약개발과 같은 의료 분야에 활용이 될 수 있기 때문에 많은 관심을 끌고 있는 분야이다. 다양한 차세대 염기서열 분석 기술에 대한 연구가 활발히 이어지고 있는 가운데, 나노포어를 이용한 기술은 형광 라벨링이나 PCR 증폭이 필요없고, 실시간으로 단분자를 측정하여 1kbp 이상의 긴 리드렝스를 확보할 수 있다는 장점 때문에 3세대 염기서열 분석기술로서 각광을 받고 있다. 나노포어 기술에는 α-hemolysin이나 MspA 와 같은 단백질 포어를 사용하는 바이올로지컬 나노포어와 solid-state 멤브레인 위에 나노사이즈의 홀을 만들어주는 솔리드 스테이트 나노포어가 사용되고 있다. 이중 바이올로지컬 나노포어를 활용한 기술에는 DNA 염기서열 분석에 대한 가시적인 성과를 보여주고 있는 반면, 솔리드 스테이트 나노포어에는 아직 해결해야할 이슈들이 남아있는 상황이다.

서론 부분에서는, DNA 염기서열 분석과 관련된 나노포어 시스템에 대한 전반적인 내용을 서술하였다. 우선 제 1장에서는, 나노포어 기술의 역사와 기본적인 측정 원리를 설명하였다. 또한, 나노포어 기술 외에 차세대 염기서열 분석 기술들에 대한 간단한 설명과 함께, 염기서열 분석 시장에서의 나노포어 기반 기술의 현재 위치를 서술하였다. 제 2장에서는 DNA 염기서열 분석 관점에서 솔리드 스테이트 나노포어 기술의 현재 해결해야할 이슈들을 설명하였다. 또한, 이러한 이슈들을 해결하기 위해 어떠한 시도들이 솔리드 스테이트 나노포어에 적용되어 있는지에 대한 보고들을 정리하였다.

제 3장에서는 파이렉스 기판 위에 보론 나이트라이드 라는 멤브레인 물질을 사용하여 높은 민감도와 낮은 노이즈 특성을 가지는 나노포어 플랫폼을 확립하였다. 이 연구는 2-D 멤브레인을 사용한 나노포어에서의 주로 문제되고 있는 플리커 노이즈와 다이일렉트릭 노이즈를 두가지를 낮추고자 하는 목표로 수행되었다. 다이일렉트릭 노이즈는 선행연구를 통하여 검증된 파이렉스 기판 기반의 플랫폼을 사용하여 두 오더 이상의 노이즈 감소 효과를 확인하였다. 플리커 노이즈의 경우, 6~8 레이어의 두께를 가지는 BN 멤브레인을 100 nm 이하의 작은 오프닝 에어리어로 형성하여 주어 그 노이즈 레벨이 감소함을 확인하였다. 이러한 결과를 토대로, 그동안 제기되어 왔던 2-D 나노포어 소자의 플리커 노이즈의 원인으로 지목되어 오던 기계적 안정성이라는 측면에서 보다 직접적인 지표인 멤브레인의 용수철 상수를 도입하여, 이러한 멤브레인의 기계적 성질이 플리커 노이즈와 상관관계가 있음을 밝힐 수 있었다.

제 4장에서는, 쿼츠 기판위에 원자층 증착기술을 이용하여 ZnO 멤브레인을 형성하여 ZnO 물질의 나노포어 소자로서의 가능성을 확인하고, 실제 DNA 분자가 나노포어를 통과할 때의 통과 양상을 분석하는 연구를 진행하였다. 먼저, 쿼츠 기판 위에 2 μm의 오프닝 사이즈를 가지는 poly-Si를 프로텍션 층으로 사용하여, 전사방식이 필요 없는 쿼츠 기판 기반의 플랫폼을 확립하였다. ZnO 를 멤브레인으로 선택한 이유는 Zno는 화학적, 기계적 안정성이 뛰어나고, 기존에 사용하는 SiN_x 와 달리 isoelectric point 가 9.5 정도로 pH 8.0 에서 (+) 표면 전하를 가지는 점 때문이었다. 제작된 소자는 기판에서 오는 낮은 노이즈의 특성을 가져갈

뿐만 아니라, ZnO 멤브레인에서 오는 특징으로 SiN_x 포어보다 대략 한오더 이상으로 DNA의 통과속도가 느려지는 것이 확인되었다. 이러한 slowing down 효과를 설명하기 위해, (+) 표면 전하를 가지는 ZnO 포어 벽과 (−) 전하를 가지는 DNA 와의 정전기적 상호작용에 의한 추가적인 마찰력 모델을 도입하였다.

이 학위논문에서는, DNA 염기서열 분석의 활용을 위한 solid-state 나노포어의 세가지 주요 이슈들에 대해 논의를 하였다. 이러한 이슈들은 (i) 신호대 잡음비 (SNR)의 향상 (ii) 공간 분해능의 개선 (iii) DNA의 통과 속도를 늦추는 것을 포함한다. 2D 물질 중 하나인 BN를 멤브레인으로 사용한 나노포어 연구를 통하여, 2D 물질의 얇은 두께에서 오는 공간 분해능의 향상과 이에 따라 증가하는 flicker noise 에 대한 이해와 이를 개선시킬 수 있는 방법을 제안하였다. 다음으로, ZnO 물질을 나노포어로 적용하여 낮은 noise를 가지면서 DNA의 통과속도를 효과적으로 늦출 수 있는 ZnO 나노포어 플랫폼을 도입하였다. 이러한 결과들은 ZnO 나노포어 소자를 활용한 특정 핵산 간의 ZnO 포어와의 상호작용에 대한 연구나 단일 염기 다형성에 대한 연구 분야에 활용될 수 있을 것이다.

표제어 : 나노포어 기술, DNA 염기서열 분석, 전기적 노이즈, 보론 나이트라이드, 아연 산화막, 시간 분해능

학 번 : 2011-20639

List of publications

Paper

(1) Kyeong-Beom Park, Hyung-Jun Kim, Hyun-Mi Kim, Sang A. Han, Kang Hyuck Lee, Sang-Woo Kim, and Ki-Bum Kim, "Noise and sensitivity characteristics of solid-state nanopores with a boron nitride 2-D membrane on a pyrex substrate." *Nanoscale*, 2016. **8**(10): 5755-5763.

(2) Kyeong-Bum Park, Hyung-Jun Kim, Yun-Ho Kang, Jae-Seok Yu, Hongsik Chae, Kidan Lee, Hyun-Mi Kim, and Ki-Bum Kim, "Slow DNA Translocation through Zinc Oxide Nanopores in Transfer-free Quartz platform" (*on manuscript)*

(3) Ashvani Kumar, Kyeong-Beom Park, Hyun-Mi Kim, and Ki-Bum Kim, "Noise and its reduction in graphene based nanopore devices." *Nanotechnology*, 2013. **24**(49): 495503.

(4) Min-Hyun Lee, Ashvani Kumar, Kyeong-Beom Park, Seong-Yong Cho, Hyun-Mi Kim, Min-Cheol Lim, Young-Rok Kim, and Ki-Bum Kim, "A Low-Noise Solid-State Nanopore Platform Based on a Highly Insulating Substrate." *Scientific Reports*, 2014. **4**: 7448.

(5) Kidan Lee, Kyeong-Beom Park, Hyung-Jun Kim, Jae-Seok Yu, Hongsik Chae, Hyun-Mi Kim, and Ki-Bum Kim, "Recent Progress in Solid-State Nanopores," *(on manuscript)*

First author presentations

(1) **Kyeong-Beom Park**, Min-Hyun Lee, Hyun-Mi Kim and Ki-Bum Kim, "The demonstration of voltage measurement methodthough embedded metal electrode in solid-statenanopore" Nano Korea 2013 (2013)

(2) **Kyeong-Beam Park**, Ashvani Kumar, Hyung-Jun Kim, Hyun-Mi Kim, and Ki-Bum Kim "The Comparison of Noise Characteristics between Si and Pyrex Substrate in Solid-State Nanopore" 제21회 한국반도체학술대회 (2014)

(3) **Kyeong-Beam Park**, Ashvani Kumar, Hyung-Jun Kim, Hyun-Mi Kim, and Ki-Bum Kim, "h-Born Nitride Nanopore Treated by Flicker Noise Reduction Process for High Signal to Noise Ratio", MRS 2014 (2014)

(4) **Kyeong-Beom Park**, Hyungjun Kim, Jeong-Mo Yeo, Ashvani Kumar, Hyun-Mi Kim, Ki-Bum Kim "Noise Reduction Treated Boron Nitride Nanopore for High Signal to Noise Ratio", ENGE 2014 (2014)

(5) **Kyeong-Beom Park**, Hyung-Jun Kim, Hyun-Mi Kim, Sang-A Han, Kang Hyuck Lee, Sang-Woo Kim, Ki-Bum Kim "Noise and Sensitivity Characteristics of Solid-State Nanopores with 2-D Membranes" 230th ECS meeting (2016)

Patent

김기범, 김현미, 이민현, 박경범, 수직적 나노 채널 및 나노 포어를 가지는 이온 소자 (Ion device having vertical nano-channel and nanopore), 대한민국 10-2012-0066985.

Awards

2014 Materials Fair, Bio materials 분야, 우수 포스터 상 (2014. 09. 25)

2015 Materials Fair, Bio materials 분야, 우수 포스터 상 (2015. 10. 01)